Deposition of Gallium Phosphide on Silicon by Metalorganic Chemical Vapor Deposition

Deposition of Gallium Phosphide on Silicon by Metalorganic Chemical Vapor Deposition

By Trevor Smith,

A Thesis Submitted to the Department of Engineering Physics and the School of Graduate Studies in Partial Fulfillment of the Requirements for the Degree Master of Applied Science

McMaster University

Master of Applied Science (2022)

Hamilton, Ontario (Engineering Physics)

TITLE: Deposition of Gallium Phosphide on Silicon by Metalorganic Chemical Vapor Deposition

AUTHOR: Trevor Smith (McMaster University)

SUPERVISOR: Dr. Ryan Lewis

NUMBER OF PAGES: xxi, 155

Abstract

This thesis explores the deposition of GaP on GaP (100)-4° and (111)A, and Si (100), (100)-4° and (111) surfaces using metalorganic chemical vapour deposition (MOCVD) for epitaxial growth. The effects of Sb as a surfactant is also investigated. GaP/Si/GaP heterostructures are an ideal candidate for efficient difference frequency generation into the mid-infrared spectrum through engineered quasi-phase matched (QPM) templates. The difference in polarity at the GaP/Si interface makes defect-free GaP/Si growth challenging to accomplish, but the minimal lattice mismatch and infrared transparency makes it a promising economical approach to achieve high-speed satellite communication. Developing orientation patterned (OP) templates requires controlling whether primarily Ga-Si or P-Si bonds form at the interface, as these bonds are what dictate the domains orientation. The choice of pre-treatment conditions, growth conditions, and precursor species can affect the interface bonding and twin formation, both crucial factors in developing OP-QPM templates. This work extends previous studies by exploring new experimental conditions and the resulting film morphology. Conditions for smooth GaP surfaces using TMGa and PH_3 are found. Heteroepitaxy of GaP on (100) and (100)-4° Si both yielded nano-sized crystallites with a 550 °C pre-treatment and growth, but nanowires under 750 °C pre-treatment. Both yield larger dot-like crystallites under the 750 °C pre-treatment and growth. The GaP/Si(111) surface yields similarly-sized crystallites under the 550 °C pre-treatment and growth conditions, but with significant densities of spiraling nanowires. Under the 750 °C pre-treatment and 550 °C growth, micron-sized crystallites with few nanowires, and larger chain-like clusters form. Sb was found to play a significant role in the

low-temperature nucleation on Si (100) and suppression of nanowires on Si (111). These results contribute to the understanding of GaP epitaxial growth by MOCVD and Sb as a surfactant for GaP/Si heterostructures.

Acknowledgements

First and foremost, I thank my god for the countless blessings, adventures, and opportunities I have been so lucky to experience over these past two years.

The content of this thesis would not have been possible if it wasn't for all the amazing people that I have had the pleasure of meeting and working with over the course of my masters. Words cannot express my overwhelming gratitude to everyone; whether casual conversations after a long day or teaching me new techniques that would be crucial to my experiments, I am truly grateful for everyone who has helped me along the way.

My advisor, Dr. Ryan B. Lewis, thank you for the opportunity to do meaningful work, the mentorship both as an academic and when I felt particularly lost in general, the care and compassion you have for others, and the knowledge you've shared. The project you assigned to me pushed me out of my comfort zone, forcing me to grow both as an academic and researcher. You've been an amazing role model of an advisor and person, and taught me more than I ever could have imagined when I started this program. Additionally, I must acknowledge the help of Dr. Ray LaPierre. I thank you for stepping in as my acting-advisor for these last few months. I sincerely appreciate the significant time you've taken out of your busy schedule to assist me, and for your thorough critiquing of my work. Your advice, flexibility, and compassion during these difficult times have not gone unnoticed, and I don't know how I could have finished this without your help. To both of you fine gentlemen, I will be forever in your debt.

My parents, I am eternally grateful for the amazing life you have provided for

me and the endless love, care, and generosity. Thank you for always being there for me and being both personal and academic role models all my life. To my dog and best friend, Pi Smith, I love you dearly and deeply grieve your loss. You changed (and saved) my life, and I will never forget you or what you've done for me. To my sisters, Claudia and Simone, I find comfort knowing you guys are always there for me when I need you, and I couldn't have asked for better siblings to experience the sorrows and celebrations of life with.

To all the people who have assisted me during my time at McMaster, thank you sincerely. Dr. Manu Hedge played a key role in carrying out the MOCVD experiments described within this thesis, and for that I am sincerely grateful. Doris Stevanovic, thank you for your kindness, help with training, and maintaining a safe work environment in the Centre for Emerging Device Technologies (CEDT). The professors who taught me courses here at McMaster University, Dr. Peter Mascher, Dr. Erik Sorensen, Dr. Maureen Lagos, Dr. Andy Knights, and Dr. Ray LaPierre, thank you for the opportunity to take your courses and sharing your knowledge with me.

My lab mates, Ahmed Hassanen, Chris Natale, and Spencer McDermott, it's been a privilege to work with such smart and amazing people. I never expected to have such a good time with my lab mates – it takes some real great people to make sitting beside an MOCVD or AFM for hours a genuinely fun time. My dear friends (and weekend research colleagues) Benjamin Dyer (and Dayna Murdoch) and Spencer Ploeger, thank you for all the hangouts, adventures, experimenting, and good times we shared. Your friendship means more to me than you'll ever know, and the papers we have somehow published together will always be some of

my favourite momentos. Lastly, I want to thank all the friends who have enriched my life that I haven't mentioned above. Some of you, regrettably, are no longer part of my life. Nonetheless, I will always remember the times we shared, the inspiration and motivation you were, and the changes you made in my life (both as part of it, and forcing me to improve as a void in it). Some of you were also met during my masters, and I cannot express how much you all mean to me. This has been, without a doubt, the most challenging era of my life, and I cannot imagine how I could have got through it all without you. Truly, thank you from the bottom of my heart.

Dedication

This thesis is dedicated in the memory of Pi Smith (June 30 2017 - April 30 2022), my best friend who sadly passed away unexpectedly during the writing of this thesis.

Contents

List of Figures

List of Tables

Chapter 1

Introduction

1.1 Gallium phosphide (GaP) for optoelectronic applications

The modern digital age has led humans to fundamentally depend on information technology systems in practically all aspects of life. The most widely used semiconductor is silicon (Si) due to the low cost from its relatively high abundance in nature. Si is a great material for the fabrication of various integrated-circuits. However, Si has a significant downfall for some applications due to the material's band structure. Si is an indirect bandgap material, meaning that the lowest energy level of the conduction band does not have the same crystal momentum as the highest energy level of the valence band, as can be seen in Figure 1.1 [1]. This means that for Si to transition an electron from the valence to conduction band, a photon and a phonon must be involved, where the photon accounts for the difference in energy and the phonon accounts for the difference in crystal momentum. This is an acceptable characteristic for integrated-circuits. However, the indirect

bandgap of Si becomes problematic in optoelectronics applications due to the issue of radiative recombination. The requirement for a phonon and photon to be present for radiative recombination to occur makes using indirect semiconductors as a light-emission source impractical due to the low-efficiency from the unlikeliness of both phonon and photon coexisting simultaneously. This means that for light-emission applications, semiconductors with a direct bandgap are necessary. A quick inspection of Figure 1.2 clearly shows the band structure of gallium arsenide (GaAs - a direct bandgap III-V semiconductor) and that only an absorbed photon is necessary to excite an electron across the bandgap. Radiative recombination has a significantly higher efficiency than that of the indirect bandgap material. Thus, direct bandgap semiconductors provide a feasible platform for light-emission based on radiative recombination in semiconductors. The III-V semiconductors are ideal for optoelectronics due to high electron mobility, including materials such as GaAs, GaN, GaP, InAs, InP, and InSb, where all but GaP are direct bandgap. Although an indirect bandgap material, GaP still has applications in optical metasurfaces and solar cells [2, 3]. The band structure of GaP can be found in Figure 1.3, which although an indirect bandgap material, a direct transition does exist, albeit with a wider energy gap than that of the bandgap.

Both GaAs and GaP have wide transparencies into the infrared frequency range and significant nonlinear optical susceptibilities, meaning they are potential media for non-linear optical processes in the infrared range. GaAs has a larger transparency region in the mid-infrared than GaP. However, GaP is preferable to GaAs in terms of the two-photon absorption threshold [4, 5]. These factors make both GaAs and GaP ideal candidates for nonlinear two-wave mixing effects,

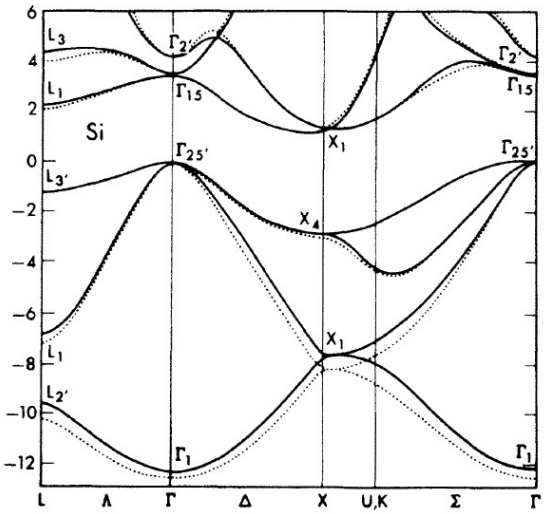

FIGURE 1.1: Band structure for Si where the solid line is calculated with a non-local pseudopotential and dashed is the local pseudopotential. Reproduced with permission from [1].

like difference frequency generation (DFG), sum frequency generation (SFG), and second-harmonic generation (SHG). Phase matching is, however, required for these effects to constructively interfere with one another in phase-space, as illustrated through Figures 1.4 and 1.5. Both figures show the addition of static phasors with constant magnitudes. That is, if $P_1 = A_1 e^{i\theta_1}$, $P_2 = A_2 e^{i\theta_2}$ are phasors, then $Real(P_1))^2 + (Imaginary(P_1))^2 = (Real(P_2))^2 + (Imaginary(P_2))^2 = A_1 = A_2$, where each consecutive phasor has an additional phase factor, θ.

Figure 1.4 shows the addition of three phasors where the magnitudes = 3 units and $\theta = 0$ radians. As can be seen, the phase matching results in an increasing real component to the signal with no imaginary component. Figure 1.5 also has phasors with magnitudes = 3 units, but the addition of a $\theta = \frac{\pi}{6}$ radian phase-shift shows the destructive nature of a phase-difference to the propagating waves intensity. After 12 additions with the $\theta = \frac{\pi}{6}$, the resulting magnitude is 0.

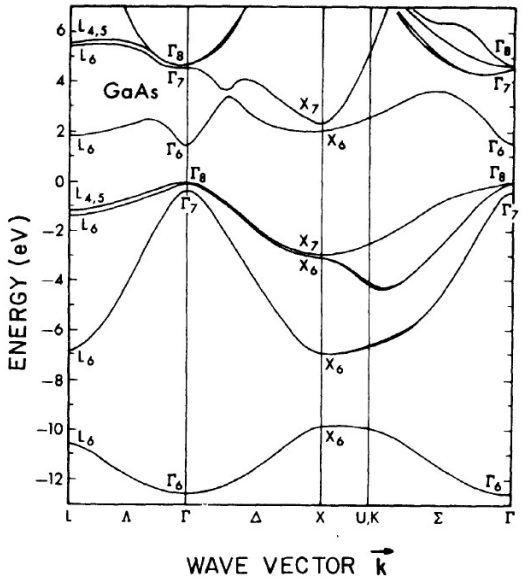

Figure 1.2: Band structure for GaAs calculated with a non-local pseudopotential. Reproduced with permission from [1].

Thus, phase matching is important to the interaction of light in an optically-active medium. Birefringent materials have a refractive index that depends on the polarization and propagation direction, meaning the angle of incidence and polarization of sources can be used to achieve phase matching. This, however, only works for materials with a strong birefringence. Materials with a weak to no birefringence, like GaAs or GaP, need some other method of counteracting chromatic dispersion. Other techniques, such as ferroelectric domain engineering, exist for ferroelectric materials such as lithium niobate ($LiNbO_3$) and lithium tantalate ($LiTaO_3$) [6, 7], but cannot be used for III-V semiconductors. One way to use III-V semiconductors for DFG and bypass this obstacle of chromatic dispersion is through a technique called quasi-phase matching (QPM). This is where phase-matching doesn't actually occur; rather, a periodic inversion in the crystal structure inverts the refractive index of the material and maintains the flow of

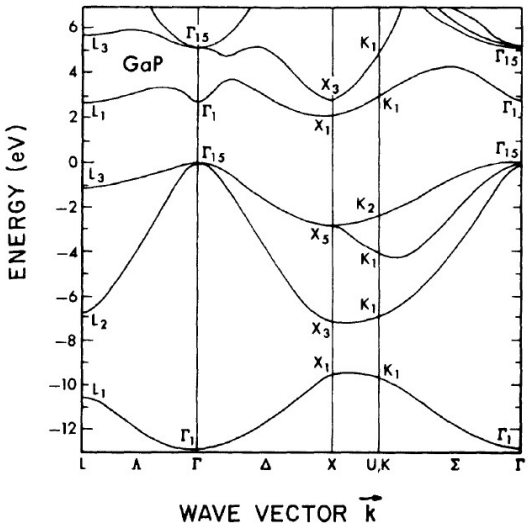

Figure 1.3: Band structure for GaP calculated with a non-local pseudopotential. Reproduced with permission from [1].

power into the desired optical mode. This is further discussed in the next section. QPM has the additional benefit of not suffering from spatial walk-off like birefringent materials.

One specific application of particular interest for QPM GaP is low-loss satellite communication in adverse weather conditions. Telecommunications typically use wavelength bands of 1300 nm and 1550 nm - both of which suffer from significant atmospheric attenuation. Figure 1.6 shows a graph of the relationship between wavelength and attenuation for atmospheric signal transmission, where visible light has a relative transmission of approximately 0.5 [8]. This makes signal transmission in the visible range to low-IR a challenging frequency range if one desires a reliable signal transmission. Various small bands of low-IR to mid-IR have higher transmission values. However, the widest atmospheric window with relatively high signal transmission is the long wavelength infrared (LWIR) window

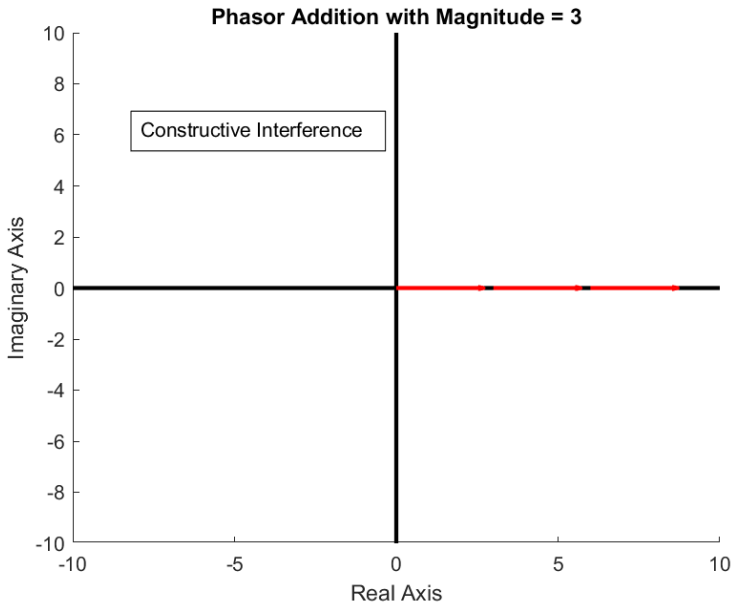

Figure 1.4: Constructive interference through addition of phase matched phasors in the complex domain.

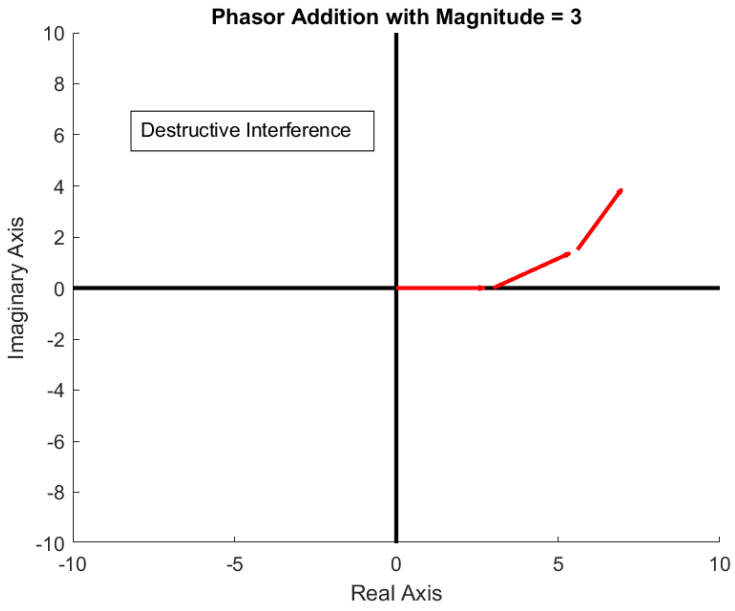

Figure 1.5: Destructive interference through addition of phasors in the complex domain that do not satisfy the phase matching condition.

of approximately 8-12 µm. This would allow for feasible communication systems that could be robust to cloud coverage and other detrimental conditions. With the use of previously discussed optical processes such as DFG, signals can be converted from an input wavelength of a standardized telecommunications band into a LWIR wavelength within the previously mentioned transmission window. This window aligns well with the merits of GaP, as the transparency range is acceptable for this range of frequencies.

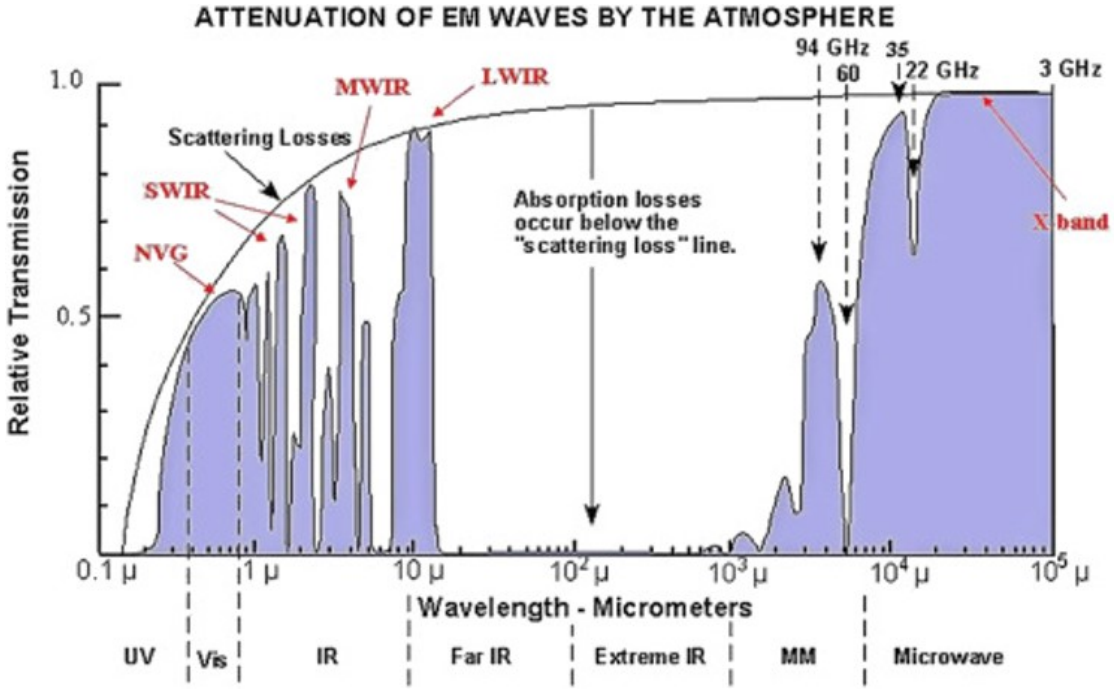

Figure 1.6: Plot of atmospheric attenuation to wavelength for relative transmission. Reproduced with permission from [8].

1.2 Substrate orientations and QPM

By definition, a crystal is a lattice structure made of periodically arranged atoms in specific configurations [9]. Different crystal structures exist for different types of materials, eg. face-centered cubic (FCC), body-centered cubic (BCC), hexagonal close packed (HCP), and some materials can be found in various structures depending on the fabrication conditions. Compound crystals like GaP or GaAs can form structures of two superimposed lattices to form a new structure, like the zinc-blende structure that results from an FCC lattice of cations and anions, or wurtzite structure that results from an HCP lattice of cations and anions. Additionally, depending on growth conditions and material-induced strain, one can form different crystal structures from the same type of material, eg., GaP can be grown in both zinc-blende or wurtzite configurations. Any disruption to the periodic structure of a lattice is called a defect. In semiconductors, defects are frequently intentionally introduced to increase or decrease the number of charge carriers in a given material, such as using dopants as electron donors or acceptors in Si. Crystal defects can be benign (meaning they do not affect growth of the crystal), but they can also cause the formation of a new crystal structure during subsequent regrowth.

For the MOCVD of GaP on GaP and Si substrates (with lattice constants of 5.45 Å and 5.43 Å, respectively), there is minimal lattice mismatch between the different materials. The monolayer height for a cubic structure can be calculated based on the specific family of planes and the atomic distance between lattice sites,

$$d_{hkl} = \frac{a}{\sqrt{h^2 + k^2 + l^2}} \tag{1.1}$$

where a is the lattice constant, h,k, and l correspond to the family of planes, and d_{hkl} is the spacing between planes. GaP has planar distances of d_{100} = 545 pm and d_{111} = 315 pm, with Si having interplanar spacing of d_{100} = 543 pm and d_{111} = 314 pm. The arrangement of the surface of the crystal will dictate how the adatoms bond and are incorporated into lattice sites. Subsequent regrowth on an epitaxially smooth surface without contaminants would ideally yield a continuation of the crystal orientation of the surface (for instance, a growth of GaP (100) should yield new layers of (100) GaP, assuming only benign contaminants on the substrate). Depending on the conditions chosen for growth, the formation of a new thermodynamically-stable crystal arrangement can form, called twins. A twin is a region of a crystal (herein referred to as a domain) where the orientation of the domain has been perturbed from that of the original orientation, often by a rotation along a crystal plane. Additionally, families of twins can be defined, where each member of the family is a rotation of some angle along a different family of crystal planes. Twins can occur in various directions; one can have twins of twins, in which one family of twins originates from the original substrate orientation, and the other originates as a family of twins from the first family of twins. The formation of twins in the grown films will be discussed further later.

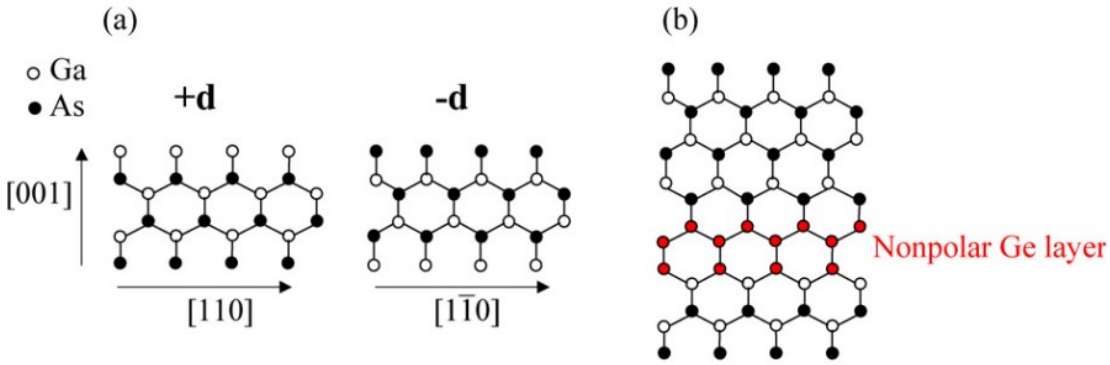

Figure 1.7: a) Diagram of a GaAs (100) lattice and the reversed lattice. b) Insertion of a non-polar layer to invert the lattice structure (one side being bonded to Ga atoms, the other side bonded to As). Reproduced with permission from [10].

Figure 1.7 shows two different periodic arrangements of GaAs (100), where the first arrangement starts with As and terminates with Ga while the reverse starts with Ga and terminates with As. A crystal reversal can be engineered by taking a terminating layer of one atom (either Ga or As), insert a thin film of a non-polar layer with minimal lattice mismatch (Ge in the case of GaAs), and force an initial layer opposite to that of the previous terminating layer (i.e. Ga-Ge followed by Ge-As or As-Ge followed by Ge-Ga). This lattice reversal scheme shown in Figure 1.7 is not exclusive to GaAs and Ge; GaP and Si have a similar lattice mismatch and has been shown to work in the same way [11].

Quasi-phase matching (QPM) is a technique for phase-matching materials with little to no birefringence, making them incompatible with techniques like critical phase-matching [12]. Birefringent materials can use the difference in beam polarization to have different refractive indices for minimizing phase mismatch. In contrast, QPM uses the periodic inversion of crystal domains to reverse the sign of the nonlinear susceptibility coefficient - allowing continuous energy flow into the

desired frequency mode.

Creating a crystal with several domains of controlled orientations and dimensions can be accomplished through the use of an orientation-patterned template. Orientation-patterned templates involve having different orientations on the surface of the substrate (eg., a surface is partially $(1\bar{1}0)$ and partially (110) in different areas) that are then regrown on top of, where the orientation of the regrown bulk crystal is the same as that of the template below. This allows for a single crystal of one material, but with various regions of controlled dimensions and orientation. By designing the template such that there is a periodic reversal of orientation at a constant length (where the domain lengths correspond to the experimental parameters of interest), various nonlinear optical processes can be efficiently executed.

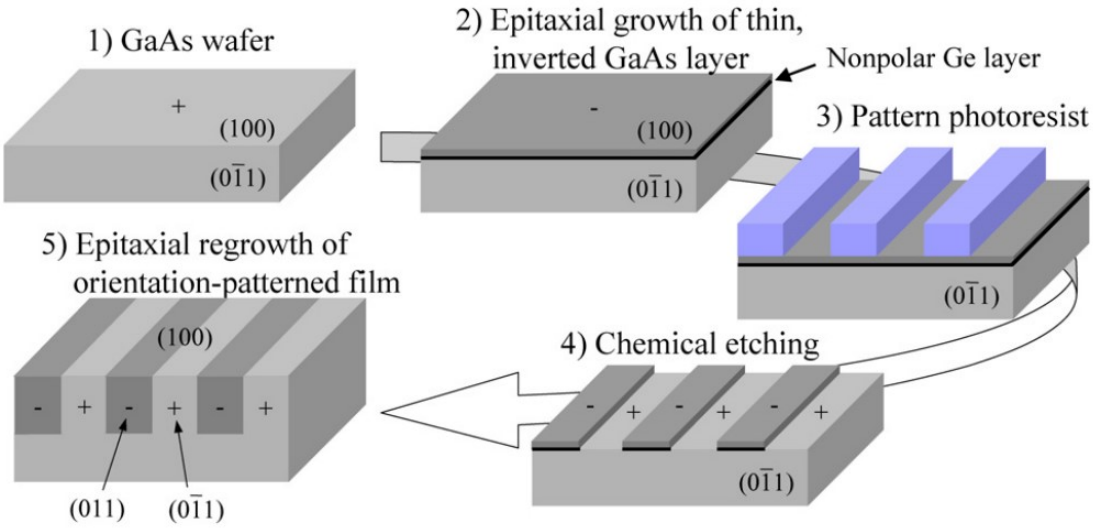

Figure 1.8: Diagram of the quasi-phase matching fabrication process for epitaxially-grown crystals. Reproduced with permission from [10].

Figure 1.8 shows a diagram of a crystal with the aforementioned domain inversions. As denoted by + and -, the periodic inversion occurs with a periodicity

chosen based on the material and different frequencies being phase matched. This repeated inversion of crystal symmetry reverses the sign of the polarization, allowing for continuous flow into the frequencies being generated by the nonlinear effect. The analysis of how to design the periodicity of the crystal to generate wavelengths of interest is a deep and involved analysis that is beyond the scope of this thesis, but is available in existing literature [13, 14]. Discussion herein focuses not to the design of these crystals, but rather fabrication using existing techniques in the semiconductor manufacturing.

Various methods can be used for the production of III-V semiconductor OP templates for subsequent crystal growth. One method for producing templates is wafer bonding. This involves the use of two crystal substrates, fusing two or more substrates together [15, 16, 5]. MBE and MOCVD growth on a OP-template is a more reliable and established technique for creating QPM materials. Several high quality QPM GaAs experiments show very promising results [17, 18], and QPM GaP has also been shown [19, 20, 21], albeit less investigated. OP-GaP has also been grown on non-GaP substrates, such as the growth of OP-GaP on an OP-GaAs [22]. Producing an OP-GaP substrate is not a trivial endeavour; comparatively less research has been conducted into GaP than GaAs. The growth of homoepitaxial GaP by MOCVD has been previously explored [23, 24], as discussed and achieved in Chapter 3. Several experiments of MOCVD grown GaP on Si have been previously performed with precursors of TEGa with TBP [25, 26, 27, 28] and TMGa and PH_3 [29] but with different conditions than the experiments described here. This thesis focuses on further exploring how TMGa and PH_3 can be used for the development of OP-GaP templates for LWIR difference frequency generation.

1.3 Thesis outline

The goal of this thesis is to explore the nucleation of GaP on Si substrates for the development of an MOCVD-grown OP-GaP template. Chapter 2 explores the underlying theory behind the experimental techniques used throughout this thesis, detailing the principles of epitaxial growth, microscopy, and x-ray diffraction. Chapter 3 explores the conditions for GaP homoepitaxy using TMGa and PH_3 precursors with atomic force microscopy (AFM) imaging to create an ideal surface for subsequent heterostructure growth. Chapter 4 examines the pre-treatment effects on an oxide-removed Si substrate using PH_3 by examining AFM imaging of the atomic surface immediately post-treatment. Chapter 5 extends this by exploring the nucleation of GaP-on-Si hetereoepitaxy using scanning electron microscopy (SEM) and x-ray diffraction (XRD). Chapter 6 extends the work of chapter 5, exploring the surfactant effect of a 5 second Sb deposition between the pre-treatment and growth steps, also aided by SEM and XRD. Lastly, chapter 7 summarizes the results and explores potential improvements and future work.

Appendices are also included for the reader's reference. Appendix A shows the 1D XRD scans generated for the various samples. This information is encapsulated within that of the pole figures, but is included for completeness. Appendix B shows the flow rates for the various experiments. Lastly, Appendix C shows the different pole figure intensity spot patterns that correspond to different families of planes that were used in the texture analysis.

Chapter 2

Background and methodologies

2.1 Metalorganic Chemical Vapor Deposition

Metalorganic vapor phase epitaxy (MOVPE), also known as metalorganic chemical vapor deposition (MOCVD), is a fundamentally important manufacturing technique in solid-state electronics. It is one of the de facto methods for the epitaxial growth of III-V material systems for a variety of devices, including but not limited to solid-state laser diodes, high-frequency devices, and photovoltaic devices [30]. Unlike molecular beam epitaxy (MBE), which requires near-vacuum conditions, MOCVD operates at a relatively higher pressure in a highly non-equilibrium chemical reactor. Whereas solid-source MBE requires effusion cells to evaporate the atomic sources, MOCVD requires gas or liquid sources made into the gaseous state using a bubbler system. MOCVD and MBE yield overall a similar growth process, but with some primary differences; MOCVD can lead to higher impurities due to the lack of an ultra-high vacuum (UHV) and carbon contamination from the organnometallic precursors, but typically have faster growth rates. MOCVD

is thus preferable to MBE for growing thick, high-quality crystals, assuming one can minimize epitaxial growth defects by optimizing the growth parameters.

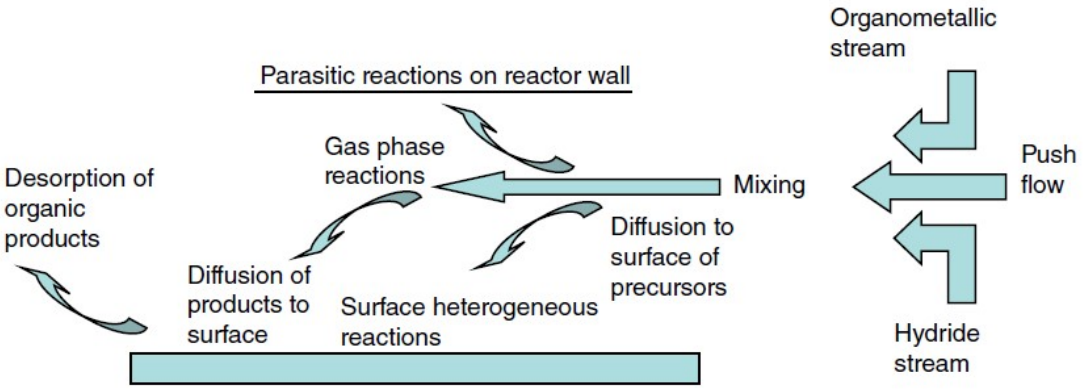

Figure 2.1: Diagram of different paths for precursors in an MOVPE growth. Reproduced with permission from [30].

One can optimize the growth process by conducting systematic trials to identify how different parameters affect a growth experiment's end product. Figure 2.1 shows the general process in which precursors are adsorbed onto a surface, referred to as adatoms [30]. Chemical species can either decompose into smaller chemical species or adhere to the surface intact. If large chemical species are not able to decompose, they can prevent further chemical species adsorption through surface passivation [31]. Samples are typically grown at various temperatures and with various precursor deposition rates to see the effects on the crystal's growth rate, surface roughness, and growth-related defects. Adjustments of these control parameters allow for a deeper understanding of the surface-level mechanisms that play a dominant role in the growth process.

Additional techniques can also alter the resulting crystals, such as using surfactants to alter the diffusion length along the crystal surface [32]. Depending on the

surfactant chosen and the structure being grown, surfactants can either increase or decrease the diffusion length by making it more or less energetically favourable for an adatom along the crystal surface to occupy a lattice site. Shorter diffusion lengths will result in increased nucleation along the surface of the crystal, which is beneficial for the growth of dense clusters of quantum dots or thin films. Longer diffusion lengths are favourable when one wants minimal nucleation sites on the surface of the crystal, such as growing nanowires (the adatom travels longer along the surface until it finds a bonding location).

Precursors are chosen based on various factors, such as thermal decomposition of species, temperature requirements, and reactor design. In this thesis, the chemical precursors of trimethylgallium (TMGa) and phosphine (PH_3) were used as the gallium and phosphorus sources. These were selected as they were already installed on McMaster's MOVPE system and allow for a fast growth rate of GaP at high temperatures with a smooth surface [23, 24]. Trimethylantimony (TMSb) was used as the antimony source, as it had been investigated previously on other semiconductors and was also available in the facilities. Various conditions were used for the growth of GaP on GaP and Si substrates; these are found at the start of the following chapters. Flow rates can be found in Appendix B.

2.2 Electron Microscopy

Electron microscopy uses electron beams to generate images of nanoscale materials. Classical optical microscopes typically have a maximum magnification on the order of 1,000, whereas electron microscopes can have a magnification of over 100,000 times. This difference in magnification results from the fundamental difference in microscope designs. Optical microscopes use a light source and one or more optical lenses. The light is reflected off the object, focused by the lenses and provides a visual amplification of the image based on the curvature and refractive index of the lens.

As the name suggests, electron microscopes rely on electrons instead of light. The electrons are emitted from an electron source, typically a heated tungsten filament or cold-field emission gun, emitting electrons with energy in the keVs. The emitted electrons then undergo focusing to a probe of nanometers in size (and new electron microscopes crossing the sub-angstrom probe threshold [33]) with the use of an electromagnetic lens that converges the electron beam through the use of a magnetic field. The probe size of the electron beam is what gives rise to the incredibly high spatial resolution of such devices. For diffraction of a wave through a medium to occur, the wavelength of the travelling wave should be on the same order of magnitude as the object it is scattering from. A sub-angstrom probe can focus the electron beam down to individual columns in a lattice, allowing for precise identification of material defects or grain boundaries that would be impractical or impossible with other techniques. Two main types of electron microscopy exist - scanning electron microscopy (SEM) and transmission electron microscopy (TEM). All electron microscopy in this thesis was conducted

with SEM; however, TEM is important in materials characterization and will be briefly discussed.

SEM uses the electron beam of the microscope and detectors to image the surface of a specimen by various means. This focused beam moves in a raster-scan motion along the surface of the crystal, making a two-dimensional image for interpretation. One SEM imaging mode involves the use of backscattered electrons (BSE-SEM) that interacted with the specimen in elastic collisions [34]. These electrons can penetrate shallowly into the surface of specimens due to their high energy, with signal intensities proportional to the Z number of the material. Another SEM mode uses secondary electrons (SE-SEM), which are electrons that result from inelastic collisions. These electrons have (relative to the original impinging electron) lower energy, so they can only emerge at or close to the surface of the substrate. Other SEM modes exist to detect other signals, such as using x-ray or photodetectors for other types of electron-matter collisions in specimens.

In contrast to SEM using signals from the surface of a material, TEM transmits a beam of electrons through a thin specimen (typically on the order of 10 to 100 nm in thickness). The beam undergoes both elastic and inelastic scattering, creating a diffraction pattern that yields information about the material characteristics. TEM also has several imaging modes, such as bright-field TEM (BF-TEM) and dark-field TEM (DF-TEM). BF-TEM uses the center region of the electron beam post-transmission - blocking out the higher angle signals where scattering occurs - making the image appear bright in areas with light atoms as the angle of scattering is dominated by the Z number. In the dark field image, the high-intensity spots

undergo scattering (the reverse of BF-TEM), allowing for a more precise determination of heavier atoms in the sample. One can also use the diffracted signal to include only specific planes of diffraction in the image by blocking all transmitted electrons except those of interest, allowing for the identification and determination of defects [35].

An additional technique, annular BF-TEM (ABF-TEM), is a variation of BF-TEM that can identify lighter atoms in the specimen, which is not typically possible in BF-TEM. BF-TEM images have a high-intensity signal from unscattered electrons that transmit through the sample, making it difficult to resolve light atoms with precision. By blocking out the unscattered portion of the BF signal using an annular (also known as a ring) detector, a higher portion of the BF signal will correspond to electrons scattered at low angles (due to the low Z number), making this an incredibly powerful technique for identifying potential contaminants and defects in epitaxial growth [36].

2.3 Atomic Force Microscopy

Atomic force microscopy (AFM) is a type of probing microscope capable of imaging the surface of materials with sub-nm resolutions. This high resolution is obtained by using a cantilever tip that scans across the surface of the material in a raster-scan pattern. A laser is focused above the cantilever, leading to measurable intensity signal changes on a quadrant photodetector when the cantilever moves up and down, as shown in Figure 2.2 [37]. These phase shifts are then converted into the height at the surface of a sample, leading to the generated image.

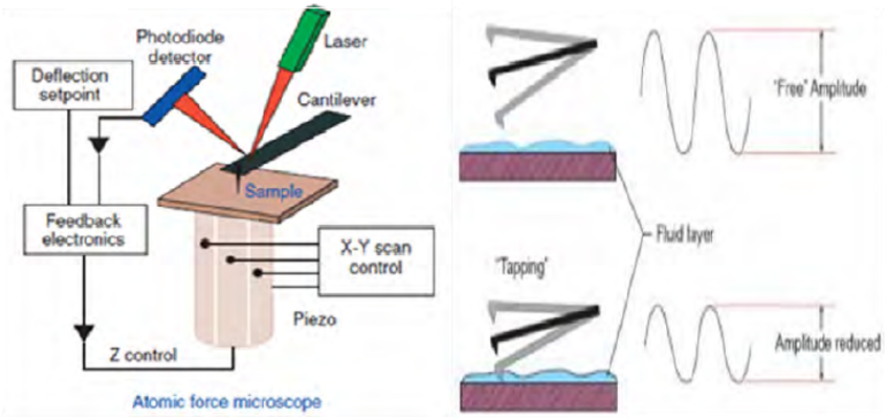

Figure 2.2: Contact mode scans involve a scan along the surface of a specimen, applying a consistent force. Tapping mode scans oscillate the cantilever near the resonant frequency, meaning the specimen doesn't undergo a shear force. Reproduced from "Atomic Force Microscopy in Detection of Viruses" [37] by Norma Hernández-Pedro, Edgar Rangel-López, Benjamín Pineda and Julio Sotelo under license CC BY 3.0.

There are two main imaging modes in AFM: contact and tapping modes. Contact mode involves dragging a cantilever tip along the material's surface, requiring a very flexible cantilever tip with a low force constant to mitigate noise and keep the surface interaction minimal. Additionally, as many samples form a thin liquid layer in standard ambient conditions, it becomes infeasible to maintain a close

interaction while preventing the cantilever tip from being stuck. As such, tapping mode is frequently used and was the method used for the studies discussed in this thesis. The tapping mode involves the cantilever tip oscillating near the resonant frequency with a constant frequency and amplitude driven by a piezoelectric element. When the cantilever interacts with the surface, the cantilever frequency dampens and reduces oscillation amplitude, allowing for the determination of sample height at that specific point. This leads to a two-dimensional height map of the sample surface. Tapping mode also involves feedback control techniques, such as proportional-integral-derivative (PID) feedback control, to minimize setpoint and tracking errors [38].

For consistency between images, it would be ideal to take all images from the same device using the same type of AFM tip. However, due to time constraints and device maintenance, images in this thesis were taken using two different AFMs. The first AFM used in experiments was an MFP-3D by Asylum Research, and the second was an Anton-Paar Tosca 400 in the McMaster Manufacturing Research Institute. Post-processing and interpretation of AFM images are performed using the open-source software Gwyddion [39]. Image-levelling uses the mean plane subtraction method [40], and row alignment (to account for mutually shifted scans along the fast scanning axis) uses a polynomial fit unless otherwise stated [41].

2.4 X-Ray Diffraction

X-ray diffraction (XRD) is the study of material properties using scattered rays to resolve information about a material like atomic arrangement, micro-structures, and defects [42]. X-rays were discovered in 1895 by Wilhelm Conrad Röntgen, and the x-ray diffraction of crystals was discovered by Max von Laue in 1912, with significant implications ever since [43, 44]. Bragg's law describes the relationship between the diffracted x-ray intensity and the wavelength of the incident x-ray,

$$n\lambda = 2dsin\theta \tag{2.1}$$

where d is the distance between atomic layers, θ is the angle of incidence, λ is the wavelength of the x-ray, and n is the "order" of reflection (where n must be an integer number to satisfy the Bragg condition).

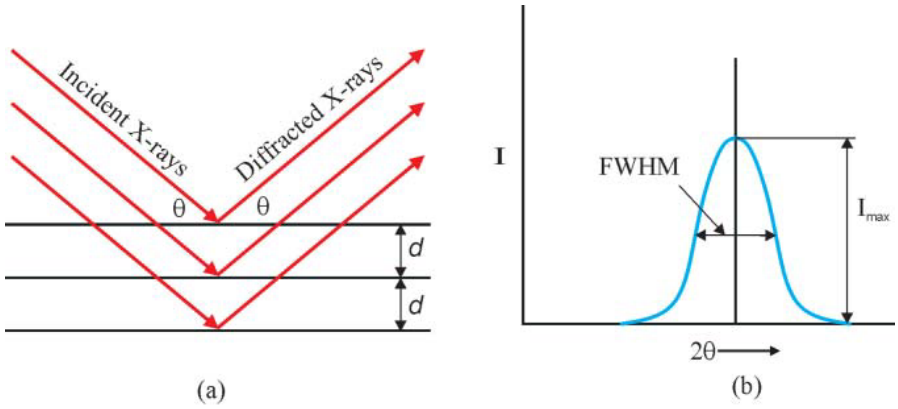

Figure 2.3: Bragg condition for a crystal structure. When the Bragg condition is satisfied, the maximal reflectance of x-rays is achieved. a) The impinging ray strikes the normal to the plane with an angle of θ, while the reflected angle is 2θ from the original direction. b) Diffraction peak observed at the corresponding 2θ angle. Reproduced with permission from [45].

Typically, $n = 1$ is used for a specific plane's intensity, and other intensity peaks at higher θ values are attributed to other planes. The θ angle is increased to find the reflectance of the crystal for different diffraction planes, allowing for a comparison between the materials' various domain orientations through texture analysis. There are many different types of XRD. One form of XRD is powder-XRD (PXRD). In PXRD, the specimen for XRD is in the powder form of the crystal being studied (for instance, GaP). The XRD pattern from the powder-coated sample will yield the XRD image corresponding to a crystal of random orientation. This can then be compared to the 1D-XRD and 2D-XRD images of a specimen with some preferred crystal orientations (not a random sample like that of the PXRD).

1D-XRD takes a sample of a specific orientation and scans the surface for a range of θ values. This differs from that of 2D-XRD, where a sample's orientation is rotated between scans to collect information about the XRD response at all angular positions along the normal axis. By sweeping the full range of angles (which is 0° to 360°), a profile of the full 2D crystal information can be found with an angular resolution of $\eta = \frac{360°}{k}$, where k is the number of measurements taken (each with a constant angular rotation). This 2D-XRD profile provides information about the crystal structure that can be interpreted by generating pole figures for a specific peak on the XRD scan.

A pole figure corresponding to a family of planes is a stereoscopic projection of the 2D scan at the various collection angles, as can be seen from Figure 2.4. Each unique plane with constructive interference has a corresponding intensity pattern in reciprocal space, with intensities proportional to the volume of the crystalline

specimen with that orientation. The image generated will have all different plane patterns superimposed on one another, with some intensity spots in the stereo projection having intensity contributions from multiple different planes. These intensities can be normalized and interpreted as a texture analysis, where the fractional intensity of each plane corresponds to the fractional volume of that texture in the sample. This will be explored further later when looking at the twinning in epitaxially grown GaP on (100), (100)-4°, and (111) substrates.

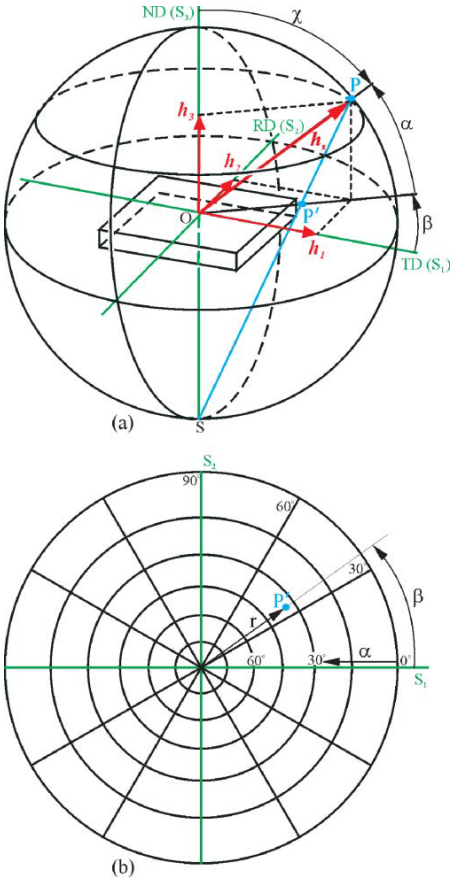

Figure 2.4: a) Definition of α and β angles based on crystal orientation. b) Stereographic projection of XRD data into the pole figure. Reproduced with permission from [46].

If there is only one crystal orientation within the scattering volume, the pole figure will show only the intensity pattern corresponding to that (hkl) plane. In the event that a crystal has more than one orientation (such as twins), the pole figure will show the intensity pattern corresponding to each (hkl) plane superimposed on one another, with the intensity proportional to the crystal volume. Figures 2.5 and 2.6 show simulated pole figures for Si and GaP (the pole figures look the same because GaP and Si have comparable lattice constants and atomic structures). The different columns correspond to the (100), (100)-4°, and (111) orientation substrates being used, with stereoscopic projections along the [0 0 1], [1 15 1], and [111] vectors in the simulations above, where the [1 15 1] vector roughly corresponds to the 4° offcut substrates. The stereographic vector for the offcut substrate is found by fitting the offcut pole figure to the (111) poles, yielding [1 15 1]. This offcut can be seen as a 'tilt' to the (100) planes pole figure, as visible by comparing the (100) on axis and misoriented pole figure simulations in Figure 2.5. Simulations are done using the WinWulff software [47], with a space group of F-43m and lattice constant of 5.45 Å.

One important factor to mention before conducting texture analysis on pole figures is the limited scanning range of the XRD system due to physical restrictions with the detector and sample holder geometry. The value of an intensity peak can be found by applying a mean average of incident x-rays over the area of the peak, yielding the full width at half maximum (FWHM) value for an individual peak. One peak can contribute to various different crystallographic orientations, meaning the fractional volume is found by finding the relative intensity of each individual plane. In the event of incomplete pole figures, families of twins are approximated based on the results shown and accounting for all known intensity points, possibly leaving out twins that are related to unscanned spots. If an intensity spot is cutoff (such that the full width of the peak is not detected due to limited theta scanning ranges), the FWHM value will be below expected and lead to texture analysis inaccuracies. The inaccurate, lower than expected intensity value will lead to lower fractional volumes of corresponding orientations to the attenuated intensity peak. In this thesis, results that suffer inaccuracies from a limited scan range are denoted with a * and only used for qualitative analysis, not quantitative.

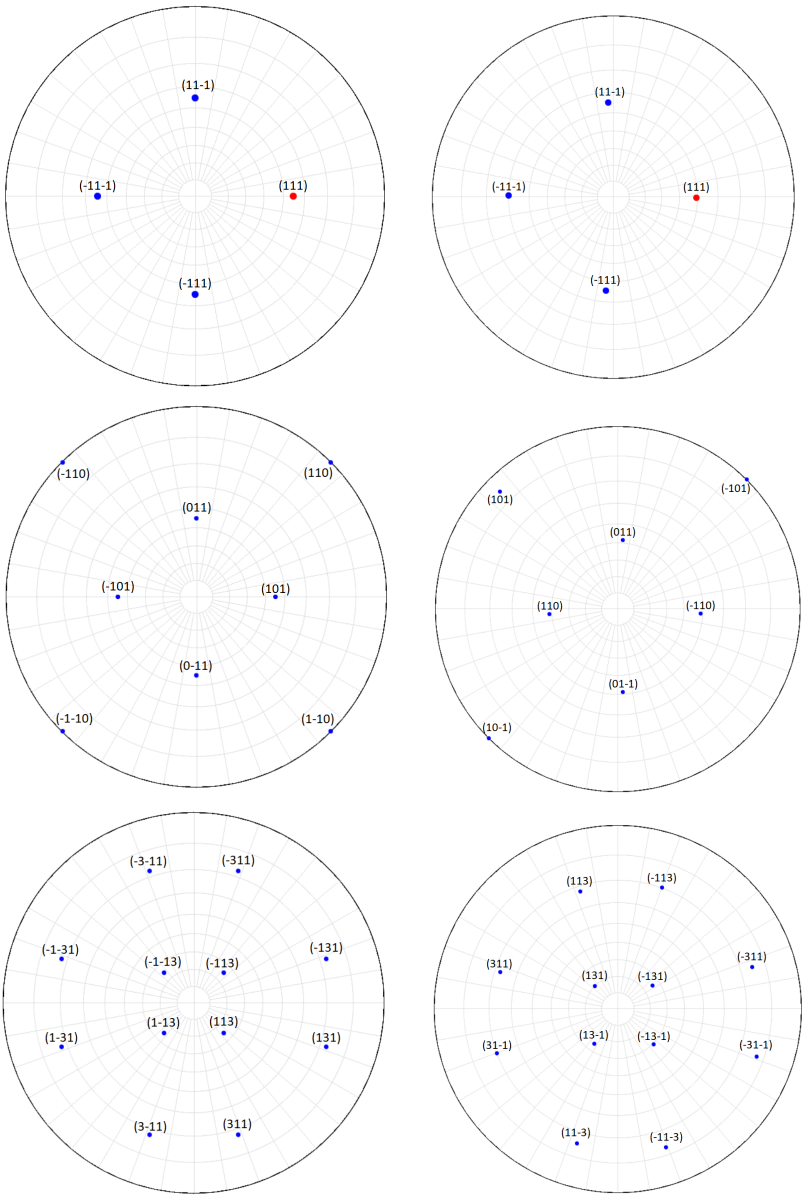

Figure 2.5: XRD simulations of GaP and Si (111), (220), and (311) pole figures corresponding to the [0 0 1] and [1 15 1] stereographic projection vectors. The [0 0 1] simulation corresponds to (100) substrates and the [1 15 1] corresponds to (100)-4° substrates. Rows going from top to bottom corresponds to (111), (220), and (311) pole figures. The left column has stereographic vectors of [0 0 1] ((100) substrates) and the right column has stereographic vectors of [1 15 1] ((100)-4° substrates).

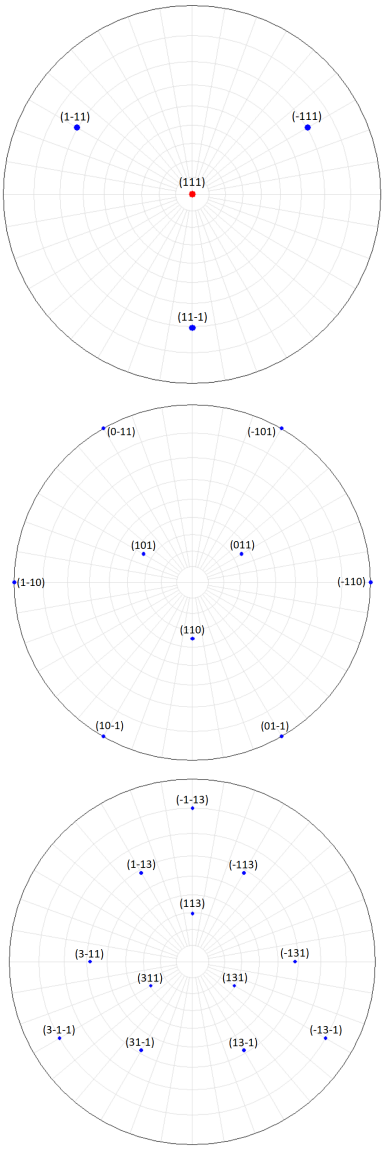

Figure 2.6: XRD simulations of GaP and Si (111), (220), and (311) pole figures corresponding to the [1 1 1] stereographic projection vector. The [1 1 1] simulation corresponds to (111) substrates. Rows going from top to bottom corresponds to (111), (220), and (311) pole figures.

Chapter 3

Homoepitaxy of GaP on (100)-4° and (111)A substrates

This chapter explores the growth of a GaP film on GaP substrates with (100)-4° and (111)A orientations. The GaP substrates in this trial were sourced from the Institute of Electronic Materials Technology in Warsaw, Poland. Specifications were measured at 300 K; the (111)A substrate was undoped, misoriented ±0.5°, had a diameter of 2" and thickness of 360±15 µm, resistivity of 0.9-2.2 Ωcm, mobility of 145-151 cm^2/Vs, and carrier concentration of 2.0-4.7 x 10^{16} cm^{-3}. The (100) offcut wafer was undoped, oriented 4° towards (111)B, had a diameter of 73 mm and thickness of 400±25 µm, resistivity of 3.96-42.5 Ωcm, mobility of 128-136 cm^2/Vs, and carrier concentration of 0.115-1.16 x 10^{16} cm^{-3}. The growth process was identical for both substrates, with the two samples placed together in the loading chamber and moved into the reactor chamber with a pressure of 75 Torr. Before commencing growth, the samples were pre-treated with a PH_3 flow for 5 minutes at 750 °C (flow rates for all experiments are in Appendix B).

This step was followed by a 5 minute GaP growth process using TMGa and PH_3 for 5 minutes at 750 °C. The precursors, TMGa and PH_3, have flow rates of 85 sccm and 250 sccm, respectively (where sccm is standard cubic centimeters per minute). Section 3.1 highlights literature on the MOCVD growth of GaP and desirable surface structures, with Sections 3.2 and 3.3 focusing on the (100)-4° and (111)A substrates, respectively.

3.1 Motivations

The growth of GaP on GaP substrates is crucial before exploring the heteroepitaxy of GaP on Si substrates. This is of fundamental importance in growing high-quality heterostructures, as potential surface-level defects could propagate in the crystal; growing an epitaxially smooth buffer layer is necessary to fabricate high-quality heterostructures. This chapter establishes the conditions required for a smooth GaP surface for subsequent heterostructure growth.

The homoepitaxy of GaP through MOCVD has previously been explored in literature, albeit less than other III-V semiconductors. Two main combinations of precursors have proven effective in MOCVD-grown GaP; triethylgallium (TEGa) with tributylphosphate (TBP) [26, 27, 28] and trimethylgallium (TMGa) with phosphine (PH_3) [24, 23]. By using TMGa and PH_3 for homoepitaxy, GaP substrates can reach smooth surfaces with a root mean square (RMS) roughness of 0.11 nm [23]. Investigation herein is limited to the use of TMGa and PH_3 due to facility availability.

3.2 GaP (100)-4° toward (111)B homoepitaxy

This section summarizes the results obtained for GaP growth on (100) GaP substrates oriented 4 degrees towards (111)B. The height trace image generated from the AFM was post-processed using a mean plane subtraction to level the data, followed by row alignment using a third-degree polynomial. AFM images of the substrates are taken prior to GaP film growth for comparison with the starting surface. Figures 3.1 and 3.2 have dimensions of 500 nm by 500 nm and 5 µm by 5 µm, respectively. The 500 nm image has a RMS roughness of 0.41 nm, and 5 µm image has a RMS roughness of 0.63 nm.

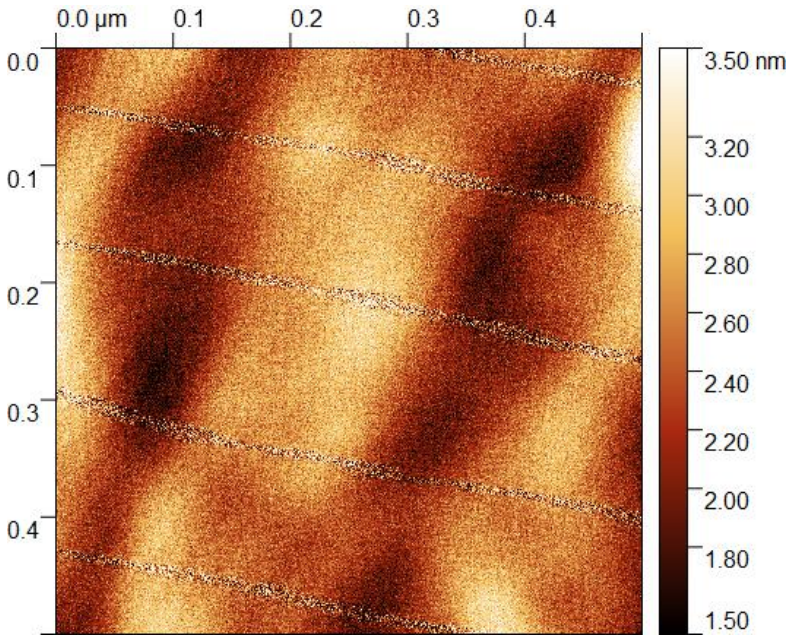

Figure 3.1: AFM image of GaP (100)-4° substrate. Dimensions are 500 nm by 500 nm.

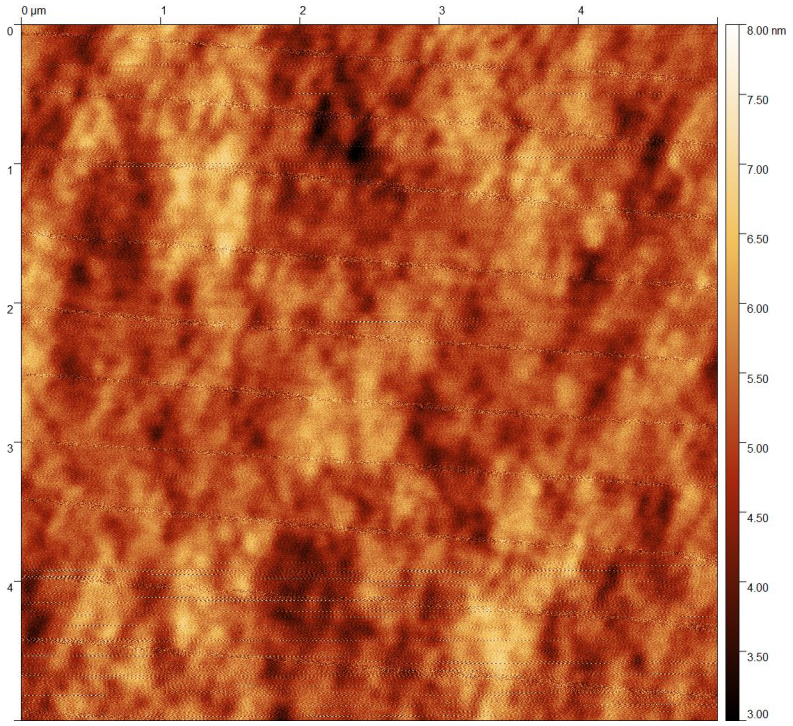

Figure 3.2: AFM image of GaP (100)-4° substrate. Dimensions are 5 µm by 5 µm.

The surface of the grown GaP on GaP film can be seen in Figures 3.3 and 3.4 with dimensions of 500 nm by 500 nm and 5 µm by 5 µm, respectively. The bottom of Figure 3.3 shows a small scan error near the bottom of the scan, so the RMS roughness is calculated with a width of 500 nm and height of 425 nm (starting from the top of the image). The area of interest has a RMS roughness of 0.29 nm. Figure 3.4 did not have any apparent image issues, so the full 5 µm by 5 µm area was used to calculate the RMS roughness, which is 0.46 nm.

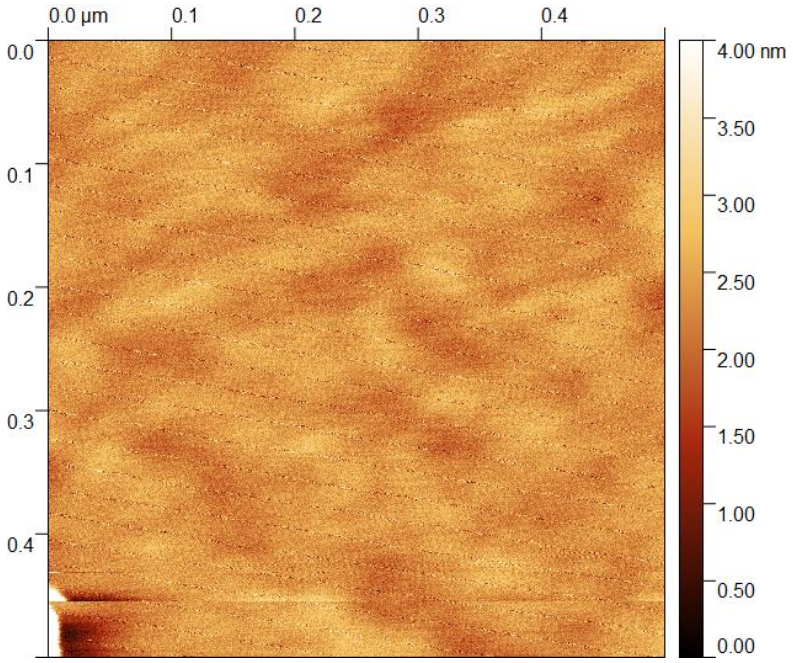

Figure 3.3: AFM image of homoepitaxy GaP (100)-4°(111)B. Dimensions are 500 nm by 500 nm.

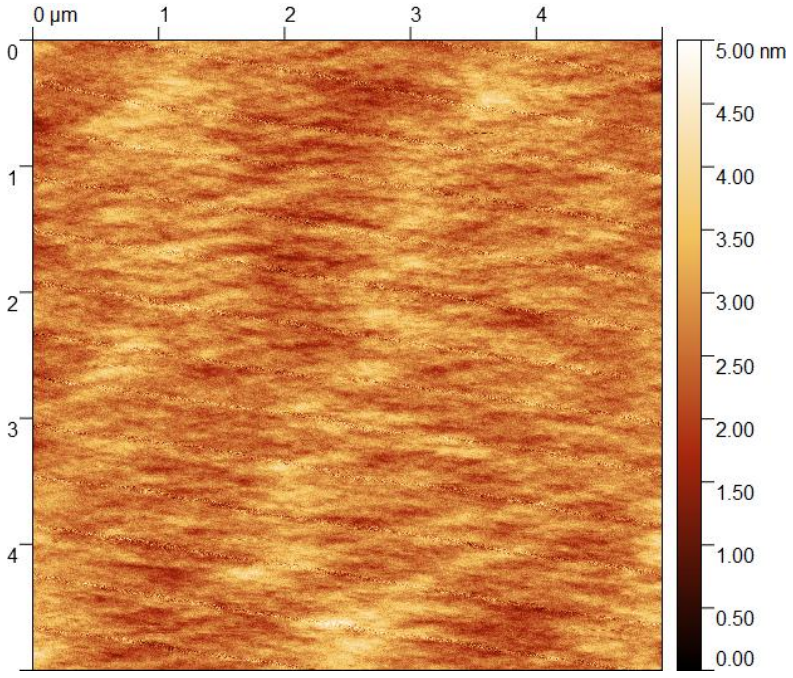

Figure 3.4: AFM image of homoepitaxy GaP (100)-4°(111)B. Dimensions are 5 µm by 5 µm.

Table 3.1 summarizes the results of the AFM RMS roughness values. It is found that the short GaP film deposition creates a smoother surface in both the 500 nm and 5 µm dimension images. Additionally, the surface of the substrates are visibly different, with the growth having a more periodic and structured pattern to the variations in height. These roughness values are consistent with other reports of GaP on offcut (100) substrates and show comparable roughness to literature [23], albeit a lower RMS roughness can likely be achieved by increasing the V/III flow rate ratio and further optimization of conditions [28].

	500 nm by 500 nm	**5 um by 5 um**
Substrate	0.41 nm	0.63 nm
Growth	0.29 nm	0.46 nm

Table 3.1: Table comparing RMS roughness of the substrate and grown film; GaP (100)-4° substrates.

The crystal structure was verified using the two-dimensional XRD pole figures generated for the (111), (220), and (311) family of planes in Figures 3.5, 3.6, and 3.7, respectively (corresponding 1D XRD scans can be found in Appendix A). The figures below show a powerful signal intensity in all pole figures at the spots which correspond to a GaP (100) crystal, albeit with a tilt visible in the pole figures. This tilt corresponds to the offcut of the sample, meaning that the intensity pattern has a 4° rotation toward (111)B in the stereoscopic projection. It is worth noting that Figure 3.5 has minimal information due to the limited scanning range chosen to expedite data collection. Although potentially problematic for complex structures with significant twinning, this sample does not indicate twinning, and thus a qualitative analysis is sufficient. It is clear from both the AFM scans showing a low surface roughness comparable to that in literature and two-dimensional XRD scans showing the pole figures of the (111), (220) and (311) families of planes, that

a smooth GaP sample in the (100) offcut orientation was successfully grown. This is a fundamental step for later trials involving the growth of Si on GaP substrates, as this allows for a high-quality surface for subsequent heterostructures.

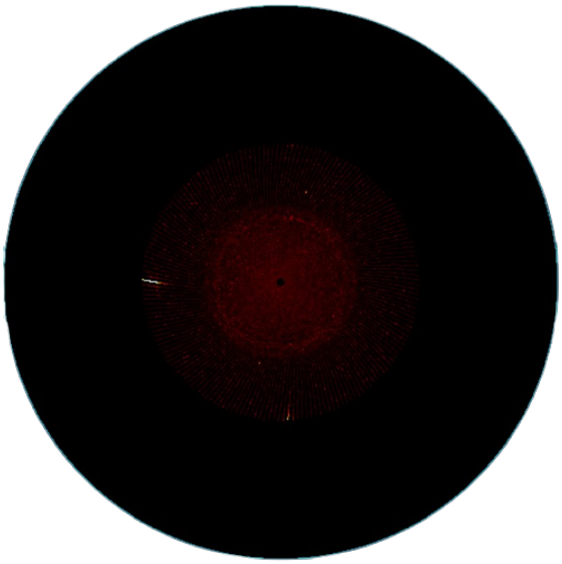

Figure 3.5: (111) pole figure for homoepitaxial GaP (100)-4°.

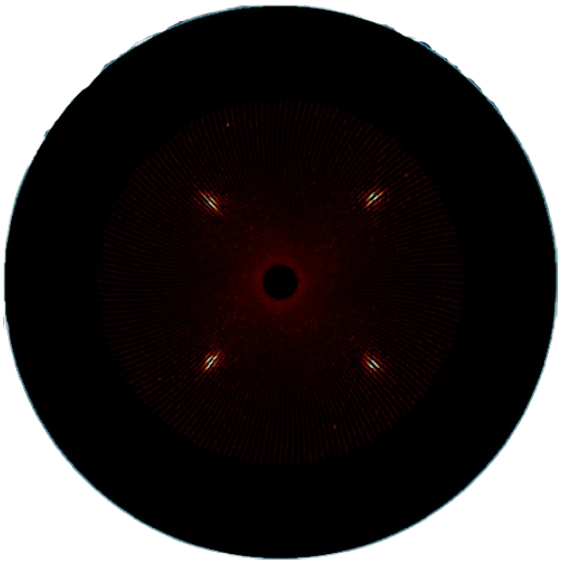

Figure 3.6: (220) pole figure for homoepitaxial GaP (100)-4°.

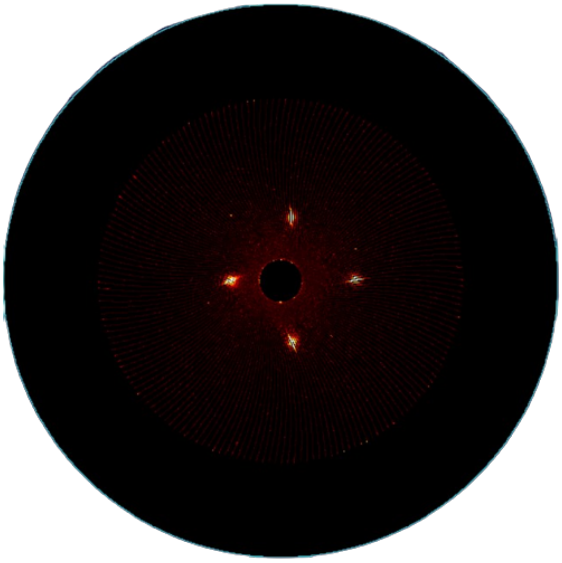

Figure 3.7: (311) pole figure for homoepitaxial GaP (100)-4°.

These samples should be of only one crystal domain. They are a benchmark for approximating how much of the random component is truly random crystal orientations and how much is from air-scattering of the x-rays. The results of the texture analysis can be found below in Table 3.2, where approximately 0.05% of the random component of the (100)-4° GaP can be attributed to air-scattering.

Pole Figure	**Main Orientation**	**Random Orientation**
(111)	99.96	0.04
(220)	99.94	0.06
(311)	99.95	0.05

Table 3.2: Texture analysis of the GaP film on GaP (100)-4° substrate from the pole figures.

3.3 GaP (111)A homoepitaxy

In this section, GaP was grown on GaP (111)A substrates. The same steps as the previous section were followed in post-processing height trace images: mean plane subtraction for data levelling and third-order polynomial row alignment. AFM images of the substrates are taken prior to GaP film growth for comparison with the starting surface. Figure 3.8 has dimensions of 500 nm by 500 nm, but due to the artifact at the bottom resulting from the polynomial row alignment, the bottom 10% of the image was excluded from the roughness calculations; this results in a RMS roughness of 0.25 nm.

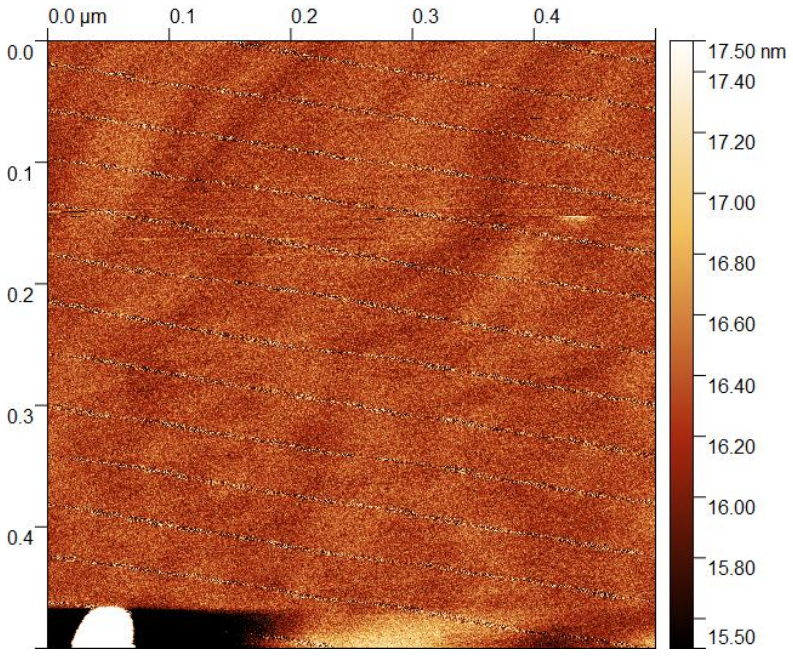

Figure 3.8: AFM image of ungrown GaP (111)A. Dimensions are 500 nm by 500 nm.

The surface of the grown GaP on GaP film can be seen in Figures 3.9 and 3.10 with dimensions of 1 µm by 1 µm and 5 µm by 5 µm, respectively. The bottom left 500 nm by 500 nm area of Figure 3.9 has a RMS roughness of 0.30 nm, and Figure 3.10 has a RMS roughness of 0.56 nm.

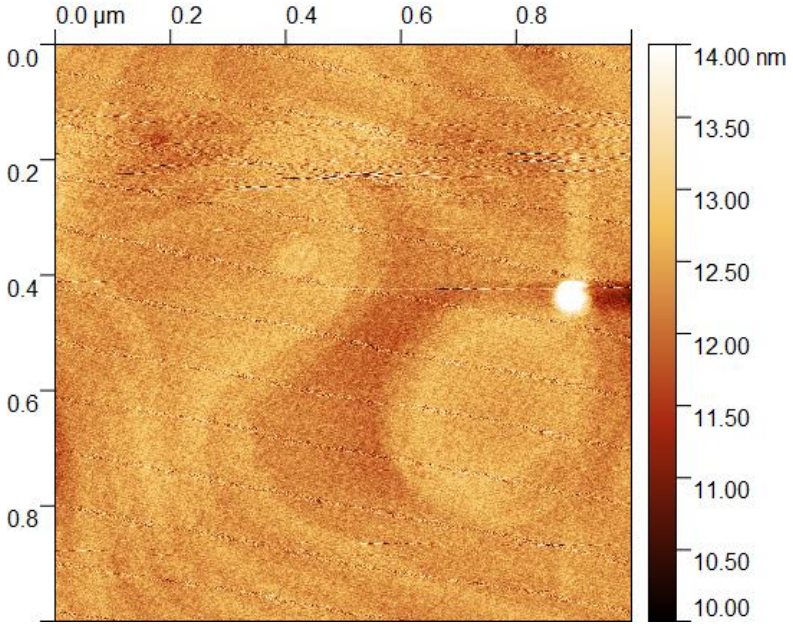

Figure 3.9: AFM image of homoepitaxy GaP (111)A. Dimensions are 1 µm by 1 µm.

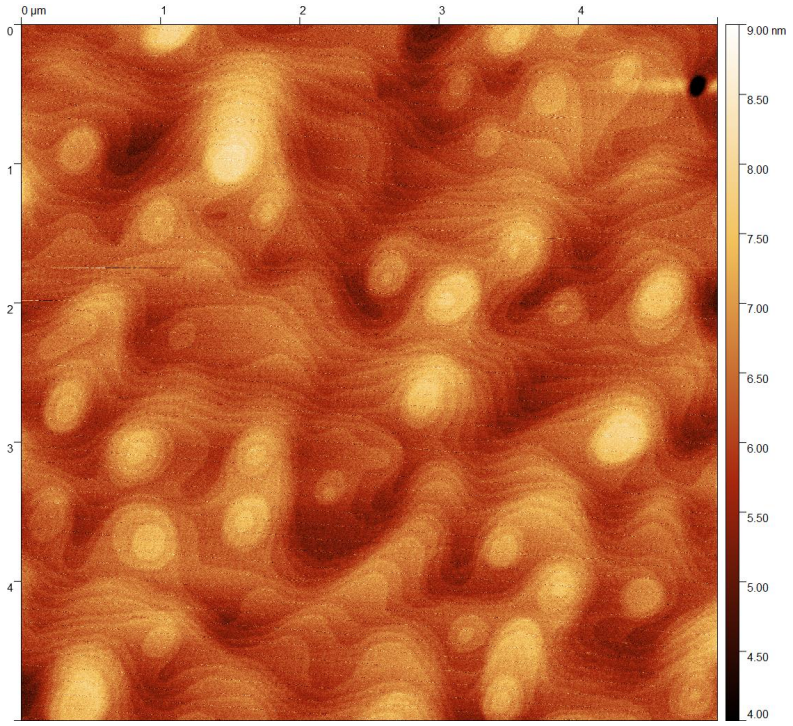

Figure 3.10: AFM image of homoepitaxy GaP (111)A. Dimensions are 5 µm by 5 µm.

Table 3.3 summarizes the results of the AFM RMS roughness values. RMS roughness for a 5 µm by 5 µm area was not performed. The roughness results show a small increase in roughness after film growth. However, step edge formations are now visible on the grown GaP film. The atomic steps visible in the image are approximately 0.6 nm in height, similar to that of a double-step of $2^{*}d_{111} = 0.630$ nm, suggesting that the surface has double-step formations during growth. The two different steps are visible from the extracted 1D height profile in Figure 3.11.

	500 nm by 500 nm	**5 um by 5 um**
Substrate	0.25 nm	-
Growth	0.30 nm	0.56 nm

Table 3.3: Table comparing RMS roughness of the substrate and grown film; GaP (111)A substrates.

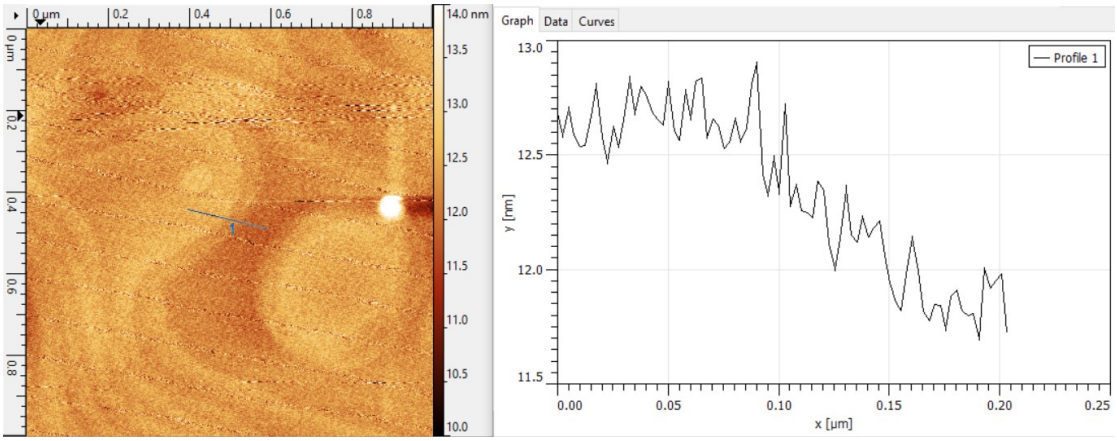

Figure 3.11: Screen capture from Gwyddion highlighting the 1D AFM GaP (111)A step formation on the grown GaP film. The height changes correspond to the GaP lattice constant, suggesting double-step formations.

The same set of pole figures were generated as the previous section, where the (111), (220), and (311) pole figures are shown in Figures 3.12, 3.13, and 3.14, respectively. Like the (100)-4° sample, there are no unexpected intensity peaks in any pole figures. One can conclude that there are no twins present in the grown structure. As growth only takes place for a short time, any grown structure would be small in volume relative to the x-ray penetration depth. Thus, if twins are forming, they will have low signal intensity relative to the main substrate orientation. As shown further in this thesis, however, growing GaP on a Si substrate (which has essentially the same pole figures as GaP due to the nearly-identical lattice constant and similarities between the diamond and zinc-blende structures) causes noticeable diffraction peaks in the two-dimensional XRD scans. This implies that if twins form on the GaP substrate, they would indeed appear in these scans; thus, the GaP would be of a single domain.

The texture analysis is performed on the pole figures on the grown film to determine how much of the random orientation one can attribute to air-scattering. The results of the texture analysis can be found below in Table 3.4, with approximately 0.05% attributed to air-scattering.

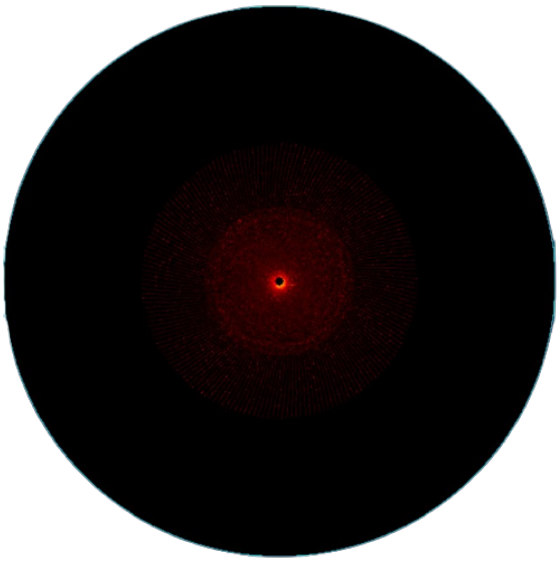

Figure 3.12: (111) pole figure for homoepitaxial GaP (111)A.

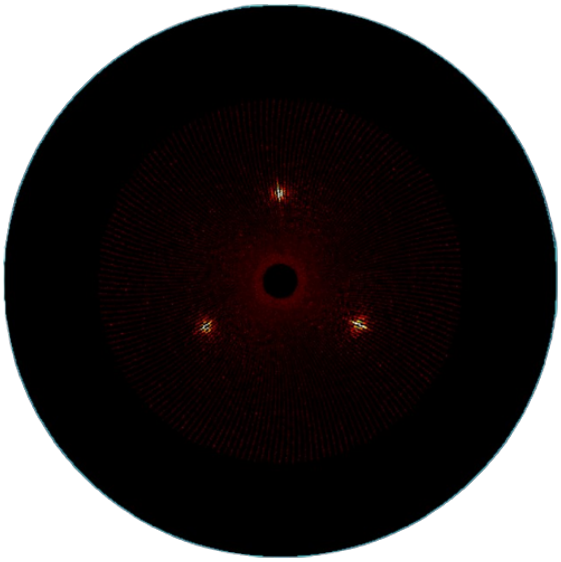

Figure 3.13: (220) pole figure for homoepitaxial GaP (111)A.

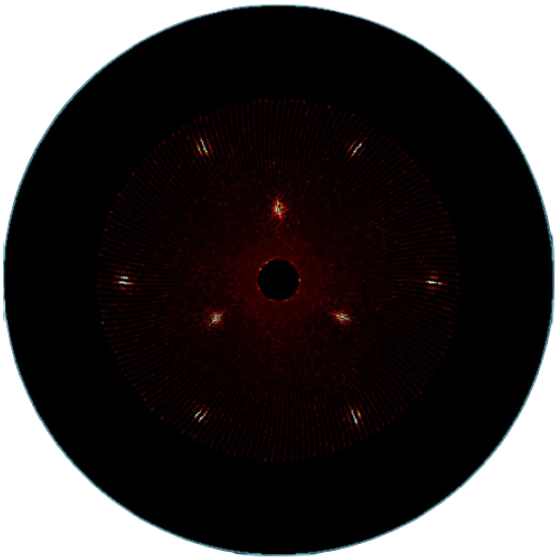

Figure 3.14: (311) pole figure for homoepitaxial GaP (111)A.

Pole Figure	**Main Orientation**	**Random Orientation**
(111)	91.41*	8.59*
(220)	99.96	0.04
(311)	99.94	0.06

Table 3.4: Texture analysis of the GaP film on GaP (111)A substrate from the pole figures. Values with a * indicate inaccurate results due to an intensity peak being cutoff.

Chapter 4

Pre-treatment of Si substrates

This chapter explores Si surfaces prior to deposition of GaP on the surface. The Si (100) substrates were sourced from UniversityWafer in Boston, USA, and the Si (100)-4° and (111) substrates in this trial were sourced from Virginia Semiconductor in Fredericksburg, USA. The (100) substrates were phosphorus-doped (n-type), had no known offcut, had a diameter of 3", thickness of 300 µm, and resistivity of over 100 Ωcm. The (100)-4° substrates were phosphorus-doped (n-type), misoriented 4° towards (110)±0.1°, had a diameter of 76.2±0.3 mm, thickness of 381±25 µm, resistivity of 0.1-0.3 Ωcm, and RMS roughness of ≤5 Å. The (111) substrates were boron doped (p-type), misoriented ±0.9°, had a diameter of 76.2±0.3 mm, thickness of 254±25 um, resistivity of 0.002-0.004 Ωcm, and RMS roughness of ≤5 Å. Samples were etched under a 1:10 hydrofluoric (HF) dip for 30 seconds followed by immediate pre-treatment under PH_3 at a temperature of 550 °C or 750 °C (for trial 1 or trials 2 and 3, respectively) for 5 minutes. The precursor PH_3 had a flow rate of 100 sccm for both temperature treatments. The following sections investigage the difference between pre-treatment temperature and substrate

orientation.

4.1 Si (100) substrate

The Si (100) substrate had a significantly different appearance depending on the temperature of PH_3 pre-treatment. Figure 4.1 shows the AFM images of the (100) substrate, where the top image (corresponding to T_{prep} = 550 °C) had a RMS roughness of 0.47 nm, and the bottom (corresponding to T_{prep} = 750 °C) sample had a RMS roughness of 0.06 nm. Si has a lattice constant of 543 pm, and the most favourable Si surface for GaP nucleation is a double-step formation [48]. A double-step of Si (100) has a 1.09 nm height difference. Figure 4.2 shows a 1D height profile along the T_{prep} = 550 °C specimen, with several sharp height shifts of approximately 1 nm. The T_{prep} = 750 °C specimen had a total height range of only approximately 500 pm, approximately equal to the height of a monolayer.

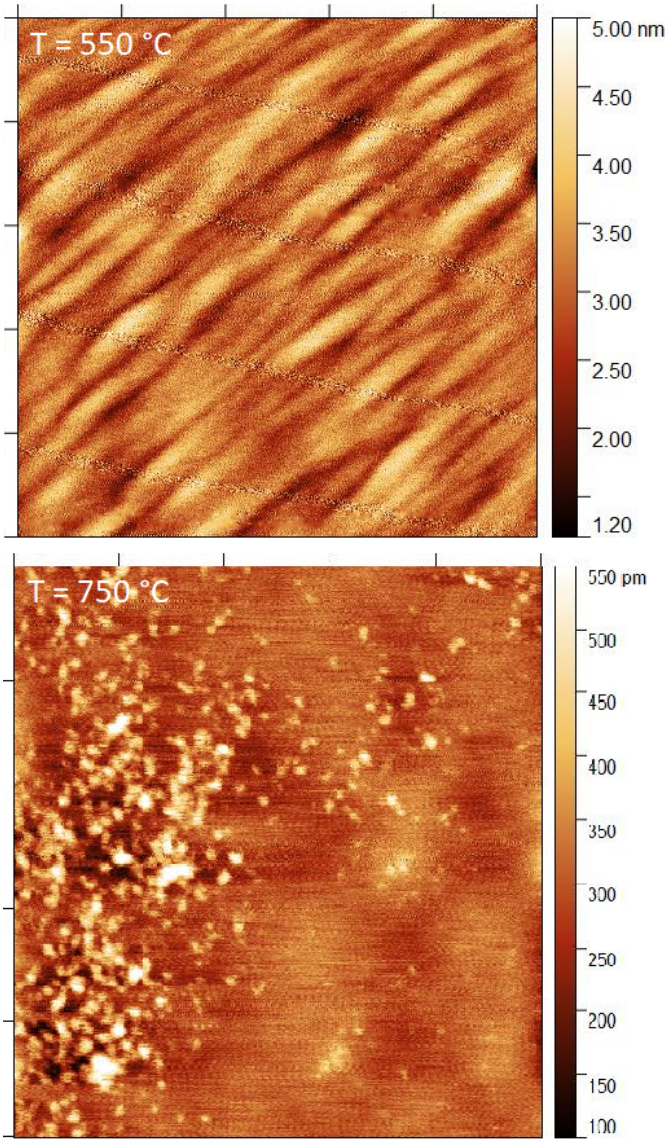

Figure 4.1: AFM images of Si (100) surfaces after HF-etch and PH_3 pre-treatment with the temperature labelled. Both scans were of an area of 500 nm by 500 nm.

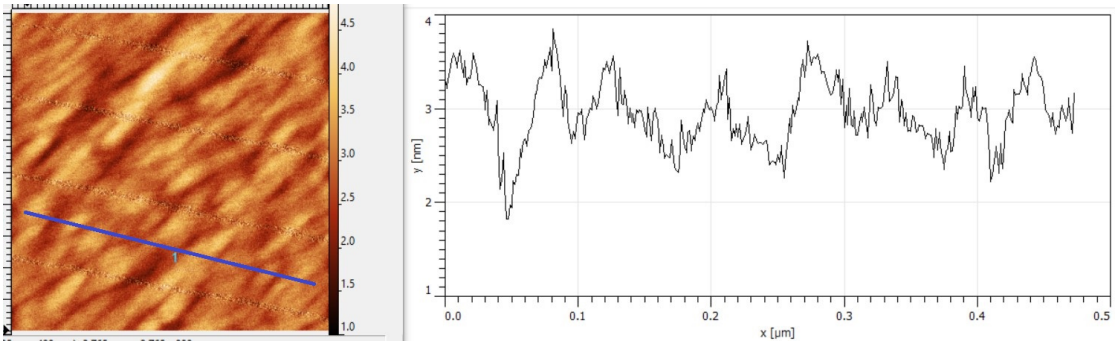

Figure 4.2: 1D height profile along the blue line. AFM image is of pre-treated Si (100) at T_{prep} = 550 °C.

4.2 Si (100)-4° substrate

Similar to the (100) samples, the pre-treatment of Si (100)-4° substrates significantly impacts the substrate surfaces. Figure 4.3 shows the AFM images of the (100)-4° substrate, where the top image (corresponding to T_{prep} = 550 °C) had a RMS roughness of 0.27 nm, and the bottom image (corresponding to T_{prep} = 750 °C) had a RMS roughness of 0.10 nm. Additionally, Figure 4.4 show the 1D height profile along the blue lines of the AFM images. Comparing the pre-treated Si (100) and (100)-4° samples, it is clear that the Si (100)-4° sample at T_{prep} = 550 °C had a smaller height variation (on the order of one monolayer as opposed to two monolayers with the Si (100) sample). Aside from this, the surfaces of both the (100) and (100)-4° substrates looked relatively comparable after the pre-treatment. In contrast, the T_{prep} = 750 °C Si (100)-4° sample seemed to be significantly rougher than that of the (100) specimen.

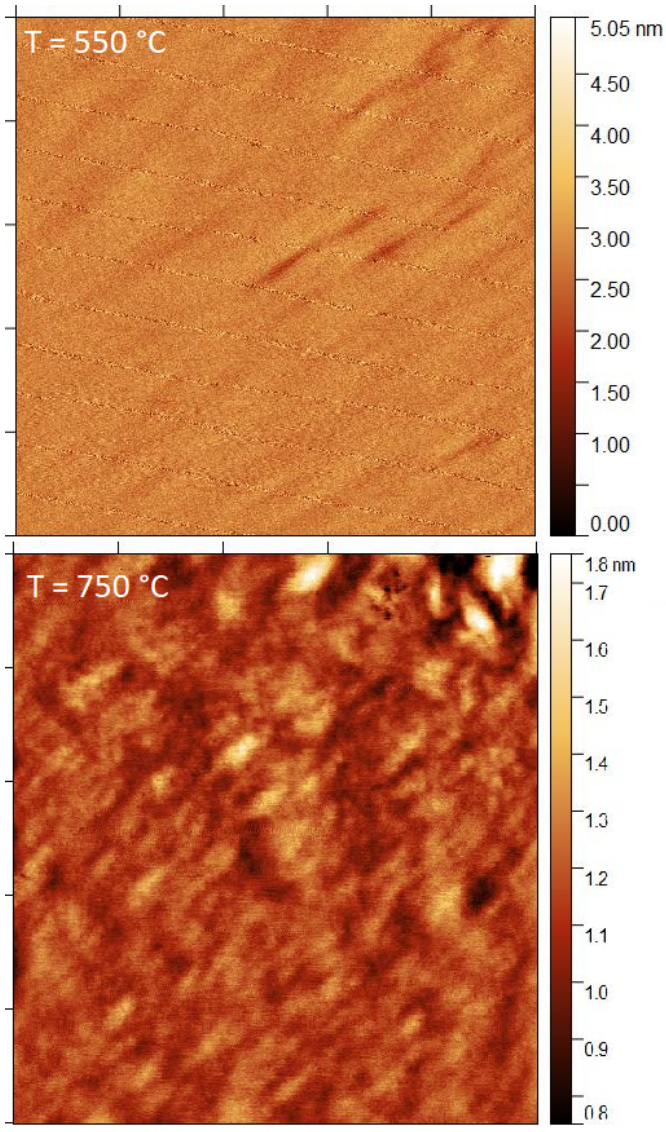

Figure 4.3: Si (100)-4° surfaces after HF-etch and PH_3 pre-treatment with the temperature labelled. Both scans were of an area of 500 nm by 500 nm.

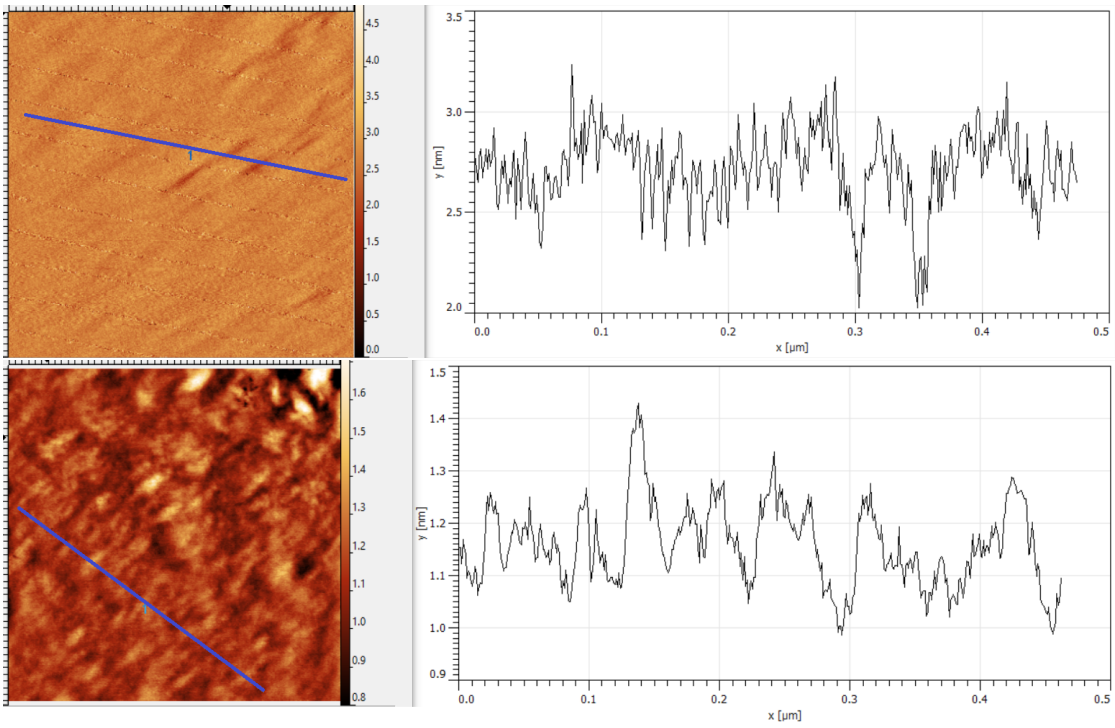

Figure 4.4: 1D height profile along the blue lines. AFM image is of pre-treated Si (100)-4° at T_{prep} = 550 °C (top) and T_{prep} = 750 °C (bottom).

4.3 Si (111) substrate

Lastly is the presentation of the Si (111) substrates. Figure 4.5 shows the AFM images the (111) substrate, where the top image (corresponding to T_{prep} = 550 °C) had a RMS roughness of 0.26 nm and the bottom image (corresponding to T_{prep} = 750 °C) had a RMS roughness of 0.07 nm. Similar to the other T_{prep} = 750 °C surfaces, we can see that the high temperature (111) pre-treatment yielded a surface height range on the order of one monolayer of Si. Comparing the T_{prep} = 550 °C results, we see that the surfaces of (100), (100)-4° and (111) look very similar, with the most significant outlier being the (100) surface. This surface seemed to have significantly more step bunching, with sharp steps well over 1 nm, corresponding to atomic steps of more than two monolayers. In Figure 4.6, the 1D height profile along the T_{prep} = 550 °C (111) sample showed a comparable surface to that of Figure 4.4. This is particularly interesting, as one would expect the more closely related surfaces of (100) and (100)-4° to be more similar after treatment. The low number of atomic terraces can likely explain this on the (100) substrate relative to the (100)-4° one, leading to fewer sites for adatoms to bind.

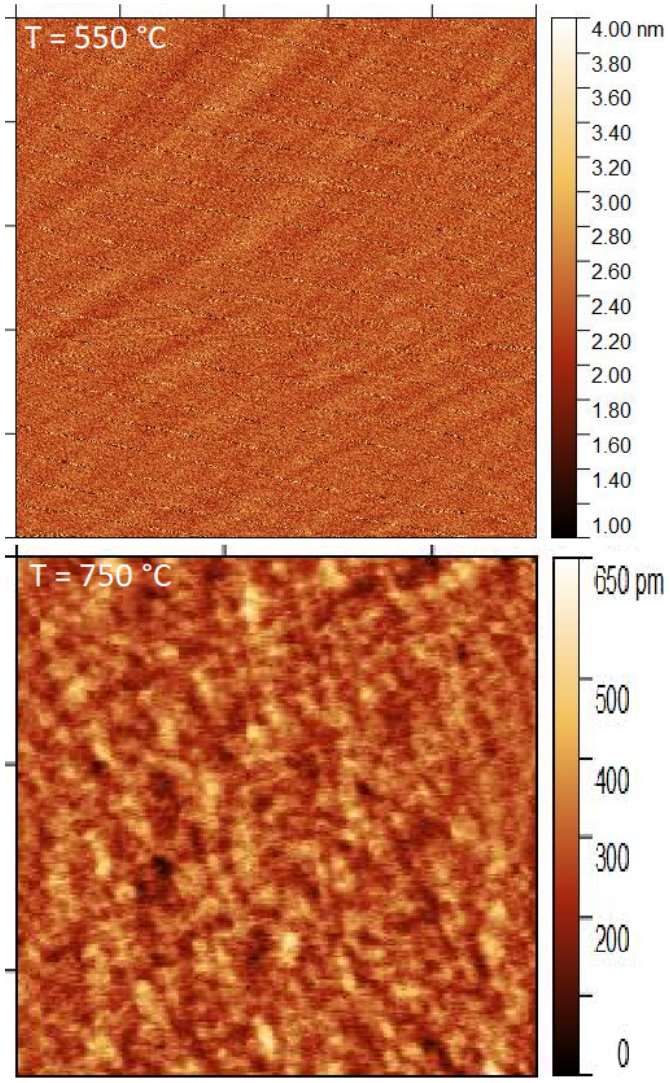

Figure 4.5: Si (111) surfaces after HF-etch and PH_3 pre-treatment with the temperature labelled. Both scans were of an area of 500 nm by 500 nm.

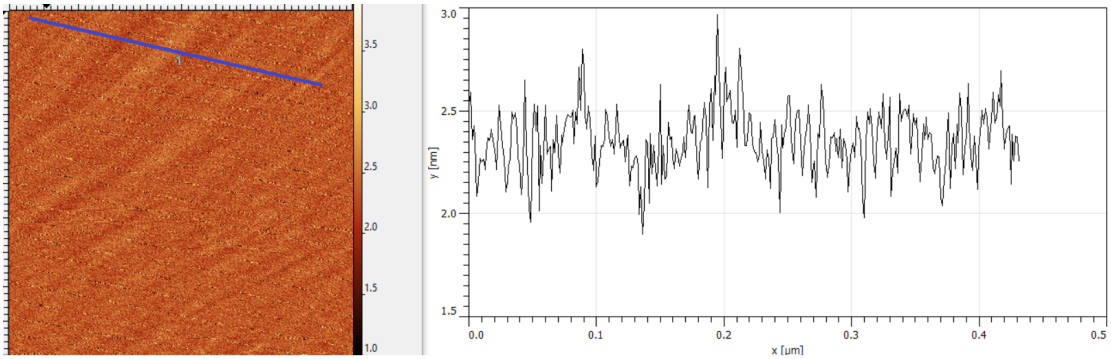

Figure 4.6: 1D height profile along the blue tangent. AFM image is of pre-treated Si (111) at T_{prep} = 550 °C.

Table 4.1 summarizes the results of Sections 4.1, 4.2 and 4.3.

	T = 550 °C	**T = 750 °C**
Si (100)	0.47 nm	0.06 nm
Si (100)-4°	0.27 nm	0.10 nm
Si (111)	0.26 nm	0.07 nm

Table 4.1: Table summarizing the RMS roughness of Si (100), (100)-4°, and (111) substrates at T_{prep} = 550 °C and 750 °C.

4.4 Pre-treated Si pole figures

As an additional step to verify the quality of Si substrates used in the trials, XRD was performed on the pre-treated Si samples. As the pre-treatment predominantly affects the surface of the substrate, the bulk structure of the two different Si pre-treatment temperatures should be comparable. As such, only the Si samples pre-treated at T_{prep} = 750 °C were used for XRD due to time and cost constraints. The pole figures from the 2D XRD data can be seen in Figure 4.7. From the data range collected in these pole figures, there is no evidence of any twinning in the substrates, supporting what would be expected from the starting epi-ready substrate. Thus, the surfaces used for GaP nucleation are of high quality.

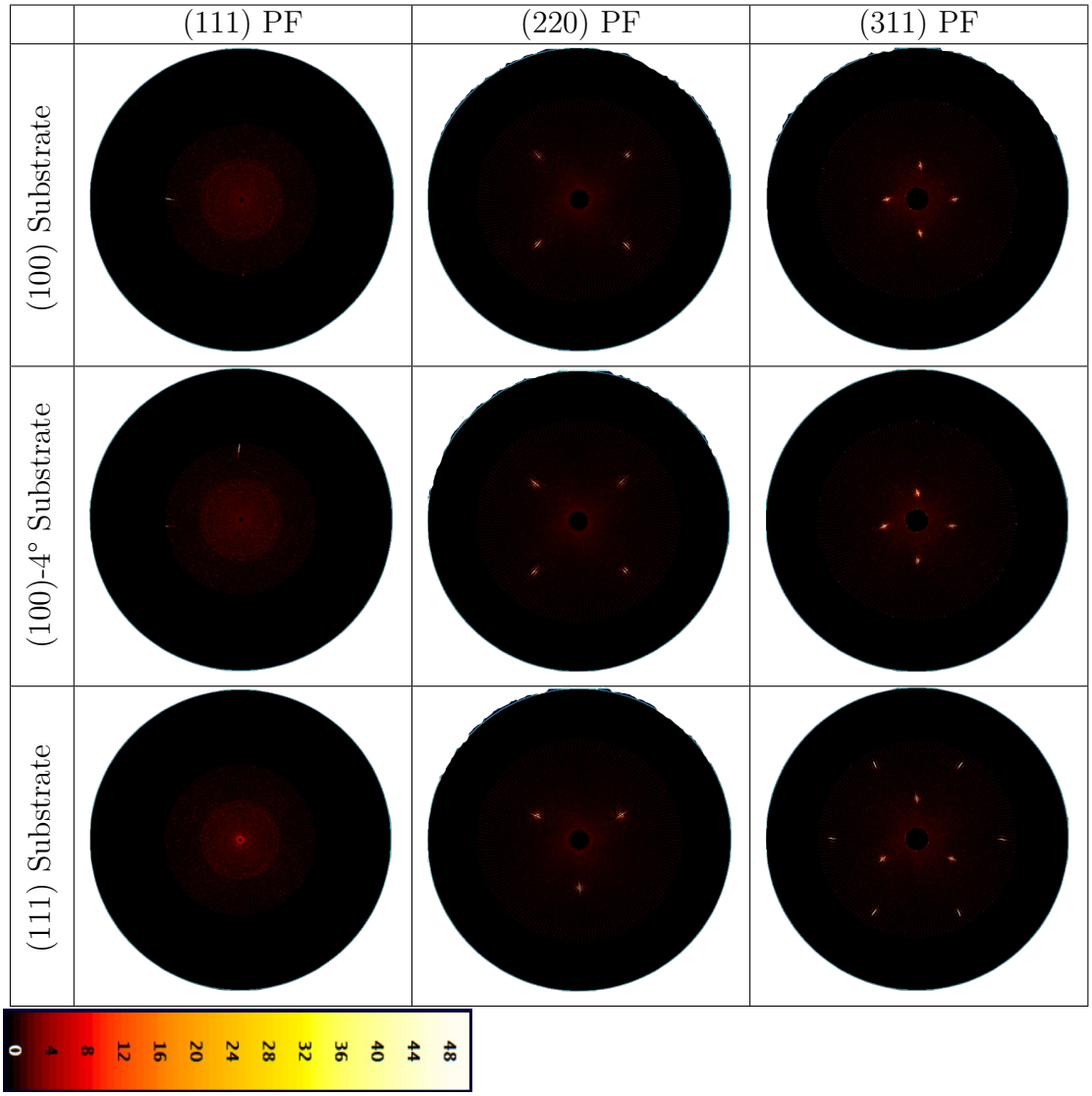

Figure 4.7: Figure of pre-treated Si pole figures, with the first, second, and third columns corresponding to the (111), (220), and (311) pole figures, respectively. The first, second, and third rows correspond to the (100), (100)-4°, and (111) substrates, respectively.

A texture analysis was performed to find how much of the random orientation in subsequent trials can be attributed to air-scattering, based on the assumption that the crystal is of one domain and any supposed random orientation can be attributed to air-scattering. Tables 4.2, 4.3, and 4.4 correspond to pre-treated Si substrates with orientations (100), (100)-4°, and (111), respectively.

Pole Figure	**Main Orientation**	**Random Orientation**
(111)	99.95	0.05
(220)	99.88	0.12
(311)	99.90	0.10

Table 4.2: Texture analysis of the Si (100) substrate from the pole figures.

Pole Figure	**Main Orientation**	**Random Orientation**
(111)	99.92	0.08
(220)	99.94	0.06
(311)	99.91	0.09

Table 4.3: Texture analysis of the Si (100)-4° substrate from the pole figures.

Pole Figure	**Main Orientation**	**Random Orientation**
(111)	85.66*	14.34*
(220)	99.89	0.11
(311)	99.90	0.10

Table 4.4: Texture analysis of the Si (111) substrate from the pole figures. Values denoted with a * are skewed towards random orientations due to limits in the scanning angles reducing the intensity peak detection counts.

Chapter 5

Heteroepitaxy of GaP on Si

This chapter summarizes three exploratory trials into the nucleation of GaP on Si substrates. Substrates used in the following trials are the same as those described in Chapter 4. A PH_3 flow pre-treatment was applied to the substrate prior to growth in an attempt to cover the surface in Si-P bonds. This is a necessary condition for growing QPM heterostructures on Ga-terminating substrates covered in a thin Si film, as the crystal orientation must undergo a lattice reversal.

The growth process started with a PH_3 flow pre-treatment for 5 minutes, followed by a GaP film growth using TMGa and PH_3 for 10 minutes. The precursors, TMGa and PH_3, have flow rates of 80 sccm and 120 sccm for trial 1, 50 sccm and 80 sccm for trial 2, and 80 sccm and 85 sccm for trial 3, respectively. Sections 5.1, 5.2, and 5.3 explore how nucleation varies over three different growth conditions, which are summarized in Table 5.1. Section 5.4 provides a quantitative analysis into twin formations among all specimens and how they compare to one another. Lastly, Section 5.5 discusses key points from trials 1-3.

Trial Number	Pre-treatment Temperature	Growth Temperature
1	550 °C	550 °C
2	750 °C	550 °C
3	750 °C	750 °C

Table 5.1: Table of growth conditions for trials 1-3.

5.1 GaP on Si (100) substrates

SEM images of the GaP films on Si (100) for trials 1-3 can be found in Figures 5.1, 5.2, and 5.3, respectively. A particularly interesting result is the contrast between trial 1 and 2. The difference between trials 1 and 2 is the T_{prep}, with $T_{1,prep} = 550$ °C and $T_{2,prep} = 750$ °C. The result of the different temperature pre-treatment is clearly visible in both quantity and type of nanocrystals forming at the surface. The lower temperature pre-treatment mainly yielded crystallites with diameters of approximately 1 micron and within 1-3 microns of neighbouring crystallites. This is very different than that of the higher temperature pre-treatment, which has significantly sparser nucleation sites, and most nanocrystals forming on the surface are nanowires instead of crystallites. Nanowires have thicknesses on the order of hundreds of nanometers, with smaller thickness towards the tips of the wires. Additionally, the nanowires seem to appear in multiples, branching out from common points. Trial 3 has the same conditions as trial 2, but with $T_{3,growth} = 750$ °C instead of 550 °C. The nanocrystals formed seem to have a similar morphology to that of trial 1, but the diameters seem to be on the order of 5 microns. Additionally, the crystallites formed seem to either be touching neighbouring crystallites (beginning to form a polycrystalline surface, as can be seen as the top of Figure 5.3) or be further spaced out from one another, likely due to the longer diffusion length along the surface due to increased thermal energy.

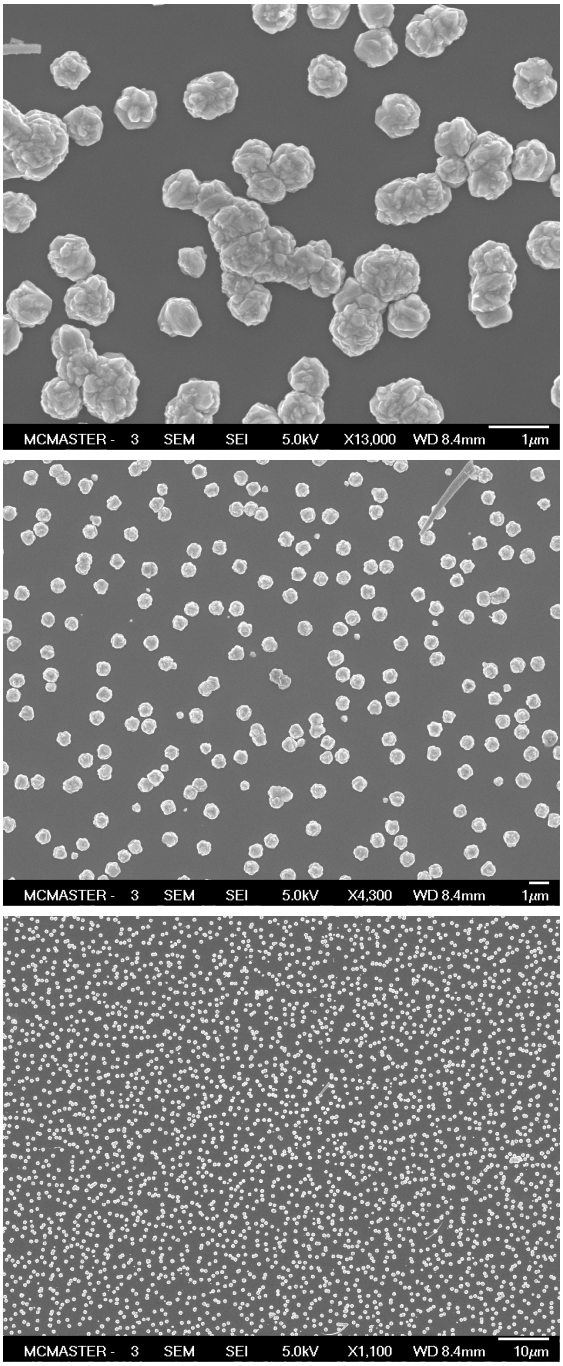

Figure 5.1: SEM images of GaP nucleation on Si (100) (trial 1). T_{prep} = 550 °C, T_{growth} = 550 °C.

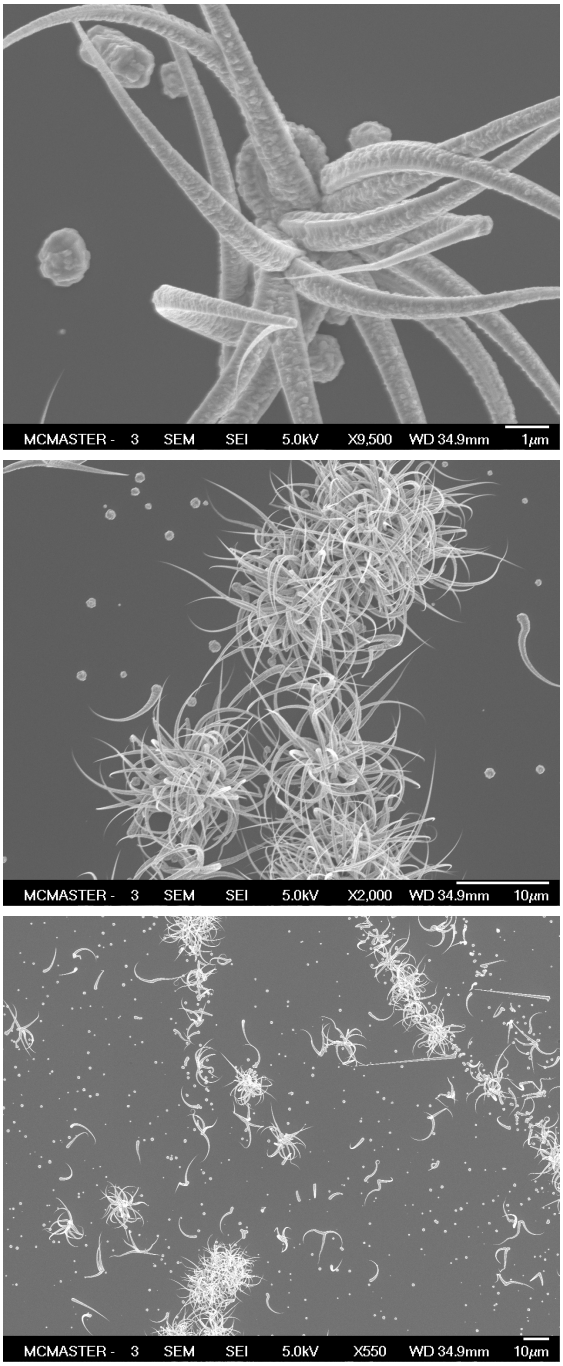

Figure 5.2: SEM images of GaP nucleation on Si (100) (trial 2). T_{prep} = 750 °C, T_{growth} = 550 °C.

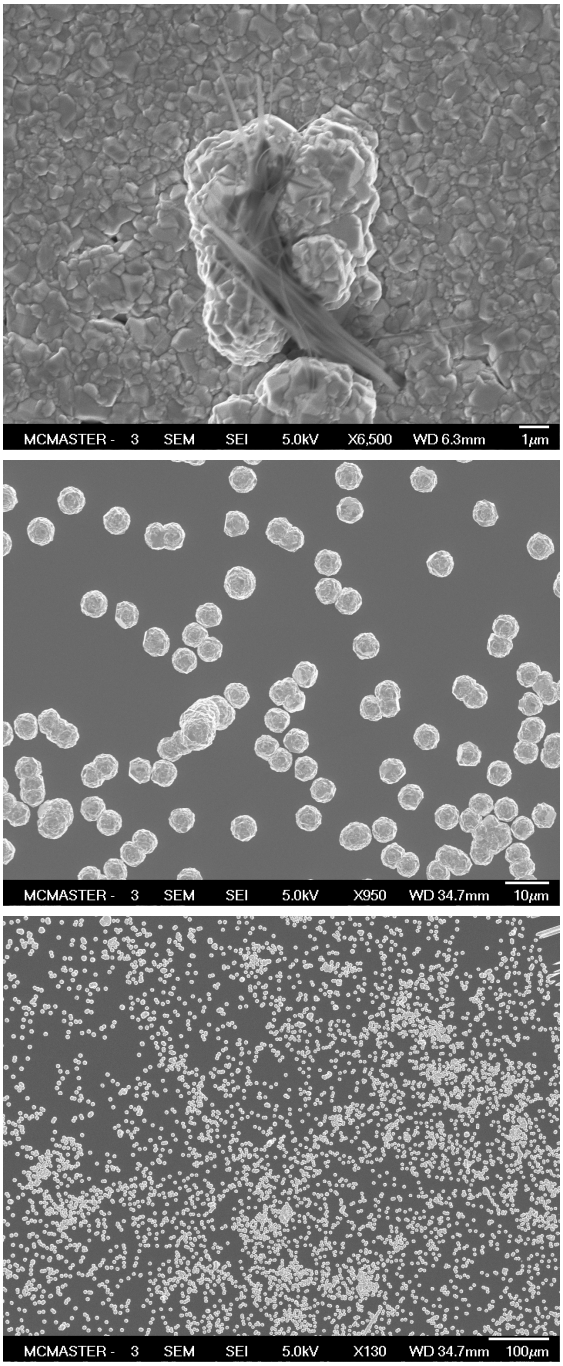

Figure 5.3: SEM images of GaP nucleation on Si (100) (trial 3). T_{prep} = 750 °C, T_{growth} = 750 °C.

5.2 GaP on Si (100)-4° substrates

SEM images of the grown films on Si (100)-4° for trials 1-3 can be found in Figures 5.4, 5.5 and 5.6, and 5.7, respectively. Trials 1 and 3 have macroscopically smooth surfaces from visual inspection; trial 2 has two distinct regions on the grown film, one appearing smooth (Figure 5.5) and the other rough with a dull yellow appearance (Figure 5.6).

Regarding trial 1 in Figure 5.4, a polycrystalline film formed over the surface of the Si substrate with grain sizes on the order of 100 nm. A significant difference exists between the (100) and (100)-4° substrates, as the (100) substrate only appeared to be the nucleation of crystallites instead of a polycrystalline film. For trial 2 ($T_{2,prep}$ = 750 °C) on the (100)-4° substrate in Figure 5.5, the most significant difference to that of the (100) substrate is the emergence of dense crystallites with a variation in diameter ranging from approximately 100 nm to over 1 micron. Additionally, a dense forest of nanowires was observed (Figure 5.6) in a yellow-colored area of the sample. The trial 3 sample of the (100)-4° orientation in Figure 5.7 has a more consistent surface, with large crystallites of approximately 5 µm in diameter. These crystallites have similar distributions along the entire surface of the sample to that of the (100) substrate, but with less bunching of crystallites (which prevents the formation of polycrystalline films).

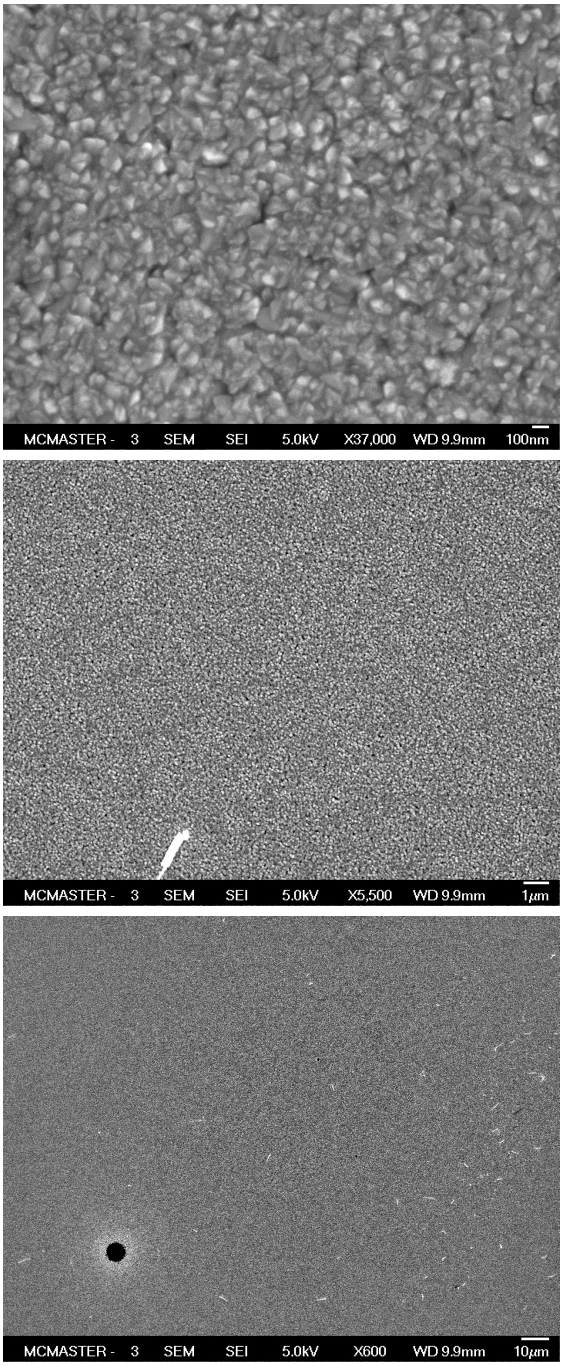

Figure 5.4: SEM images of GaP nucleation on Si (100)-4° (trial 1). T_{prep} = 550 °C, T_{growth} = 550 °C.

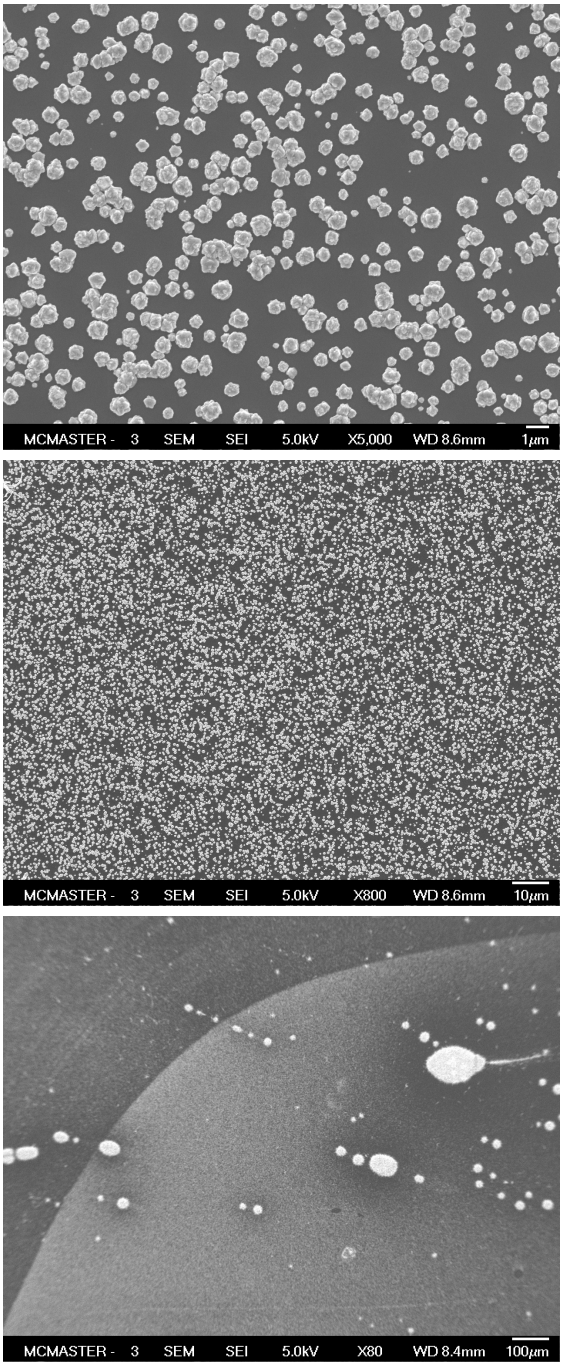

Figure 5.5: SEM images of GaP nucleation on Si (100)-4° (trial 2). $T_{prep} = 750$ °C, $T_{growth} = 550$ °C.

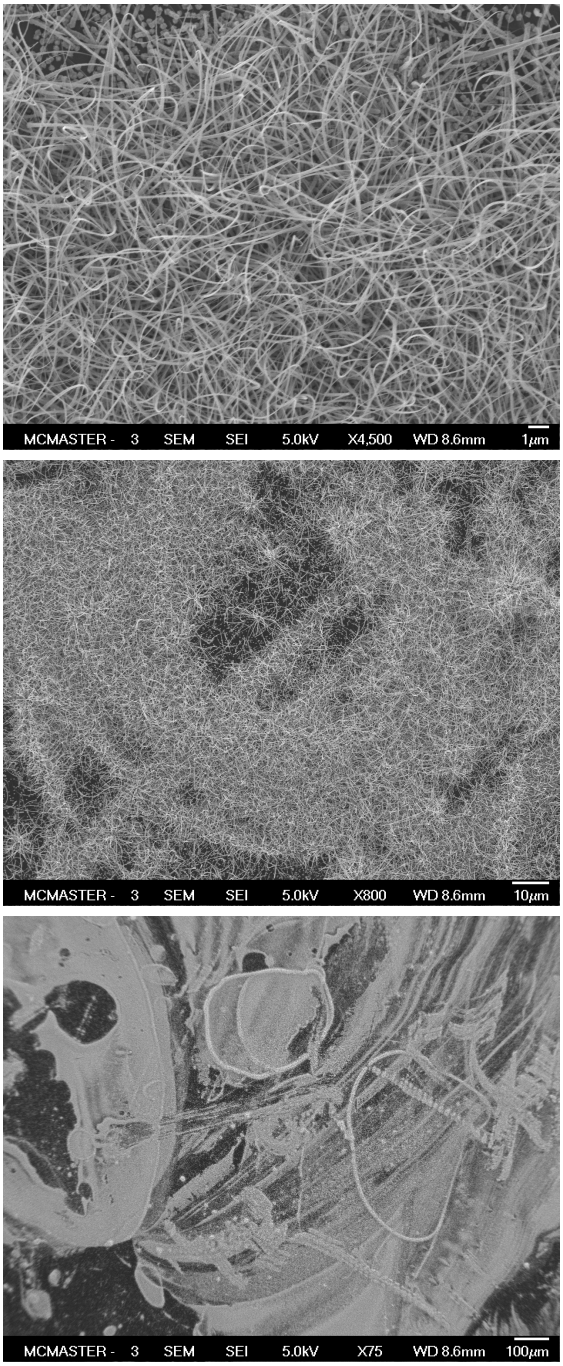

Figure 5.6: SEM images of GaP nucleation on Si (100)-4° (trial 2) focusing on the yellow area. $T_{prep} = 750$ °C, $T_{growth} = 550$ °C.

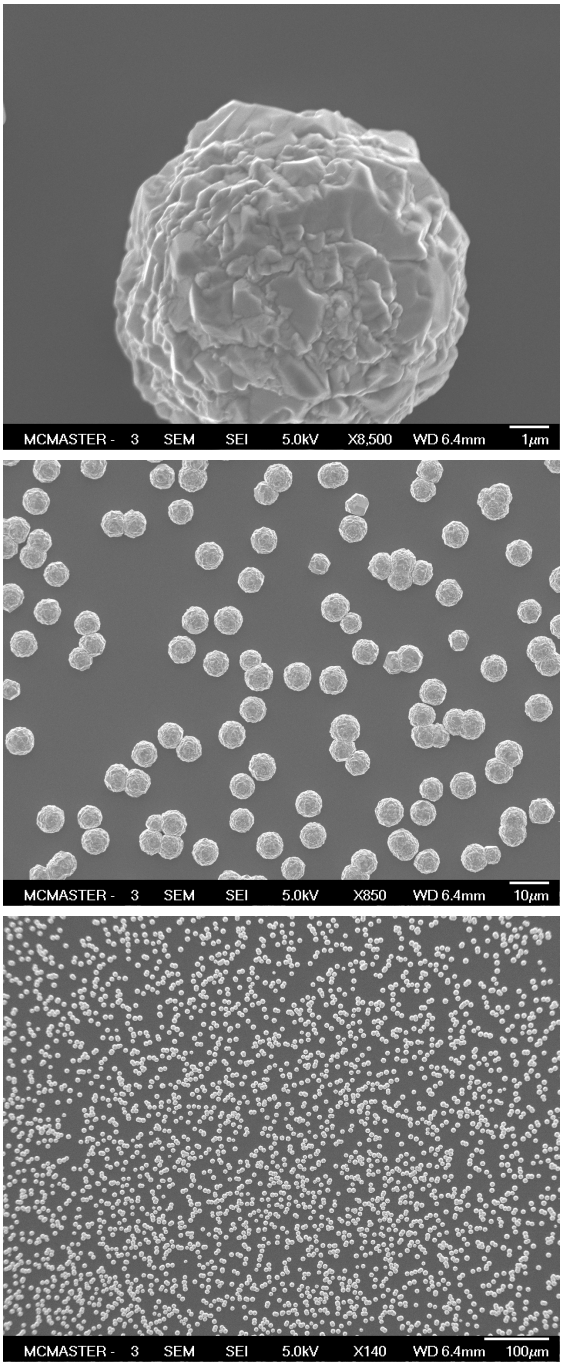

Figure 5.7: SEM images of GaP nucleation on Si (100)-4° (trial 3). T_{prep} = 750 °C, T_{growth} = 750 °C.

5.3 GaP on Si (111) substrates

The Si (111) substrates are of particular interest as they have the most significant variation between trials. Figure 5.8 shows the trial 1 (111) film, with a significant number of nanowires formed. A noteworthy point is they were grown under different conditions (T_{prep} = 550 °C) than those nanowires of the (100) and (100)-4° Si substrates that had T_{prep} = 750 °C. Additionally, these wires seem to have a long range periodicity, with most of the nanowires nucleation sites bunching together in a branching-like pattern as visible in the last image of Figure 5.8. Similar to the previous (100) and (100)-4° nanowires, they seem to originate from a common point. Trial 2 of the (111) substrate in Figure 5.9 was covered on the surface with crystallites of approximately 2 µm in diameter. Although very few on the surface of the material, nanowires like that at the top of Figure 5.9 were found along the surface. In general, the surface has a consistent surface appearance with comparable densities of crystallites. Trial 3 (111) had similar-shaped crystallites to other samples, but with diameters on the order of 10 µm (substantially larger than others). These crystallites seem to cluster together into long chains with widths ranging from 10 µm to larger polycrystalline films, as can be seen at the bottom of Figure 5.10. This is interesting, as it seems to have similarities to the pattern from Figure 5.8, but those surfaces covered in a film with nanowires on top seem to be more faceted as opposed to spherical in shape, which could potentially cause the kinking that developed into nanowires.

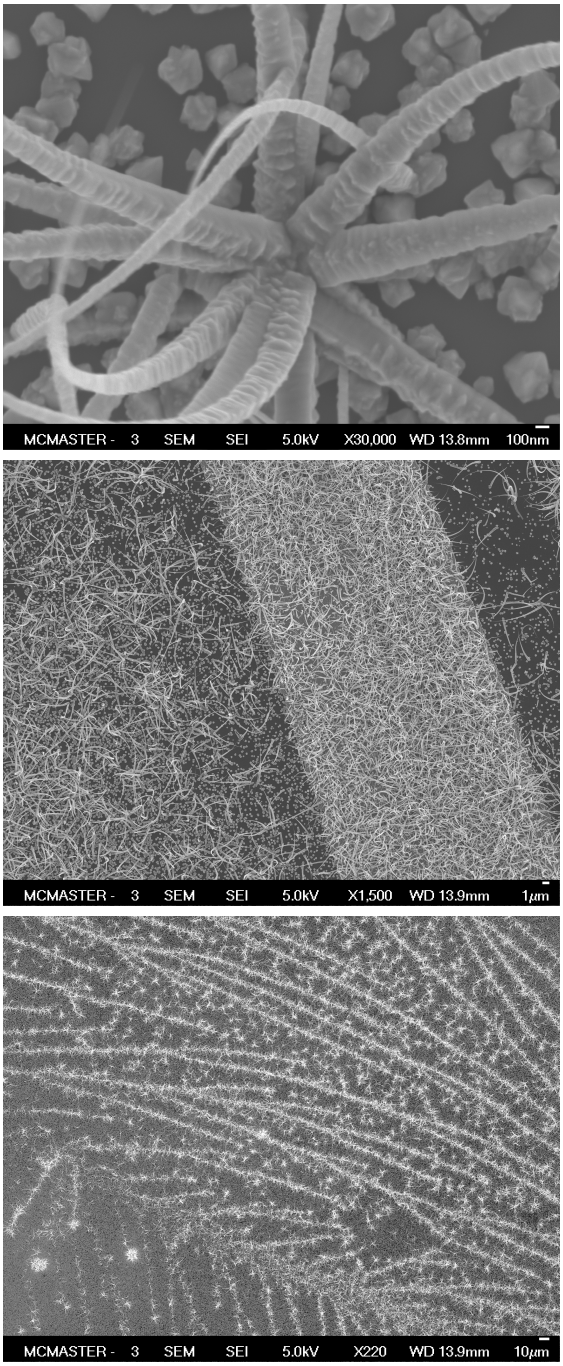

Figure 5.8: SEM images of GaP nucleation on Si (111) (trial 1). $T_{prep} = 550$ °C, $T_{growth} = 550$ °C.

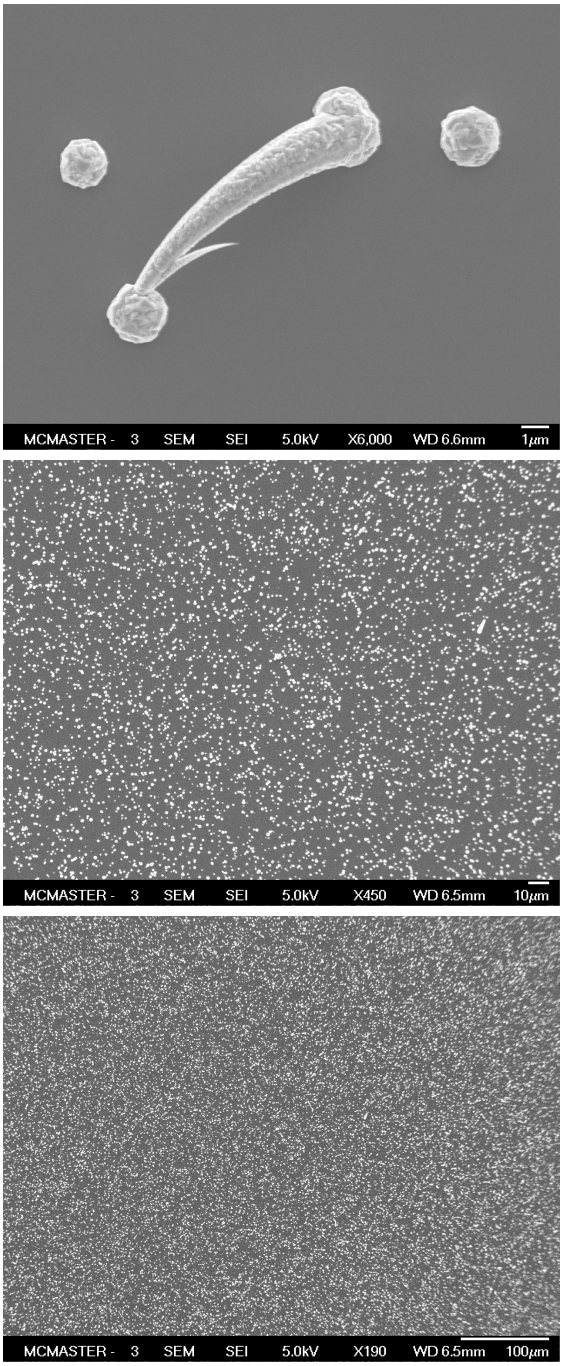

Figure 5.9: SEM images of GaP nucleation on Si (111) (trial 2). T_{prep} = 750 °C, T_{growth} = 550 °C.

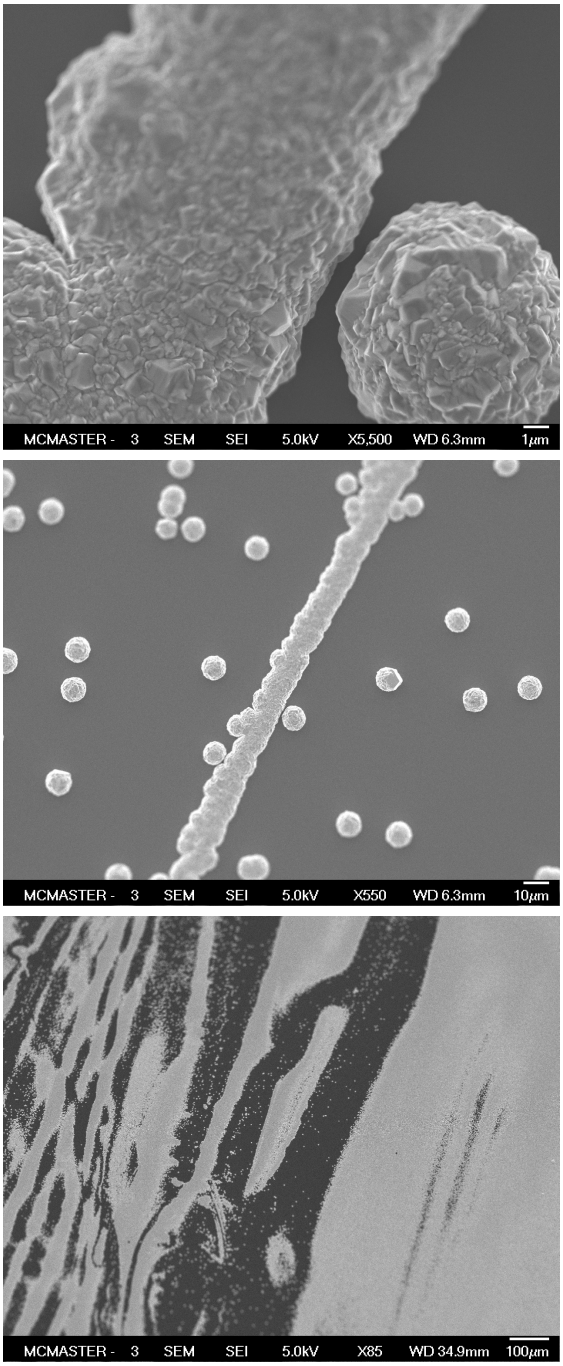

Figure 5.10: SEM images of GaP nucleation on Si (111) (trial 3). T_{prep} = 750 °C, T_{growth} = 750 °C.

5.4 Texture analysis between trials

In this section, the texture analysis of the various GaP on Si samples are presented. As previously mentioned, processing 2D XRD scan data can yield the pole figures of families of planes (in this case, the families (111), (220) and (311)). These pole figures can then be used to find the proportional volume of each crystalline configuration (such as (100) and various twins that emerge during growth). Each unique family of twins has its own respective intensity spots for each pole figure, with some spots overlapping between different families of twins. By deconvolving these intensities into average values pertaining to specific families of planes, these values can be normalized into the fractional volume penetrated by the x-rays. Since the (111), (220), and (311) pole figures are from the same 2D XRD scans, the fractional volume should be consistent between pole figures of the same types of twins.

5.4.1 (100) substrates

Texture data from the (100) substrates are consistent with one another. Trial 1 values are consistent with one another for the (220) and (311) families, with main orientation components of 99.89% and 99.90% and random orientation components of 0.11% and 0.10%. The (111), (220), and (311) texture analysis of trial 2 yields main orientation components of 99.90%, 99.89%, and 99.90% and random orientation components of 0.10%, 0.11%, and 0.10%, respectively. Lastly, the (111), (220), and (311) texture analysis of trial 3 yields main orientation components of 99.46%, 99.78%, and 99.80% and random orientation components of 0.54%, 0.22%, and 0.20%, respectively. The (111) pole figure for trial 1 on the (100) substrate

could not be accurately interpreted as the main intensity peak was cutoff, thus was left empty in Table 5.2. Similarly, the trial 3 (100) texture analysis has a larger random component than other complimentary texture data, likely attributed to the limited scan range leading to a reduced intensity value after data smoothing and integration.

These results seem to be very consistent with one another, meaning trial 1 is approximately 99.90% in the (100) orientation, trial 2 is approximately 99.90% in the (100) orientation, and trial 3 is approximately 99.79% in the (100) orientation. This seems to be consistent with the SEM images, as the trial 1 specimen had nucleation of crystallites but not covering the entire surface, and trial 2 had even sparser nucleation, but with the addition of nanowires growing in various formations. Due to the minimal growth on the surface, it is very likely that a majority of the XRD intensity contributions are from the underlying Si substrate, as the x-rays should have a penetration depth of 10 microns and growth only occurred for 5 minutes. The larger random orientation intensity found in trial 3 can likely be attributed to the larger formations on the surface, with crystallites 5-10 times larger in diameter. Additionally, the clustering of these crystallites together form rough polycrystalline films in some areas on the surface, as previously shown in Figure 5.3. This would likely lead to the increased random orientation intensity (which has contributions from random crystal grains and air-scattering).

Trial	Main Intensity	Random Intensity
1	-	-
2	99.90	0.10
3	99.46	0.54

Table 5.2: Texture analysis on the (100) substrate from the (111) pole figures in Figure 5.11.

Trial	Main Intensity	Random Intensity
1	99.89	0.11
2	99.89	0.11
3	99.78	0.22

Table 5.3: Texture analysis on the (100) substrate from the (220) pole figures in Figure 5.11.

Trial	Main Intensity	Random Intensity
1	99.90	0.10
2	99.90	0.10
3	99.80	0.20

Table 5.4: Texture analysis on the (100) substrate from the (311) pole figures in Figure 5.11.

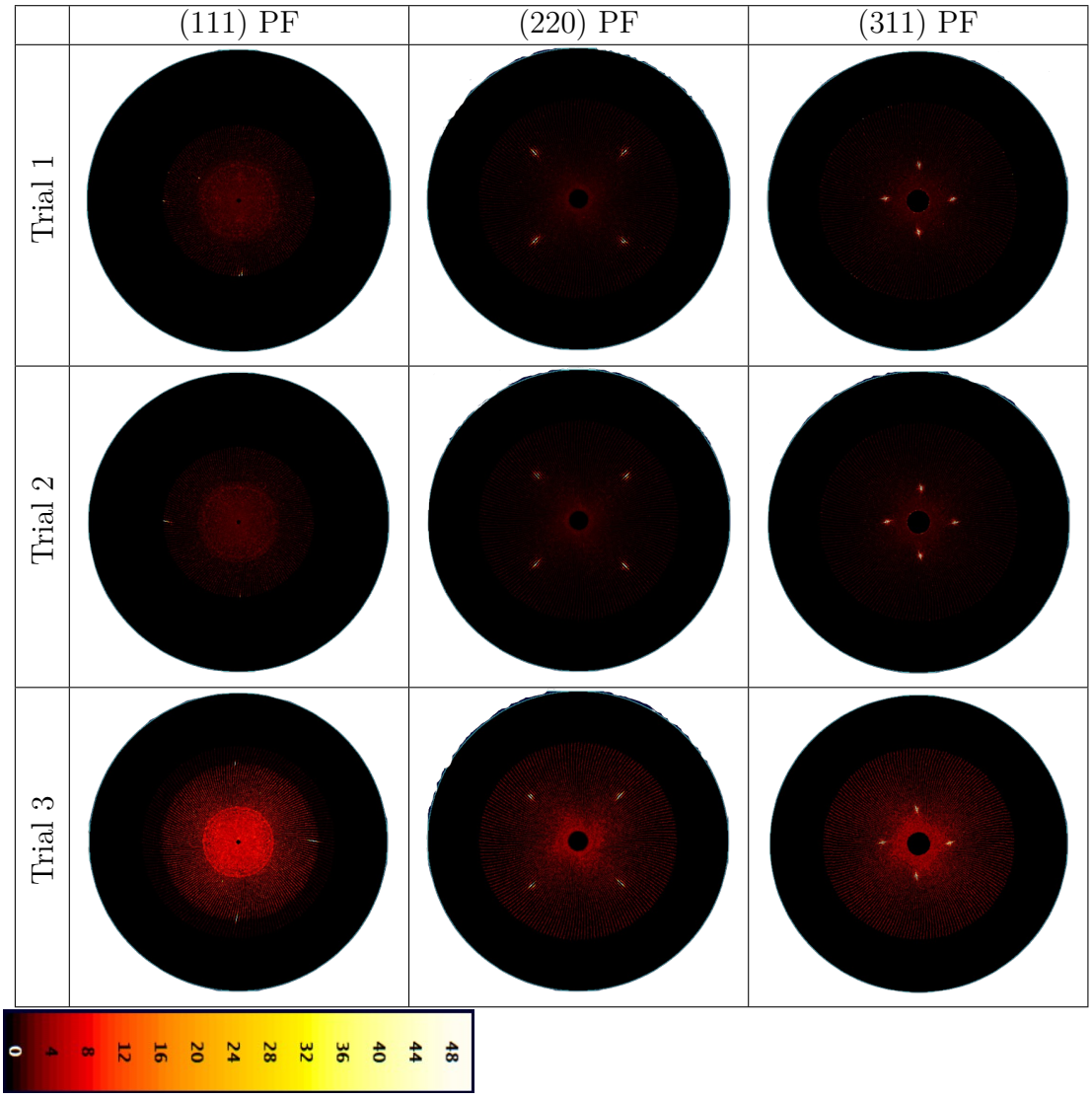

Figure 5.11: Pole figures for trials 1-3 on (100) substrates. Columns going from left to right correspond to the (111), (220), and (311) families of planes, respectively. Rows going top to bottom correspond to trials 1, 2, and 3, respectively. The colour bar at the bottom corresponds to x-ray counts ranging from 0-50.

5.4.2 (100)-4° substrates

The texture analysis of the (100)-4° samples are not as consistent as those from the (100) sample, likely due to the more complicated twinning present and limited x-ray exposure time. Longer exposure times and higher-resolution scans would provide a more accurate image that approximates a smoother distribution. Nonetheless, these results do provide a good basis for a qualitative discussion about twins on the (100)-4° orientation. Trial 1 shows evidence of two different families of twins, denoted types-A and B in the (111), (220), and (311) pole figures, but lack of agreement between the intensities. Trial 2 is similar to trial 1, with two different types of twins but again inconsistencies between the intensities. Trial 3 has significantly more types of twins than trial 1 and 2, with types-A, B, C, D, and E. Types A-D have higher intensities than that of E consistently. Additionally, trial 3 experiments have a higher than normal random orientation, likely not all attributed to the air-scattering found before. The corresponding crystal orientation for each twin can be found in Table 5.8.

Figure 5.13 shows the trial 2 (111), (220) and (311) pole figures with the yellow region. In these figures, the twin families show substantially weaker intensities. This is as expected, as the trial 2 (100)-4° yellow region shows nanowires kinking in what seems like random orientations, leading to an increase in the random signal intensity and a decrease to the twin intensities.

Trial	Main	Type-A	Type-B	Type-C	Type-D	Type-E	Rand
1	98.70	1.18	0.08	-	-	-	0.04
2	99.62	0.31	-	-	-	-	0.07
3	93.54*	3.53*	1.53*	0.50*	0.44*	0.22*	0.25*

Table 5.5: Texture analysis on the (100)-4° substrate from the (111) pole figures in Figure 5.12. Values denoted with a * are skewed towards random orientations due to limits in the scanning angles reducing the intensity peak detection counts.

Trial	Main	Type-A	Type-B	Type-C	Type-D	Type-E	Rand
1	98.72	0.81	0.35	-	-	-	0.12
2	99.88	0.05	0.03	-	-	-	0.03
3	97.65	0.23	1.12	0.50	0.32	-	0.19

Table 5.6: Texture analysis on the (100)-4° substrate from the (220) pole figures in Figure 5.12.

Trial	Main	Type-A	Type-B	Type-C	Type-D	Type-E	Rand
1	99.33	0.15	0.42	-	-	-	0.10
2	99.85	-	0.06	-	-	-	0.09
3	98.31	0.54	-	0.24	0.61	0.17	0.14

Table 5.7: Texture analysis on the (100)-4° substrate from the (311) pole figures in Figure 5.12.

Twin Type	111 PF	220 PF	311 PF
Main	<1 0 0>	<1 0 0>	<1 0 0>
Type-A (T1,T2,T4)	<1 2 2>	<1 2 2>	<1 1 2>
Type-A (T3)	<1 2 2>	<1 2 2>	<0 1 4>
Type-B (T1,T2,T4)	<1 3 7>	<1 1 2>	<1 2 2>
Type-B (T3)	<1 3 7>	<1 2 3>	
Type-C (T3)	<0 1 2>	<1 4 16>	<1 1 2>
Type-D	<1 2 3>	<0 1 3>	<1 5 9>
Type-E	<1 3 5>		<1 2 7>

Table 5.8: Crystal orientations corresponding to each family of twins on (100) and (100)-4° substrates.

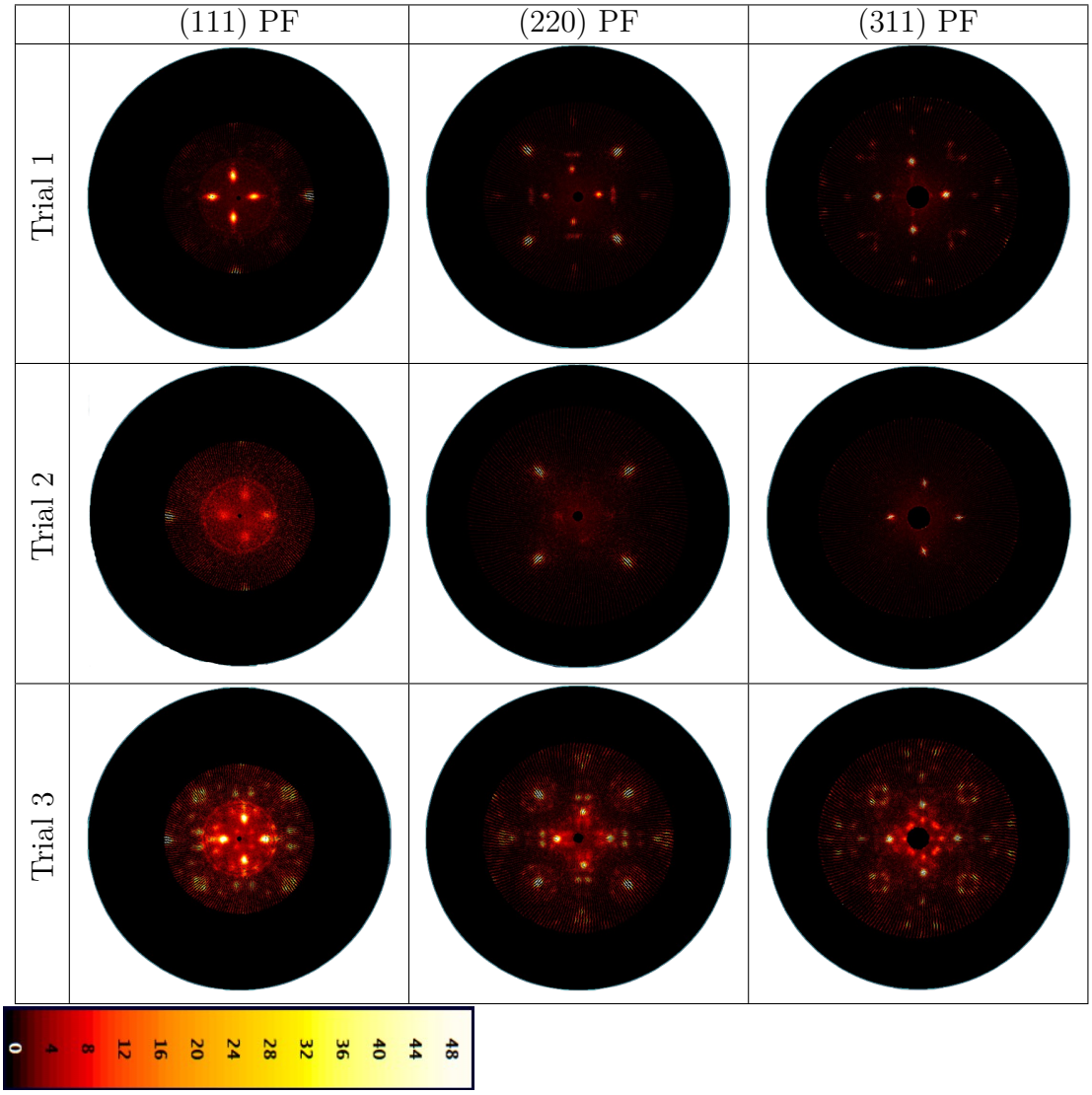

Figure 5.12: Pole figures for trials 1-3 on (100)-4° substrates. Columns going from left to right correspond to the (111), (220), and (311) families of planes, respectively. Rows going top to bottom correspond to trials 1-3, respectively. The colour bar at the bottom corresponds to x-ray counts ranging from 0-50.

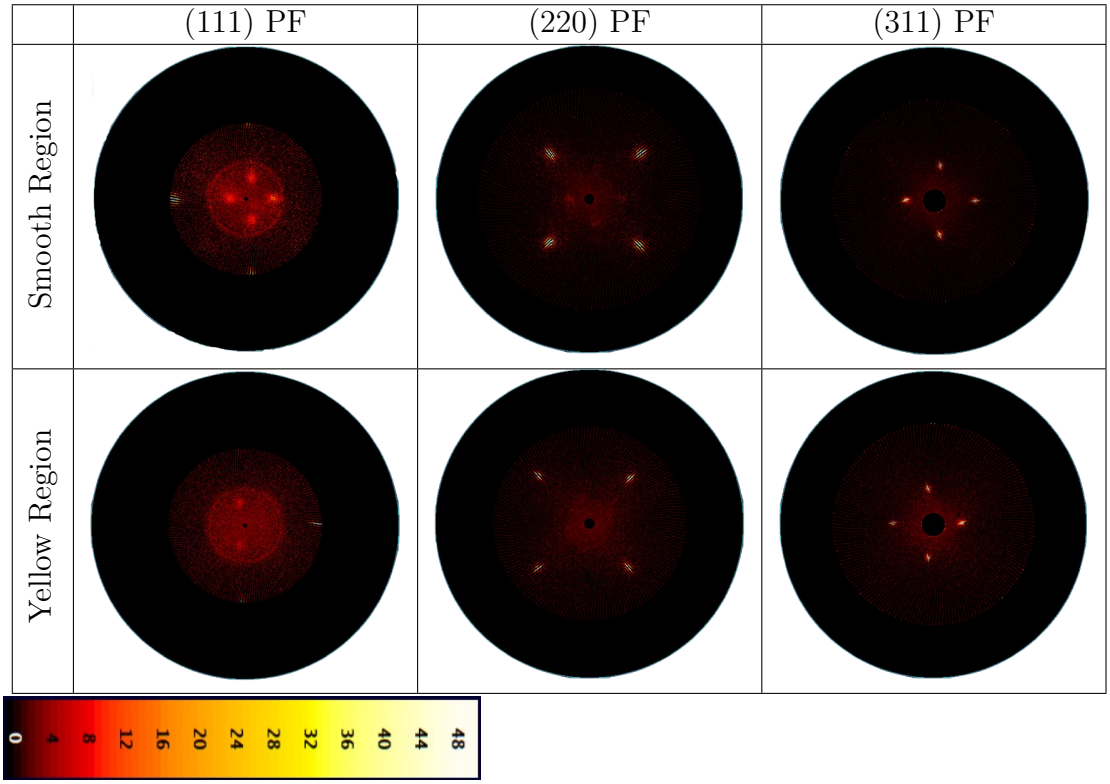

Figure 5.13: Pole figures for trial 2 on (100)-4° substrate focusing on the yellow region. Columns going from left to right correspond to the (111), (220), and (311) families of planes, respectively. Top row corresponds to the smooth region (same as the top row of Figure 5.12) and the bottom row corresponds to the yellow region. The colour bar at the bottom corresponds to x-ray counts ranging from 0-50.

5.4.3 (111) substrates

The (111) substrate has some variation between the trials, but enough consistency for adequate qualitative analysis. Trial 1 shows the most twins, with four different twins showing a significant contribution in the (111) pole figure. Trial 1 pole figures for the (220) and (311) family of planes both have variations in type-C and type-D twin intensities, with the type-D intensities not visible in the (311) pole figure. An average between the (220) and (311) pole figures yield a main texture component (corresponding to the (111) orientation) of 99.35%, type-A texture of 0.32%, type-B texture of 0.20%, type-C of 0.06%, and random component of 0.09%. The lack of type-C and type-D twins in (220) and (311) figures is likely due to the low intensity being too small to detect. Trial 2 has small twin intensities, type-A and type-B, where type-A has a higher intensity that is on par with the random orientation and slightly more prominent than type-B. Using trial 2 (220) and (311) pole figures as the reference, the texture analysis yields: (111) texture of 99.73%, type-A texture of 0.10%, type-B texture of 0.02%, and random component of 0.11%. Lastly, trial 3 shows no twins but a higher random component, with the fractional intensities corresponding to a (111) texture of 99.73% and a random texture of 0.28%.

Trial	Main	Type-A	Type-B	Type-C	Type-D	Random
1	66.38*	16.10*	7.72*	4.22*	2.53*	3.06*
2	72.33*	11.12*	10.80*	-	-	5.75*
3	61.62*	-	-	-	-	38.38*

Table 5.9: Texture analysis on the (111) substrate from the (111) pole figures in Figure 5.14. Values denoted with a * are skewed towards random orientations due to limits in the scanning angles reducing the intensity peak detection counts.

Trial	Main	Type-A	Type-B	Type-C	Type-D	Random
1	99.31	0.30	0.21	0.11	-	0.07
2	99.78	0.12	-	-	-	0.11
3	99.78	-	-	-	-	0.22

Table 5.10: Texture analysis on the (111) substrate from the (220) pole figures in Figure 5.14.

Trial	Main	Type-A	Type-B	Type-C	Type-D	Random
1	99.38	0.33	0.18	-	-	0.11
2	99.79	0.07	0.04	-	-	0.10
3	99.67	-	-	-	-	0.33

Table 5.11: Texture analysis on the (111) substrate from the (311) pole figures in Figure 5.14.

Twin Type	111 PF	220 PF	311 PF
Main	<1 1 1>	<1 1 1> (bright spots)	<1 1 1>
Type-A	<0 1 2> (bright spots)	<1 1 1> (60°/180° rotation along [111])	<1 1 1> (60°/180° rotation along [111])
Type-B	<0 1 2> (weak spots)	<1 1 5> (bright spots)	<1 1 5>
Type-C	<1 1 3> (bright spots)	<1 1 5> (60°/180° rotation along [111])	
Type-D	<1 1 3> (weak spots)		

Table 5.12: Crystal orientations corresponding to each family of twins on (111) substrates.

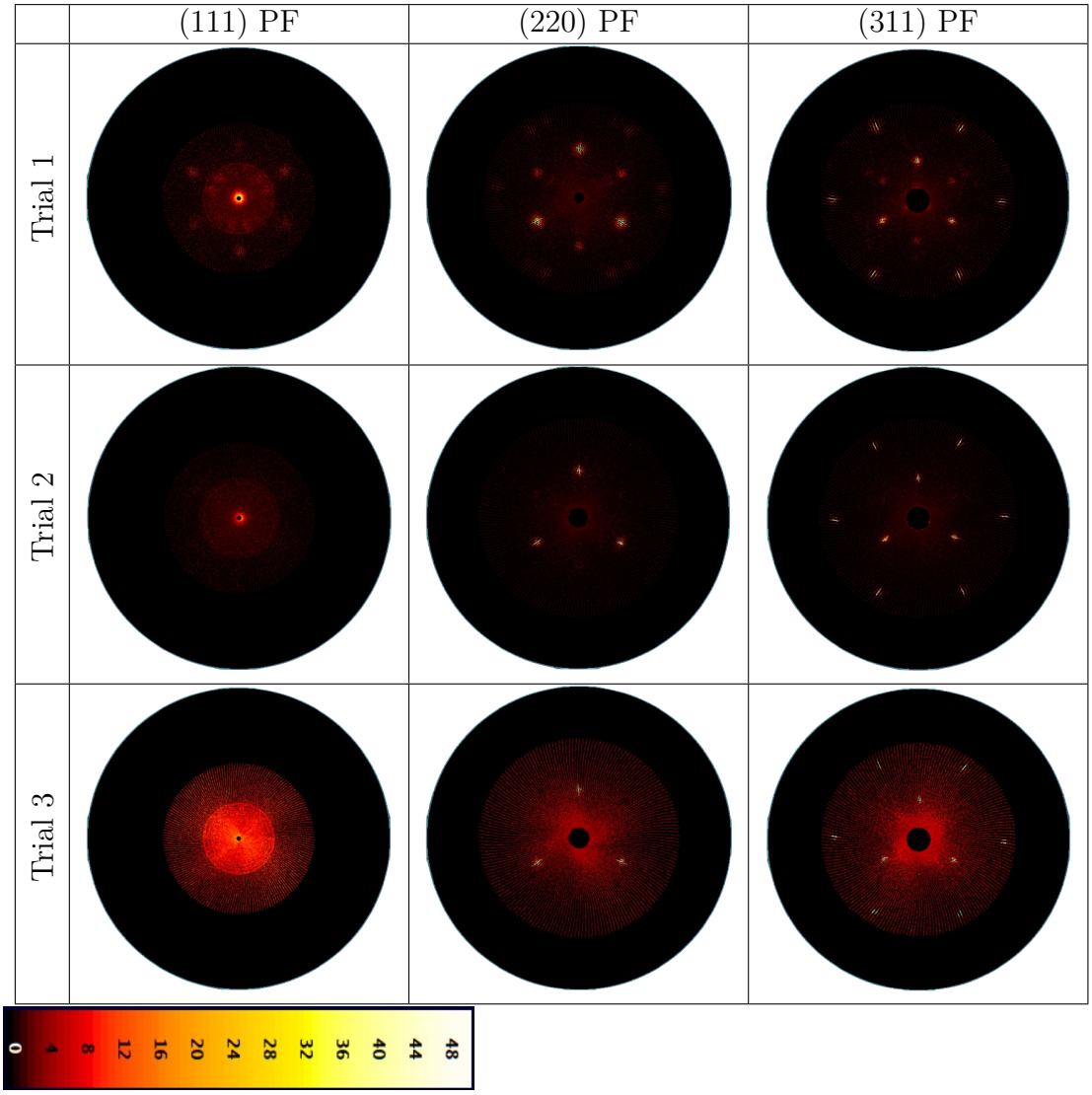

Figure 5.14: Pole figures for trials 1-3 on (111) substrates. Columns going from left to right correspond to the (111), (220), and (311) families of planes, respectively. Rows going top to bottom correspond to trials 1, 2, and 3, respectively. The colour bar at the bottom corresponds to x-ray counts ranging from 0-50.

5.5 Conclusion

The MOCVD growth of GaP on Si substrates was investigated under various growth conditions and substrate orientations (Si (100), (100)-4°, (111)). Si surfaces were pre-treated with PH_3, followed by subsequent growth with TMGa and PH_3. Three different growth conditions were used: 1) pre-treatment at 550 °C, growth at 550 °C, 2) pre-treatment at 750 °C, growth at 550 °C, and 3) pre-treatment at 750 °C, growth at 750 °C. XRD analysis and SEM imaging found that trial 2 yields the optimal nucleation of GaP on Si as it has the least amount of twinning and would be ideal for creating a single domain layer during further growth.

The (100) substrate showed little to no signs of twinning, likely due to the small grains formed on the surface (visible by SEM), meaning that most of this intensity is likely that of the Si substrate. Substrates (100)-4° and (111) both showed evidence of substantially more nucleation than (100) and appeared to be suitable candidates for further investigation. An additional interesting point is the formation of GaP nanowires on the surfaces of (100) and (100)-4° under the trial 2 conditions, and the (111) surface under the trial 1 conditions. A possible explanation for this is the presence of an oxide layer on the sample. The samples were etched with 1:10 HF before growth as thermal treatment at 550 °C would not remove an oxide surface [23]. Although the oxide layer should be removed, the short time between etching and loading the samples gives the possibility for an oxide layer to start reforming.

Chapter 6

Heteroepitaxy of GaP on Si with Sb as a surfactant

This section explores the affects of Sb deposition immediately prior to GaP on Si deposition. The growth recipe for trial 4 uses the same conditions as those of trial 1 ($T_{4,prep} = 550\ ^{\circ}C$ and $T_{4,prep} = 550\ ^{\circ}C$), with the addition of 5 seconds of TMSb deposition. Substrates used in the following trials are the same as those described in Chapter 4. The precursors, TMGa, TMSb, and PH_3, have flow rates of 80 sccm, 40 sccm, and 100 sccm for trial 4, respectively. Section 6.1 explores the SEM images of the polycrystalline films. Section 6.2 presents the texture analysis results from the generated XRD pole figures. Lastly, Section 6.3 summarizes the results of trial 4.

6.1 SEM images

SEM images of the grown films on Si (100), (100)-4° and (111) are found in Figures 6.1, 6.2, and 6.3, respectively. Significant conclusions can be drawn comparing trial 1 and 4 results. The Si (100) substrate has significant difference in the film's surface structure with the addition of Sb. Unlike the trial 1 results in Figure 5.1 with under 50% surface coverage in nucleating grains, the surface is nearly covered with GaP grains. Both samples show some nanowires present, with a much higher density on the trial 4 substrate. Grains on the (100) trial 4 sample appear smaller than those from trial 1, more similar to those on the trial 1 (100)-4° substrate. The difference between trial 1 and 4 on (100)-4° substrates is less significant. Trial 1 yielded a fairly smooth surface macroscopically, with densely packed grains covering the entire surface with diameters on the scale on 100 nm, as visible in Figure 5.4. Trial 1 also showed few (but some) nanowires present on the surface. Similarly, trial 4 shows grains and nanowires of a similar size and similar density. One noticeable difference is the emergence of a small region of dense nanowire nucleation, as shown in the second top image of Figure 6.2. The most significant difference between trial 1 and 4 is from the (111) substrate. Trial 1 (111) yielded a surface with long-range patterns of dense and sparse crystallite nucleation and covered in nanowires, as seen in Figure 5.8. In contrast, the large-scale pattern of non-uniform nucleation densities is almost completely eradicated in trial 4, with what looks like a related pattern visible in the top of Figure 6.3. Additionally, the nucleation density seems consistent along the entire surface of the specimen, with very few nanowires formed. This would support the original hypothesis for using Sb as a surfactant - reducing diffusion length and increasing nucleation density.

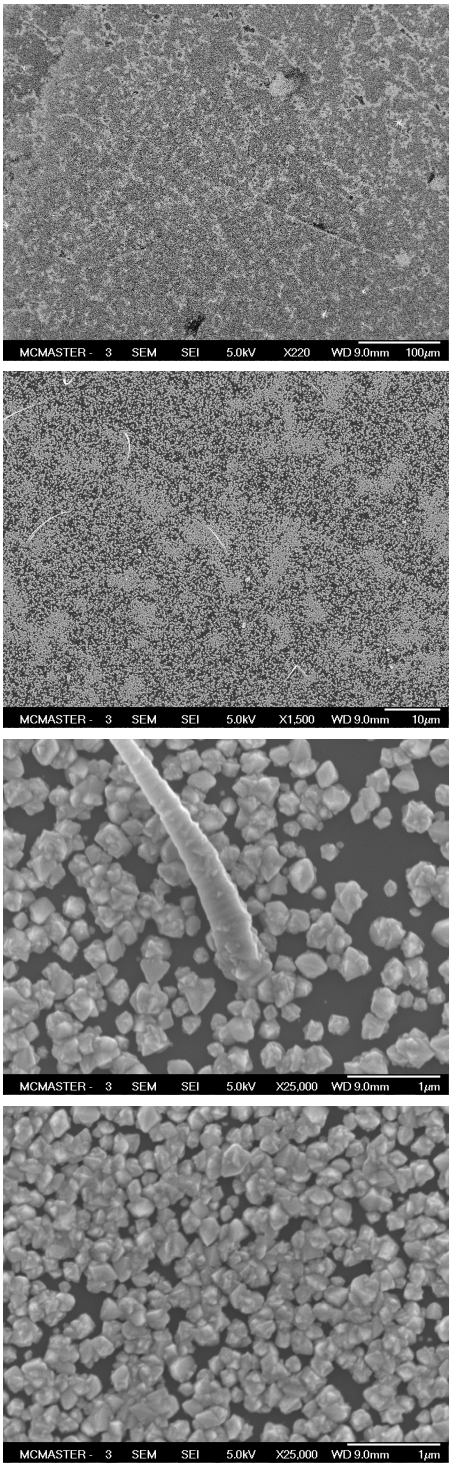

Figure 6.1: SEM images of GaP nucleation on Si (100) (trial 4). Same conditions as trial 1, with the addition of 5 s antimony deposition.

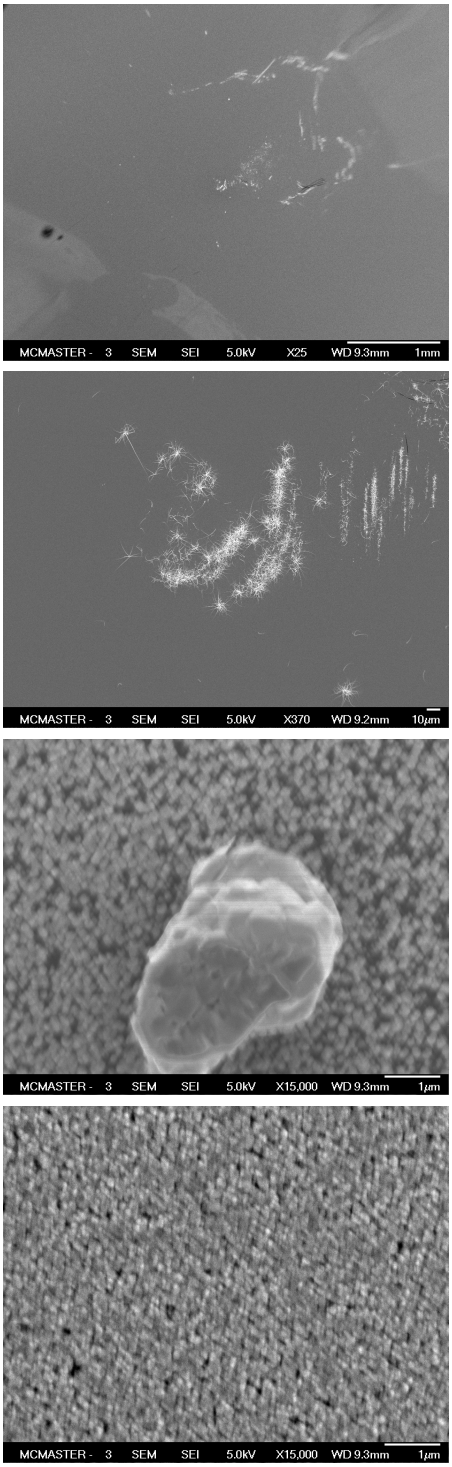

Figure 6.2: SEM images of GaP nucleation on Si (100)-4° (trial 4). Same conditions as trial 1, with the addition of 5 s antimony deposition.

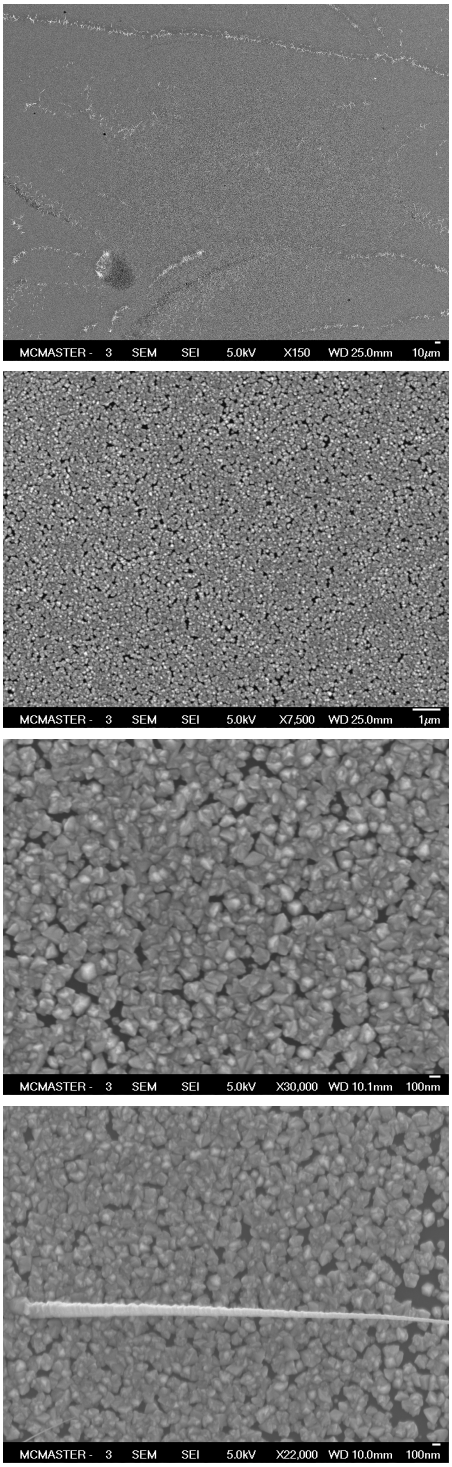

Figure 6.3: SEM images of GaP nucleation on Si (111) (trial 4). Same conditions as trial 1, with the addition of 5 s antimony deposition.

6.2 Texture analysis

The (111) pole figure data was cut off near the main peak intensity, similar to those from the previous section, thus only the (220) and (311) pole figures are used in the fractional calculation. Trial 4 (100) has a main orientation texture of 99.59%, type-A texture of 0.19%, type-B texture of 0.13%, and random component of 0.10%. Its worth noting that there was fairly significant variation between the texture analysis of the (220) and (311) pole figures (which would ideally be the same), so the results are more appropriately treated qualitatively until higher resolution scans can be conducted. The key takeaway is the significant presence of the type-A and type-B twins. The trial 4 (100)-4° sample has a stronger type-A and type-B component than that of the (100), with the averaged fractional components of the main, type-A, type-B and random orientations being 99.24%, 0.37%, 0.32%, and 0.08%, respectively. Again, the significant difference between the (220) and (311) pole figures make these results more appropriate as a qualitative analysis, with a presence of both type-A and type-B orientations. Lastly, the trial 4 (111) substrate showed a higher consistency than that of the other two orientations. The type-C twins present in the (311) pole figure do not appear in the (220) to a significant level, hence they are neglected due to the low intensity. Averaging the (220) and (311) figures, the fractional components of the main, type-A, type-B, type-C, and random orientations are 99.31%, 0.37%, 0.18%, 0.07%, and 0.09%, respectively. Good agreement between the (220) and (311) pole figures allow for quantitative interpretation of these results, meaning there is approximately twice as much of type-A than type-B, and likewise with type-B to type-C.

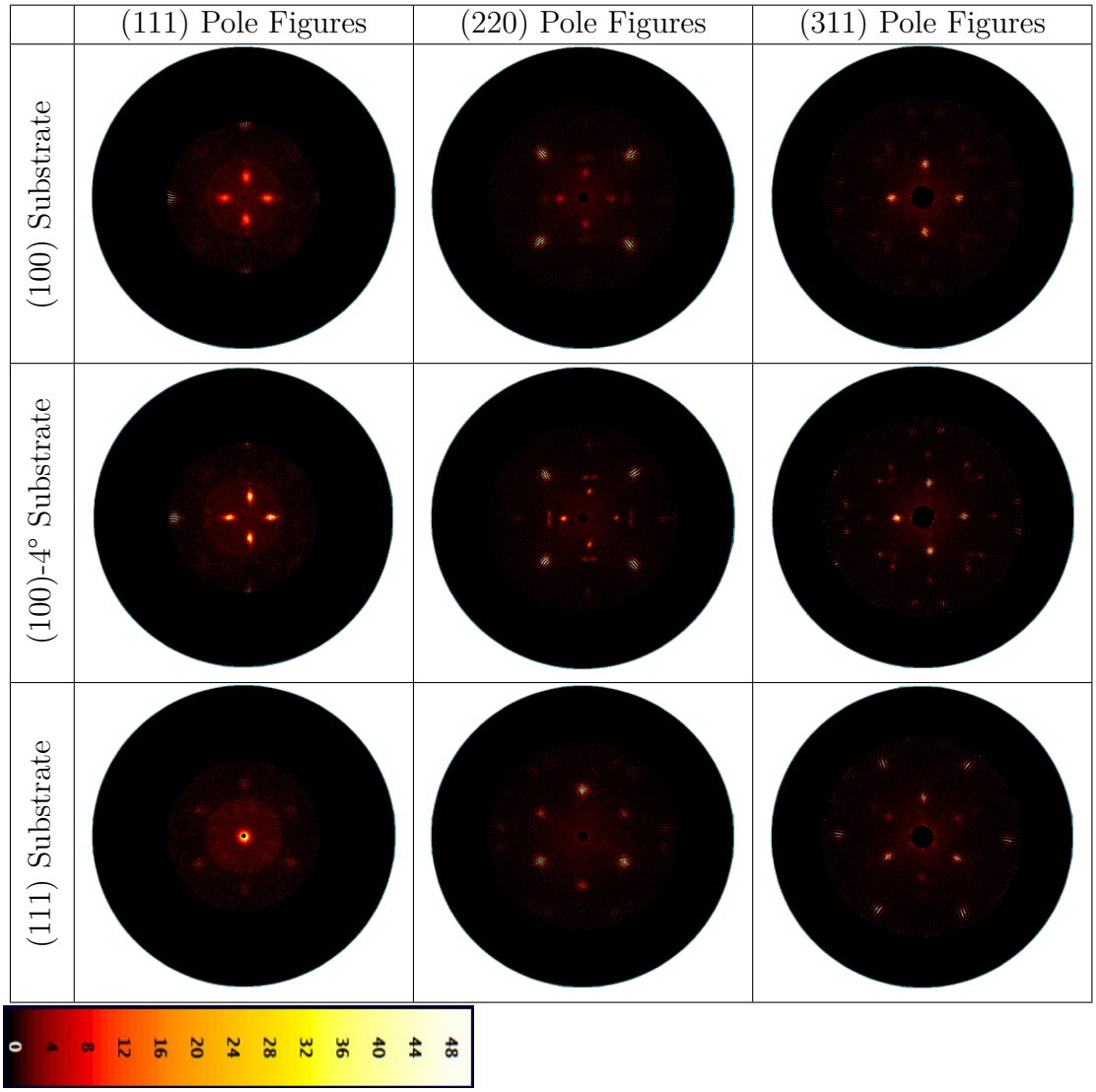

Figure 6.4: Pole figures for trial 4 on (100), (100)-4°, and (111) substrates. Columns going from left to right correspond to the (111), (220), and (311) families of planes, respectively. Rows going top to bottom correspond to substrates (100), (100)-4°, and (111), respectively. The colour bar at the bottom corresponds to x-ray counts ranging from 0-50.

Pole Figure	**Main**	**Type-A**	**Type-B**	**Type-C**	**Type-D**	**Random**
(111)	98.27*	1.41*	0.18*	-	-	0.14*
Pole Figure	**Main**	**Type-A**	**Type-B**	**Type-C**	**Type-D**	**Random**
(220)	99.47	0.29	0.12	-	-	0.11
Pole Figure	**Main**	**Type-A**	**Type-B**	**Type-C**	**Type-D**	**Random**
(311)	99.71	0.08	0.13	-	-	0.08

Table 6.1: Texture analysis on the trial 4 (100) substrate from the (111), (220), and (311) pole figures in Figure 6.4. Values denoted with a * are skewed towards random orientations due to limits in the scanning angles reducing the intensity peak detection counts.

Pole Figure	**Main**	**Type-A**	**Type-B**	**Type-C**	**Type-D**	**Random**
(111)	96.05*	3.52*	0.22*	-	-	0.21*
Pole Figure	**Main**	**Type-A**	**Type-B**	**Type-C**	**Type-D**	**Random**
(220)	99.08	0.59	0.26	-	-	0.07
Pole Figure	**Main**	**Type-A**	**Type-B**	**Type-C**	**Type-D**	**Random**
(311)	99.39	0.15	0.38	-	-	0.08

Table 6.2: Texture analysis on the trial 4 (100)-4° substrate from the (111), (220), and (311) pole figures in Figure 6.4. Values denoted with a * are skewed towards random orientations due to limits in the scanning angles reducing the intensity peak detection counts.

Pole Figure	**Main**	**Type-A**	**Type-B**	**Type-C**	**Type-D**	**Random**
111	73.35*	11.32*	7.57*	3.25*	2.21*	2.32*
Pole Figure	**Main**	**Type-A**	**Type-B**	**Type-C**	**Type-D**	**Random**
220	99.22	0.39	0.19	0.13	-	0.07
Pole Figure	**Main**	**Type-A**	**Type-B**	**Type-C**	**Type-D**	**Random**
311	99.39	0.35	0.16	-	-	0.10

Table 6.3: Texture analysis on the trial 4 (111) substrate from the (111), (220), and (311) pole figures in Figure 6.4. Values denoted with a * are skewed towards random orientations due to limits in the scanning angles reducing the intensity peak detection counts.

6.3 Conclusion

The difference in film morphology from deposition with and without Sb clearly indicate that Sb has a significant role as a surfactant in GaP on Si heteroepitaxy. The (100) substrate showed two significant differences, SEM images and the texture analysis data. Trial 1 data showed fairly consistent nucleation of small crystallites under 1 micron in diameter, contrary to the trial 4 SEM images which had a much higher nucleation density and crystallite diameters a fraction of that in trial 1. This implies that the Sb acts as predicted on the (100) substrate, creating increased nucleation on the surface. Consequential of the limited nucleation under trial 1 conditions, the texture analysis of trial 4 showed significant twinning that was not apparent in trial 1. This is likely due to the minimal volume of the grown film relative to the Si bulk, meaning the intensity peaks corresponding to twins simply appear too weak to be detected.

The (100)-4° substrate has less significant differences between trial 1 and 4 SEM images. The trial 1 SEM results showed a polycrystalline film covering nearly the entire surface, with grain diameters on the scale of 100 nm. Similarly, the trial 4 data also showed small grains with similar diameters. However, the lack of higher resolution scans make more rigorous comparisons challenging. Both conditions also showed the sparse nucleation of nanowires along the surface, localized more in the trial 4 sample (whereas the trial 1 conditions seemed to yield nanowires throughout the substrate). Interestingly, there is very strong agreement between the trial 1 and 4 texture analyses. Both showed very similar ratios between type-A and type-B twins: trial 1 has A/B ratios of 16, 2.3, and 0.36 in contrast to trial 4 with 15, 2.3, and 0.39 for pole figures (111), (220), and (311), respectively. These

results validate the conclusions drawn from the SEM images; there is little to no effect from Sb deposition pre-growth on the (100)-4° substrate. The difference between the (100) and (100)-4° pre-treatment effects likely have to do with the fact that (100) substrates have significantly less step edges than that of the offcut substrate, meaning there are fewer potential nucleation sites. This would explain why the (100) substrate had a significant difference in surface morphology between trials 1 and 4, but little to no difference for the (100)-4° sample.

The (111) substrate has very significant variations in SEM images between trials 1 and 4. Trial 1 showed nanowires covering the entire surface, with polycrystalline strips along the surface that branch out in a tree-like fractal pattern and more sparsely nucleating crystallites in other areas, as seen in Figure 5.8. In contrast, the trial 4 images showed a far more consistent surface, with a polycrystalline film forming with relatively consistent nucleation throughout. Although the grains forming along the surface are roughly the same diameter as those of the trial 1 conditions, there are far fewer nanowires being formed on this surface. The texture analysis of the (111) substrate is interesting as it shows the presence of 4 different types of twins, albeit that two are significantly weaker and are not detected in all scans due to the limited intensity being masked by that of the random orientation (texture components under 50% of the random intensity are neglected in the texture analysis). Based on the SEM results, it is clear that Sb has a two-fold effect on the (111) orientation: Sb prevents the formation of GaP nanowires, and Sb prevents the clustering of GaP into regions of two different nucleation densities (of the tree-like strips and sparsely distributed grains) to a densely-packed surface.

Chapter 7

Conclusions

7.1 Summary

The MOCVD heteroepitaxy of GaP/Si remains an elusive problem that has not received adequate exploration. Nonetheless, the significant applications to high quality III-V/Si heterostructures and commercial relevance to MOCVD makes this an avenue worth exploration. Working towards the development of MOCVD-grown OP-GaP templates for LWIR DFG, investigations into various pre-treatment, growth, and surfactant conditions were conducted. The precursors used in the experiments below were TMGa, PH_3, and TMSb, with a low temperature of 550 °C and a high temperature of 750 °C. GaP/GaP homoepitaxy is established to ensure smooth surfaces (and burying surface contaminants) for future Si deposition on GaP. Below summarizes the results of the GaP/GaP homoepitaxy trials:

- GaP (100)-4°: The sample underwent a high temperature pre-treatment and growth, with a RMS roughness of 0.46 nm. The surface does not have clearly defined step-edges, but has a smooth surface.

- GaP (111)A: The sample underwent a high temperature pre-treatment and growth, with a RMS roughness of 0.56 nm. This surface does have clear step edges forming, with a height of approximately 2 monolayers.

Choice of pre-treatment conditions shows significant effects to the Si surface structure. Below summarizes the results of the Si pre-treatment trials:

- Si (100): The sample underwent both low and high temperature pre-treatment, with a RMS roughness of 0.47 nm and 0.06 nm, respectively.
- Si (100)-4°: The sample underwent both low and high temperature pre-treatment, with a RMS roughness of 0.27 nm and 0.10 nm, respectively.
- Si (111): The sample underwent both low and high temperature pre-treatment, with a RMS roughness of 0.26 nm and 0.07 nm, respectively.
- The low temperature pre-treated Si surfaces had larger variations in the surface height, as apparent from the RMS roughness values. The surface structure seems to be mainly dominated by the pre-treatment temperature, not the substrate orientation.

As stated previously, three different temperature combinations were used: T1) low temperature pre-treatment and growth, T2) high temperature pre-treatment low temperature growth, and T3) high temperature pre-treatment and growth. Choice of growth conditions and orientation also show significant effects to the nucleation of GaP on Si:

- Si (100): T1 yielded highly faceted crystallites in the 100s of nm-micron scale,

with similar sized crystallites (but much less densely nucleated) in T2. The T2 conditions also yielded large quantities of nanowires, with many wires faceting out from the same nucleation sites. T3 yielded large crystallites of approximately 5 microns in diameter and seemed to cluster together in regions of high and low density. No twins were detected, albeit this may be due to the volume of deposited GaP.

- Si (100)-4°: T1 yielded a polycrystalline film with grain sizes of approximately 100 nm, with few but some nanowires nucleating. T2 was not uniform after deposition, with 2 regions: one that looked macroscopically smooth and one with a dull yellow appearance. The smooth region yielded crystallites of non-uniform size (micron-scale), while the yellow region was covered in densely-packed nanowires. T3 yielded crystallites of approximately 5 microns in diameter, with more consistent, evenly-spread nucleation sites compared to that of (100) T3. Minimal twinning was found with T2 conditions, and the most twinning was found in T3.

- Si (111): T1 yielded a combination of fractal-like polycrystalline films, crystallites with diameters of 100s of nm, and nanowires. T2 yielded crystallites of approximately 1 micron, and few but some nanowires nucleating. T3 had a surface with crystallites of approximately 10 microns, which cluster into long chains that form polycrystalline films. Minimal twinning was found in T2. The most twinning was found in T1, with T2 having the least and T3 having no detectable twins but a high random component.

The effectiveness of Sb as a surfactant in GaP/Si heteroepitaxy was explored

using the low temperature pre-treatment and growth conditions. The experiment used the same conditions as the previously discussed low temperature GaP/Si growth, but with the exception of a 5 second TMSb deposition step between pre-treatment and growth (T4). The use of Sb as a surfactant has significant effects:

- Si (100): The sample had dense crystallite clusters with nanowires present along the surface. Nucleation site density significantly increased when grown with Sb, and the crystallite diameter was significantly smaller. The (100) texture analysis showed twinning that was not visible in the non-Sb texture analysis.
- Si (100)-4°: The specimen seemed comparable to that without Sb. The comparability between the texture analysis of T1 and 4 support this result.
- Si (111): The sample differed far from that of T1, which was covered in nanowires, crystallites, and polycrystalline films. T4 yielded a very consistent polycrystalline film of crystallites - similar to that of T1 - but not a patterned film like that in T1. Very few nanowires were present on the surface of the specimen; the formation was greatly suppressed.

7.2 Future work

The work presented in this thesis provides meaningful insight for potential future work. More experiments are planned to be conducted, but so far have been unfortunately impossible due to instrument maintenance, staff overturn and limitations from the COVID-19 pandemic. Listed below are some of the future investigations:

- Si/GaP heteroepitaxy: Due to a shortage of the silane precursor (SiH_4), experiments into depositing thin films of Si were not able to be conducted. The deposition of Si on GaP surfaces is a fundamental step to achieving OP-GaP templates, one that has not undergone sufficient investigation. Conditions for the deposition of Si on GaP - while achieving the ideal Si double step formation on Si (100) - is necessary to accomplish the goal of OP-GaP templates by MOCVD.

- GaP homoepitaxy: Although smooth GaP has been previously reported elsewhere and accomplished within this thesis, comparatively few TMGa/PH_3 experiments have been conducted relative to TEGa/TBP. A more systematic experiment into the difference between temperature, V/III ratio, and flow rate, and how they effect growth rate and surface roughness would be a meaningful contribution to literature.

- GaP/Si heteroepitaxy: A potential improvement to the experiments shown here would be the growth of a Si buffer layer on Si substrates prior to growth. This would allow the burying of potential surface contaminants that were not removed from the HF etch or subsequently formed. This has not been well studied previously.

- GaP with Sb as a surfactant: Sb has been explored as a surfactant for the growth of various III-V heterostructures, but this is the first use for GaP/Si heteroepitaxy. The conditions explored for Sb as a surfactant were very limited; only the predeposition of Sb and one temperature was used. Future experiments exploring the predeposition of Sb in various quantities (to achieve

maximal surface coverage), the deposition (and potential incorporation) of Sb during GaP growth, and various pre-treatment and growth temperature conditions would be a valuable contribution to the existing body of knowledge.

Appendix A

θ-2θ X-ray diffraction supplement

This section is supplemental to the pole figures shown in this thesis. Although 2-dimensional x-ray scans have been presented, the corresponding 1-dimensional θ-2θ plots are shown included here.

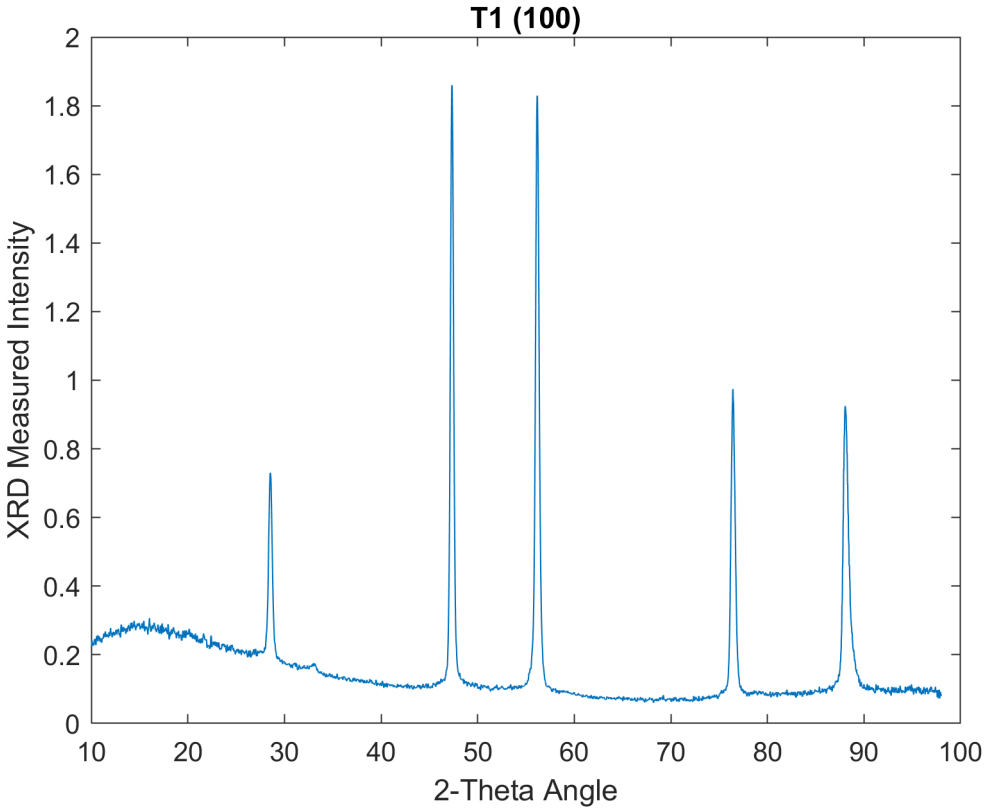

Figure A1.1: One-dimensional XRD of trial 1 on Si (100) (GaP grown on Si).

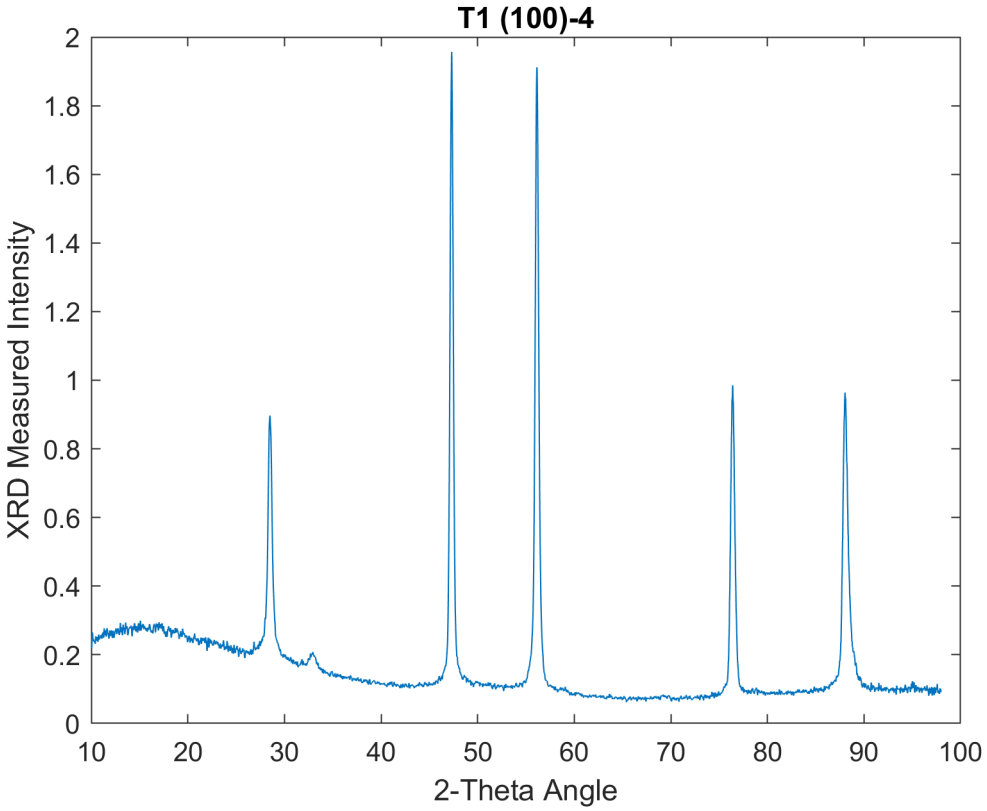

Figure A1.2: One-dimensional XRD of trial 1 on Si (100)-4° (GaP grown on Si).

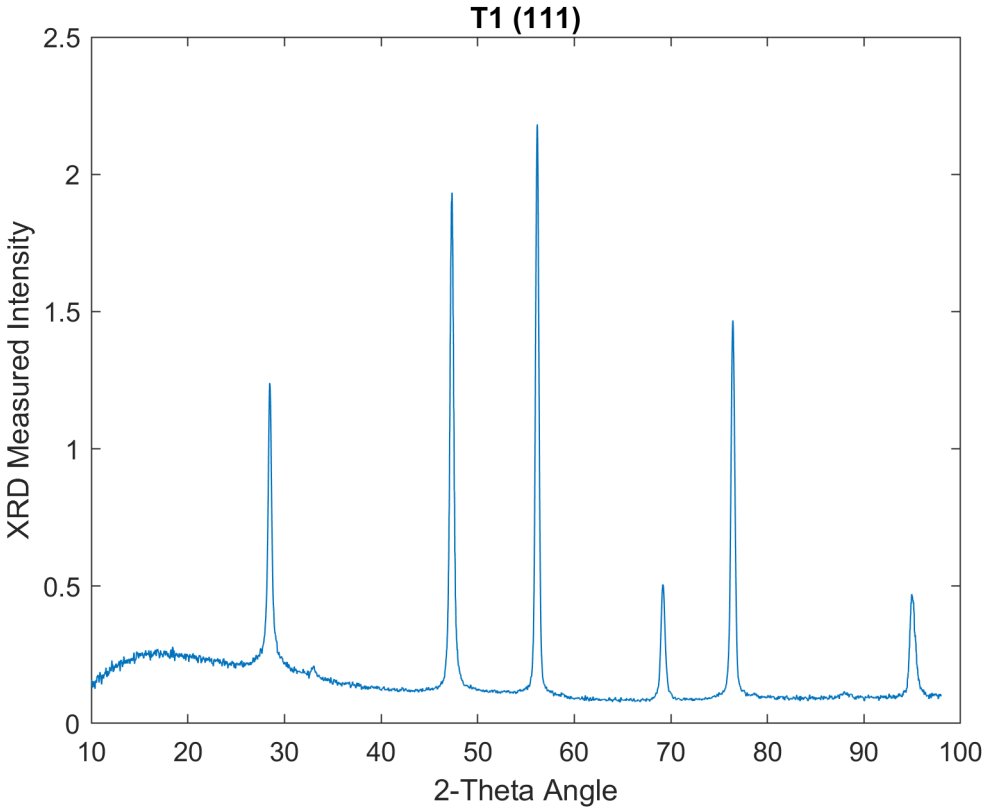

Figure A1.3: One-dimensional XRD of trial 1 on Si (111) (GaP grown on Si).

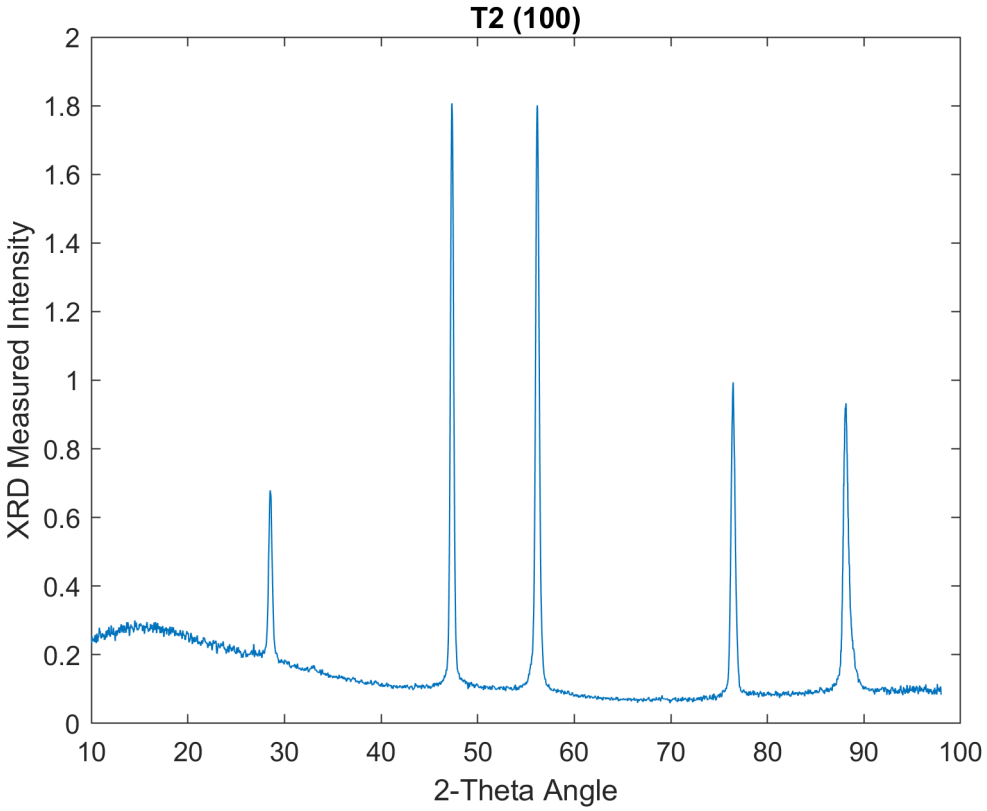

Figure A1.4: One-dimensional XRD of trial 2 on Si (100) (GaP grown on Si).

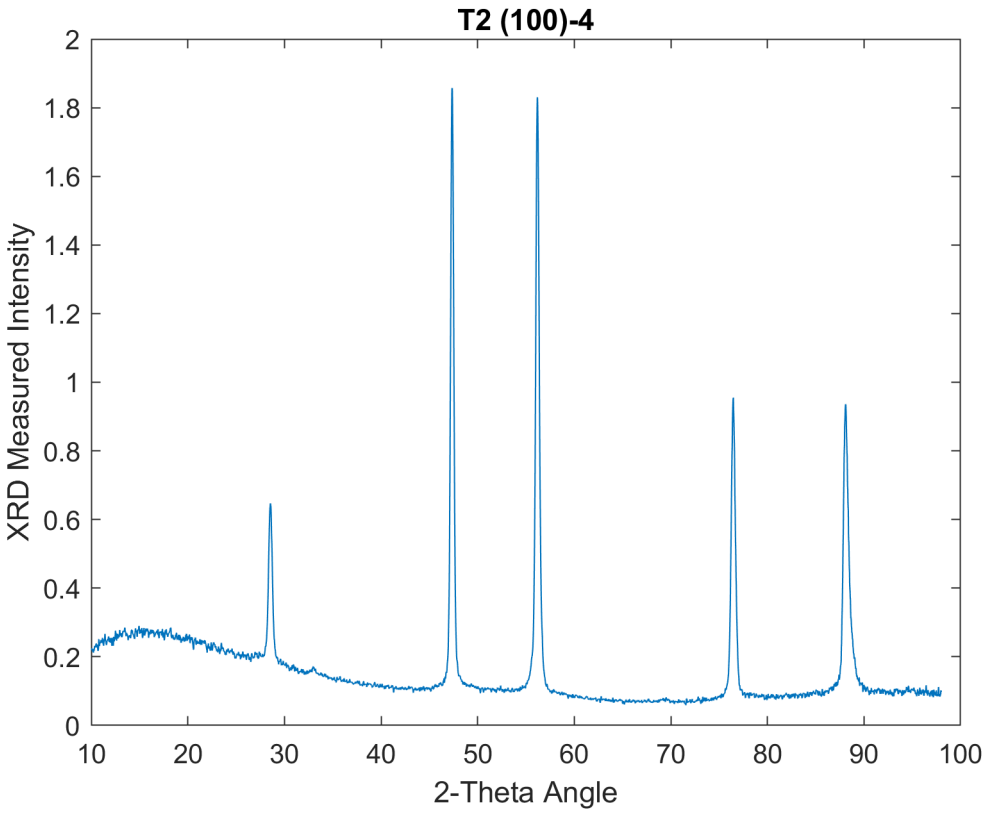

Figure A1.5: One-dimensional XRD of trial 2 on Si (100)-4°. This sample was not uniform, this is a scan of the non-"yellow" region that appears to not have nanowires (GaP grown on Si).

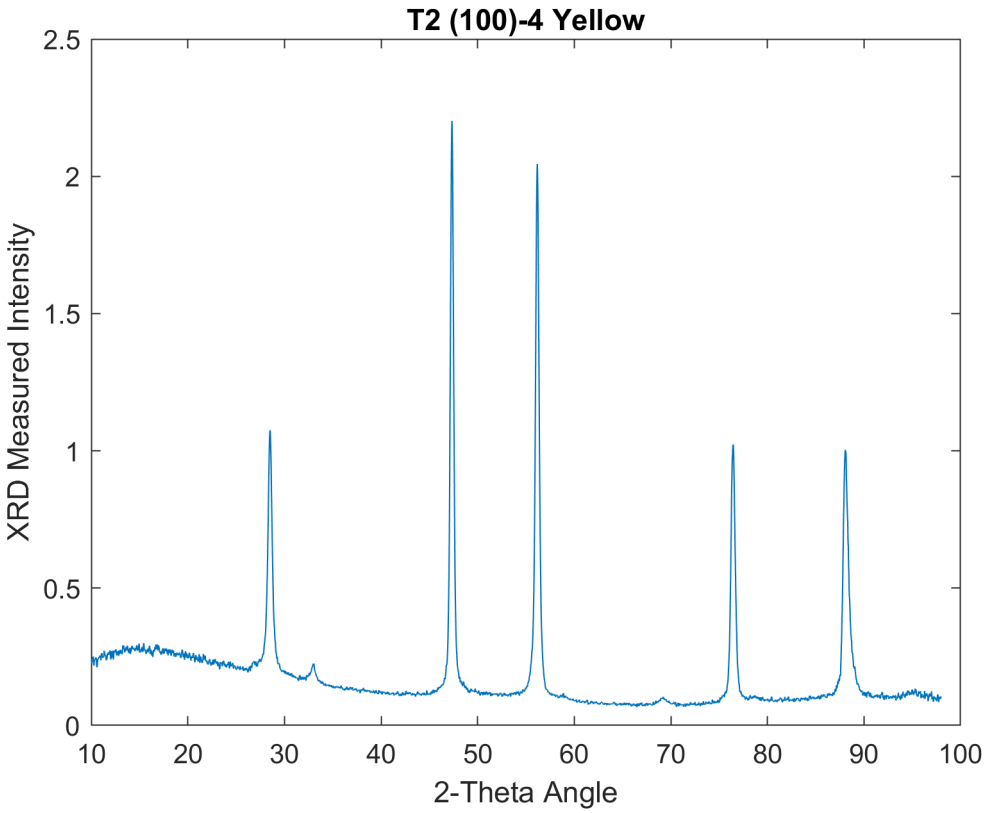

Figure A1.6: 1-Dimensional XRD of trial 2 on Si (100)-4°. This sample was not uniform, this is a scan of the "yellow" region that appears to have nanowires (GaP grown on Si).

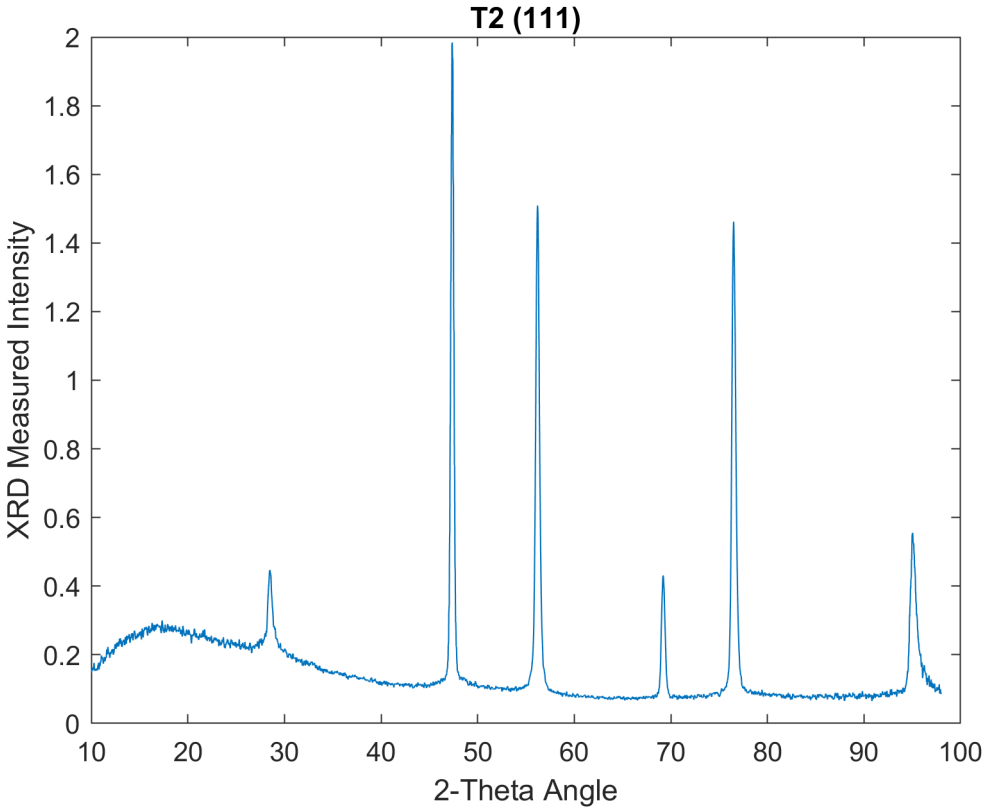

Figure A1.7: One-dimensional XRD of trial 2 on Si (111) (GaP grown on Si).

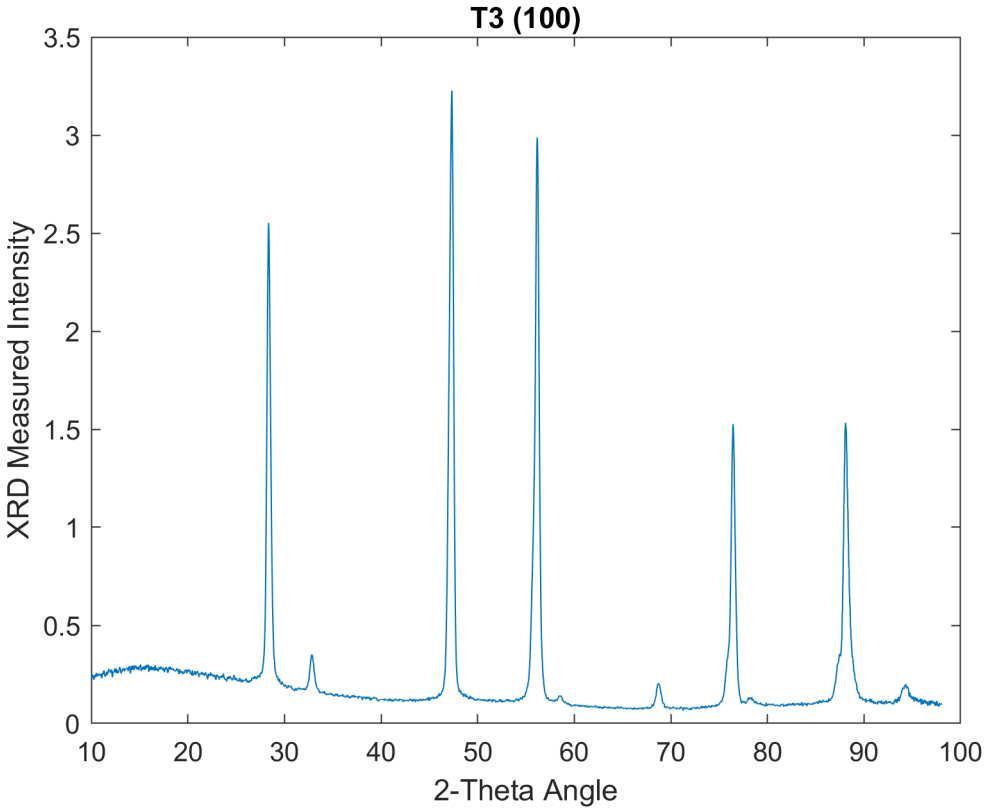

Figure A1.8: One-dimensional XRD of trial 3 on Si (100) (GaP grown on Si).

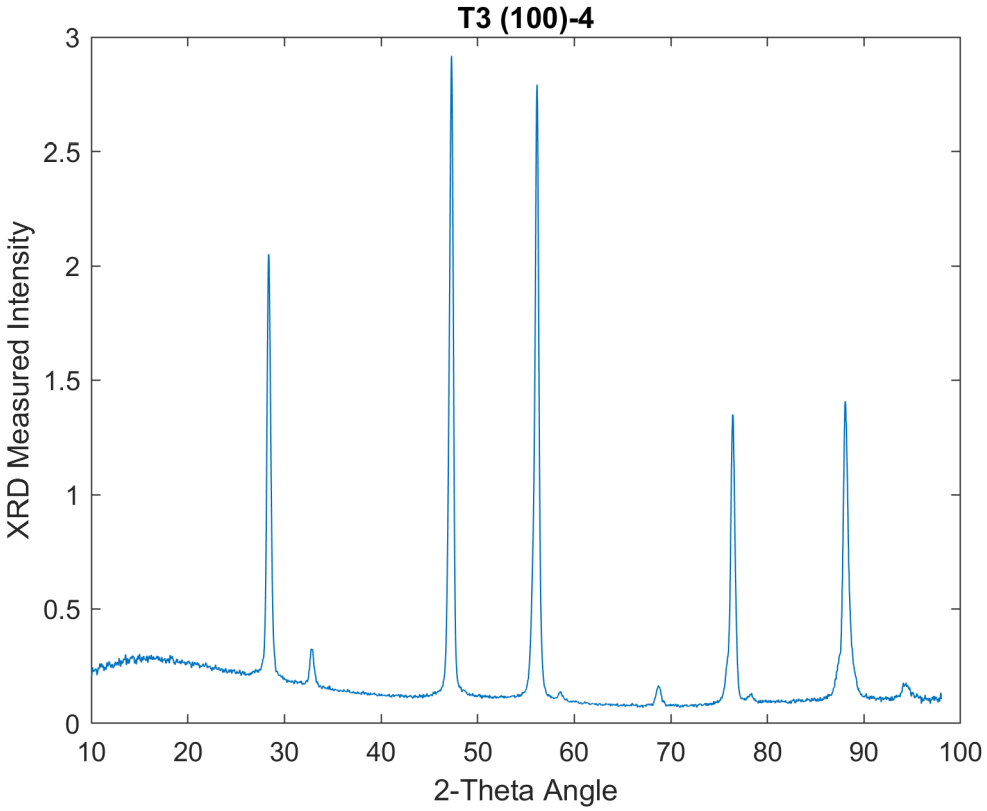

Figure A1.9: One-dimensional XRD of trial 3 on Si (100)-4° (GaP grown on Si).

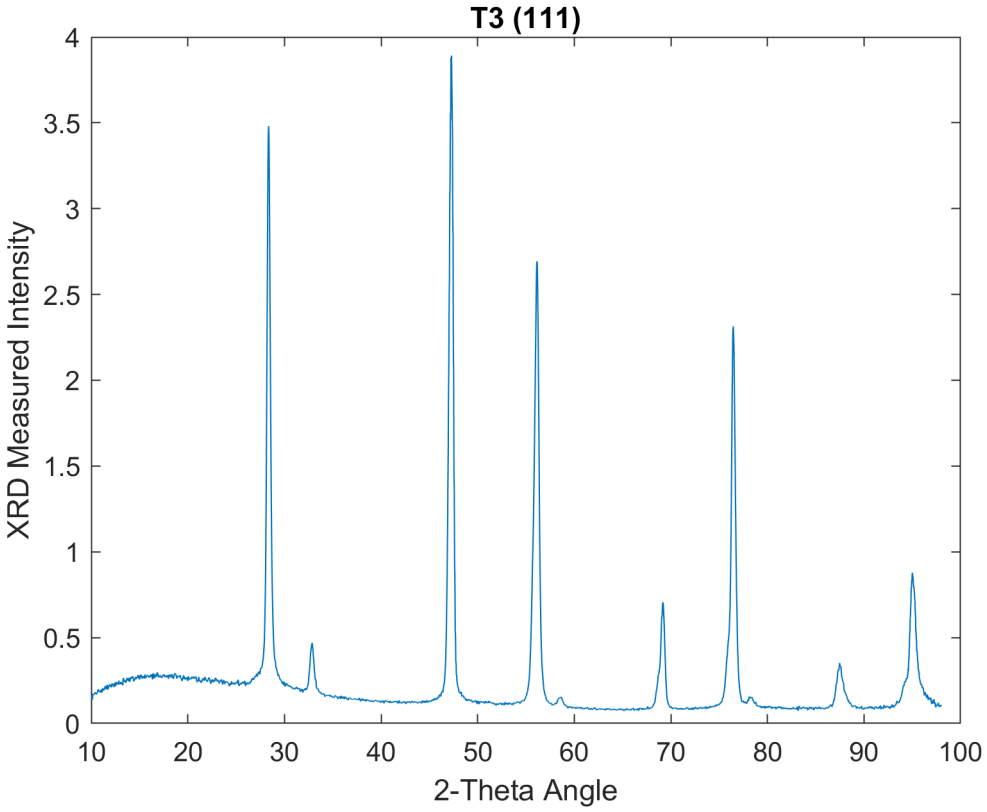

Figure A1.10: One-dimensional XRD of trial 3 on Si (111) (GaP grown on Si).

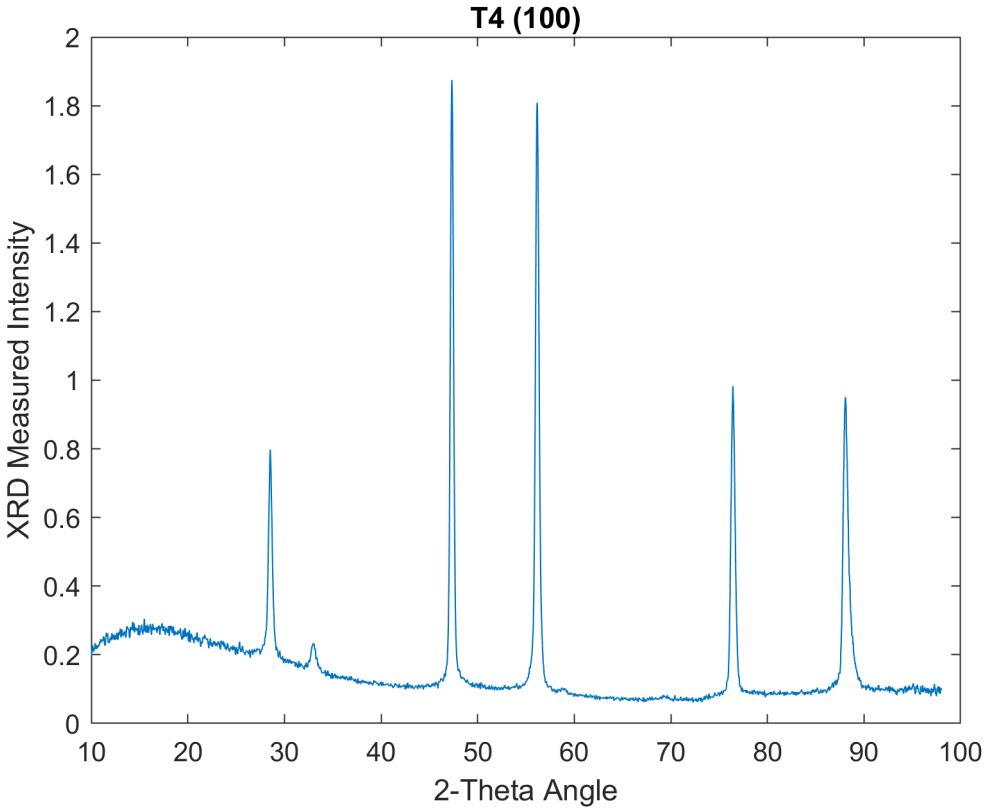

Figure A1.11: One-dimensional XRD of trial 4 on Si (100) (GaP grown on Si).

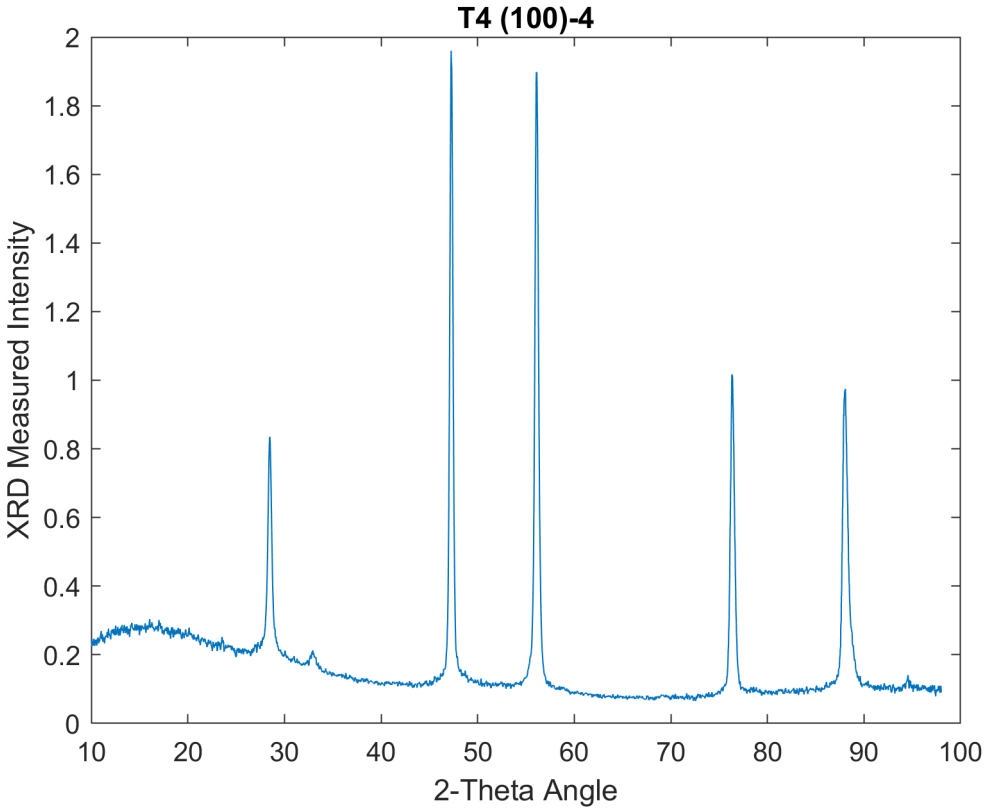

Figure A1.12: One-dimensional XRD of trial 4 on Si (100)-4° (GaP grown on Si).

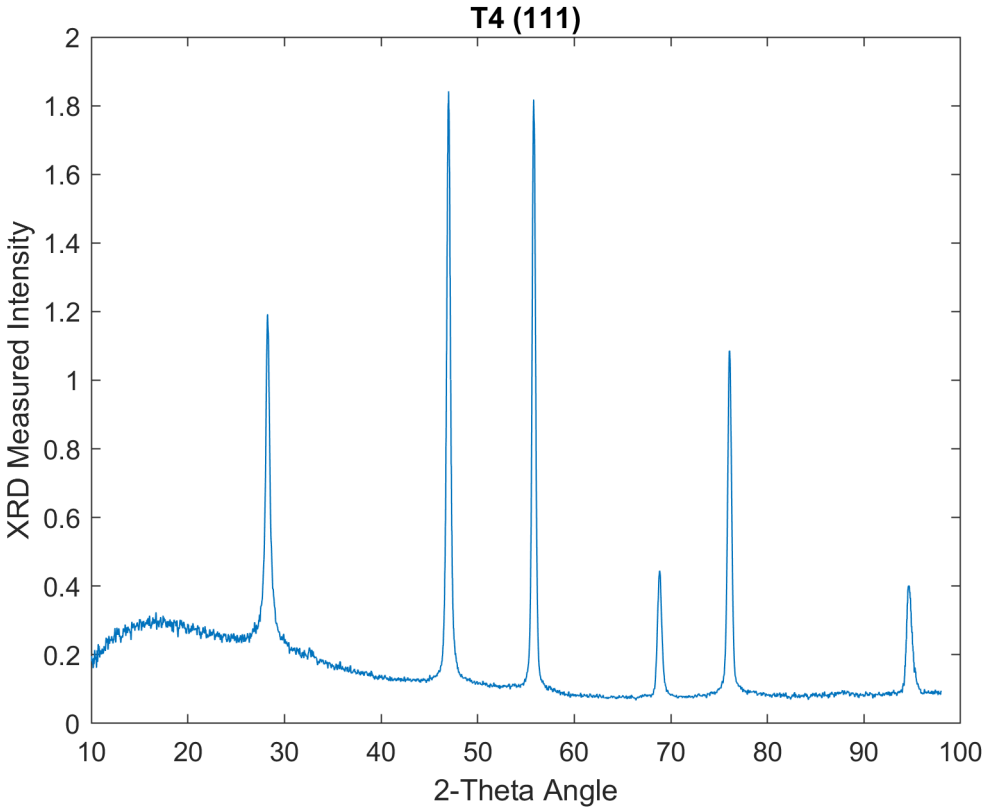

Figure A1.13: One-dimensional XRD of trial 4 on Si (111) (GaP grown on Si).

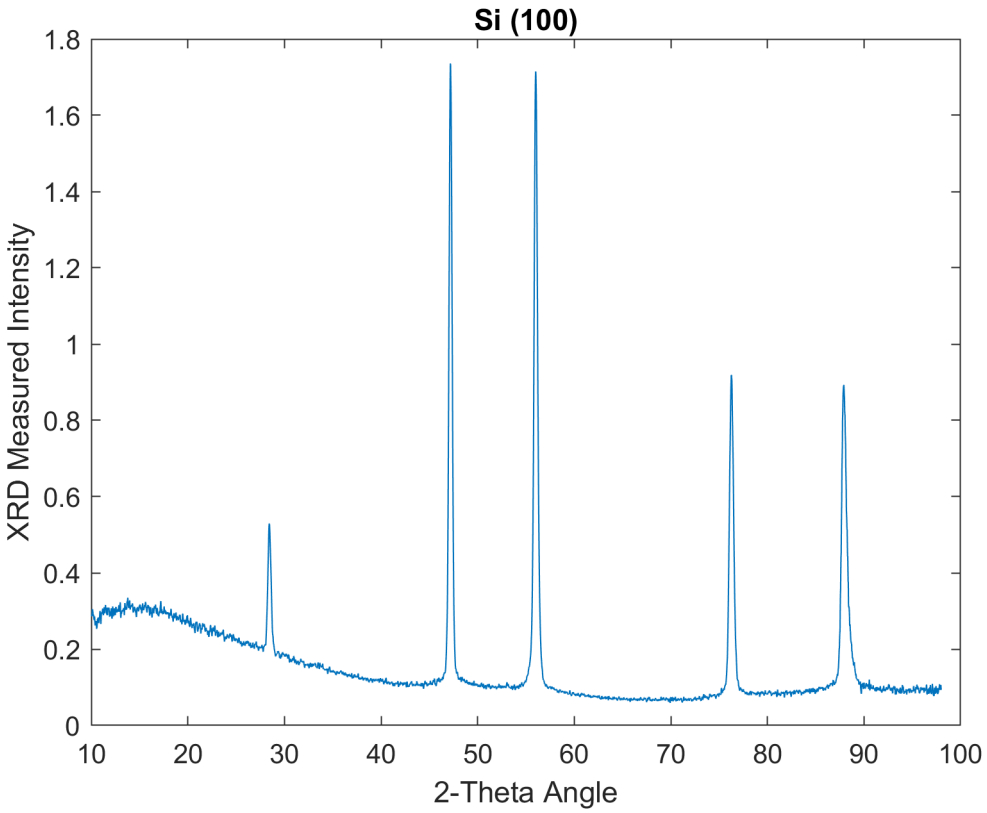

Figure A1.14: One-dimensional XRD of pre-treated Si (100).

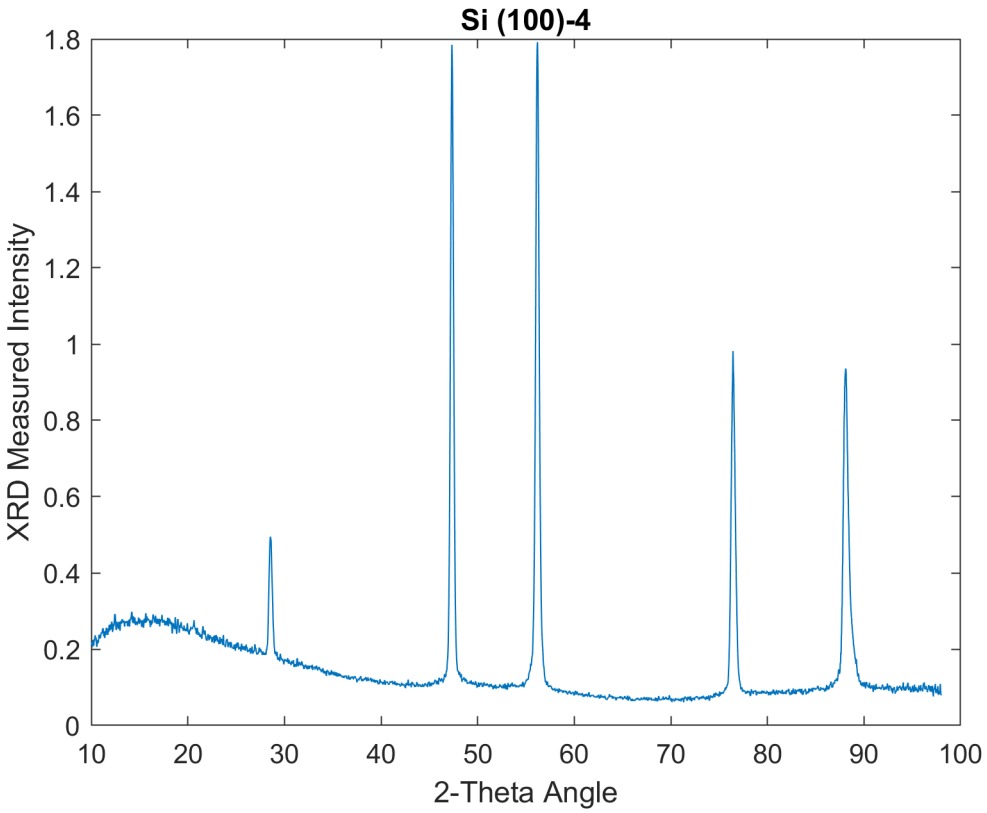

Figure A1.15: One-dimensional XRD of pre-treated Si (100)-4°.

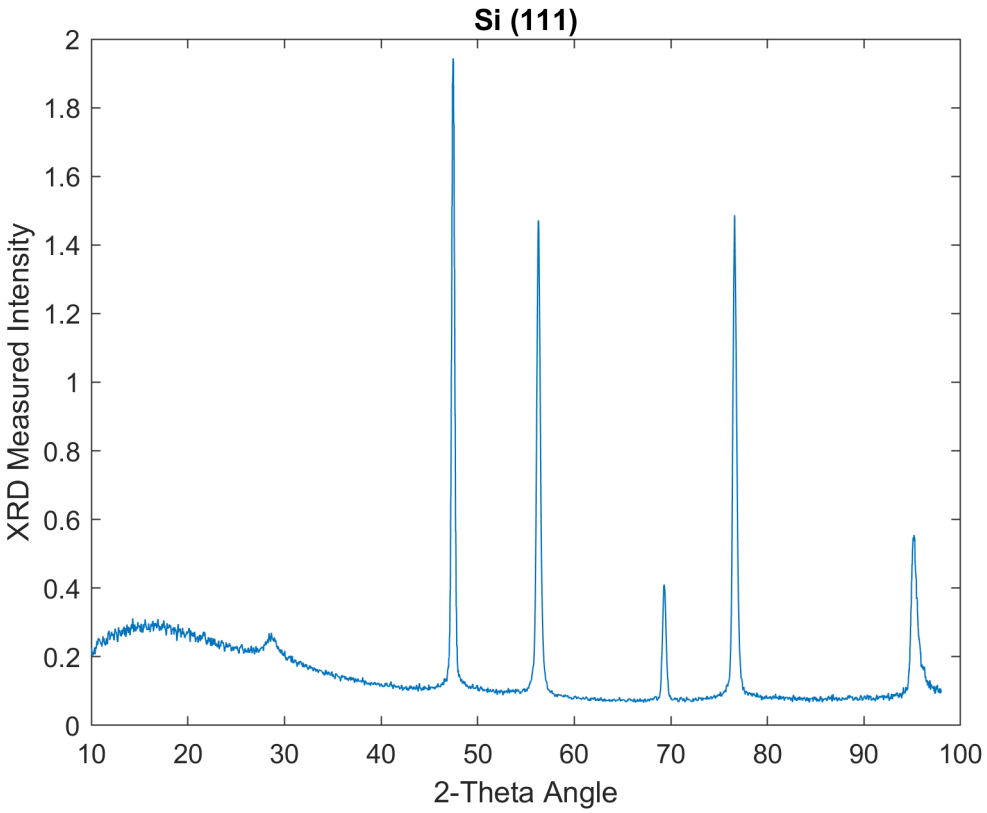

Figure A1.16: One-dimensional XRD of pre-treated Si (111).

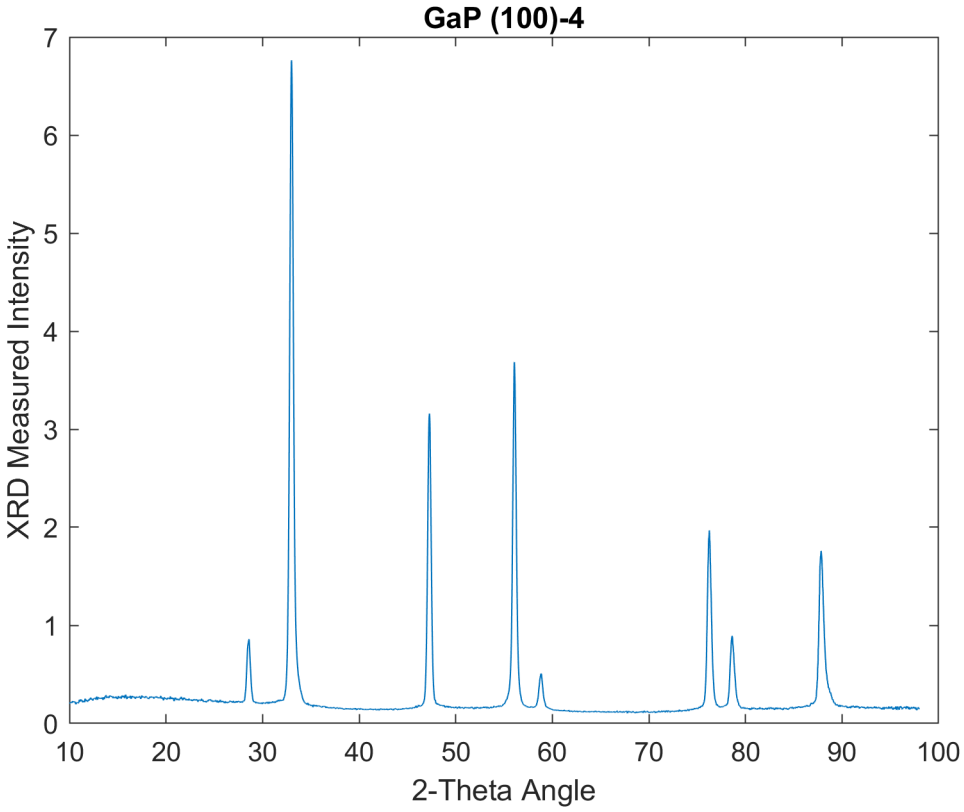

Figure A1.17: One-dimensional XRD of homoepitaxial GaP (100)-4°.

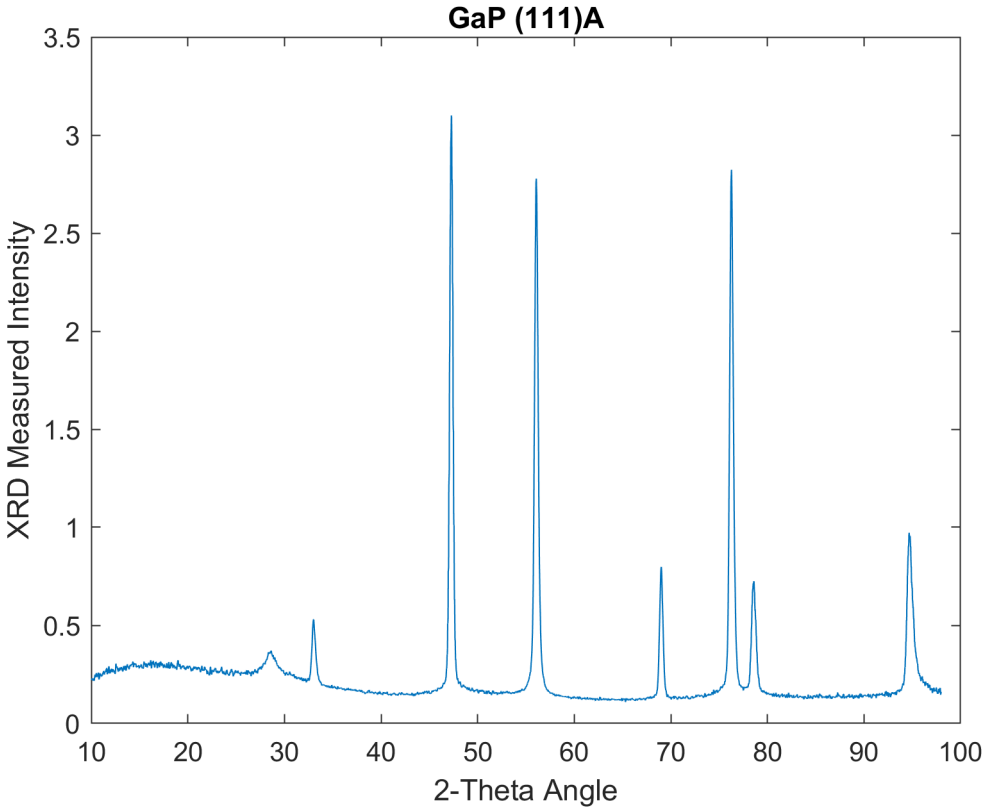

Figure A1.18: One-dimensional XRD of homoepitaxial GaP (111)A.

Appendix B

Flow rate per trial

Trial	**TMGa Rate (sccm/min)**	**PH3 Rate (sccm/min)**	**TMSb Rate (sccm/min)**
T1 (10 min growth)	80	120	0
T2 (10 min growth)	50	80	0
T3 (10 min growth)	80	85	0
T4 (10 min growth)	80	100	40
Homoepitaxy (5 min growth)	85	250	0

Table A2.1: Flow rates for various experiments.

Appendix C

Twin intensity projections

This section includes all the various stereo projections of the twins found during the examination of grown films. For each family of twins one individual orientation is shown, however, due to crystal symmetry there are several equivalent orientations that were included during texture analysis calculations. The stereo projections are done using the WinWulff [47] with the pole figures being generating using the GADDS software [**g**]

A1 (111) pole figures

A1.1 (100) and (100)-4° substrates

As the (100) and (100)-4° substrates are very similar, the pole figures of the two are very similar, with the offcut substrate being 4° tilted in the stereo projection. The white circles highlight visible intensity peaks in the example pole figure.

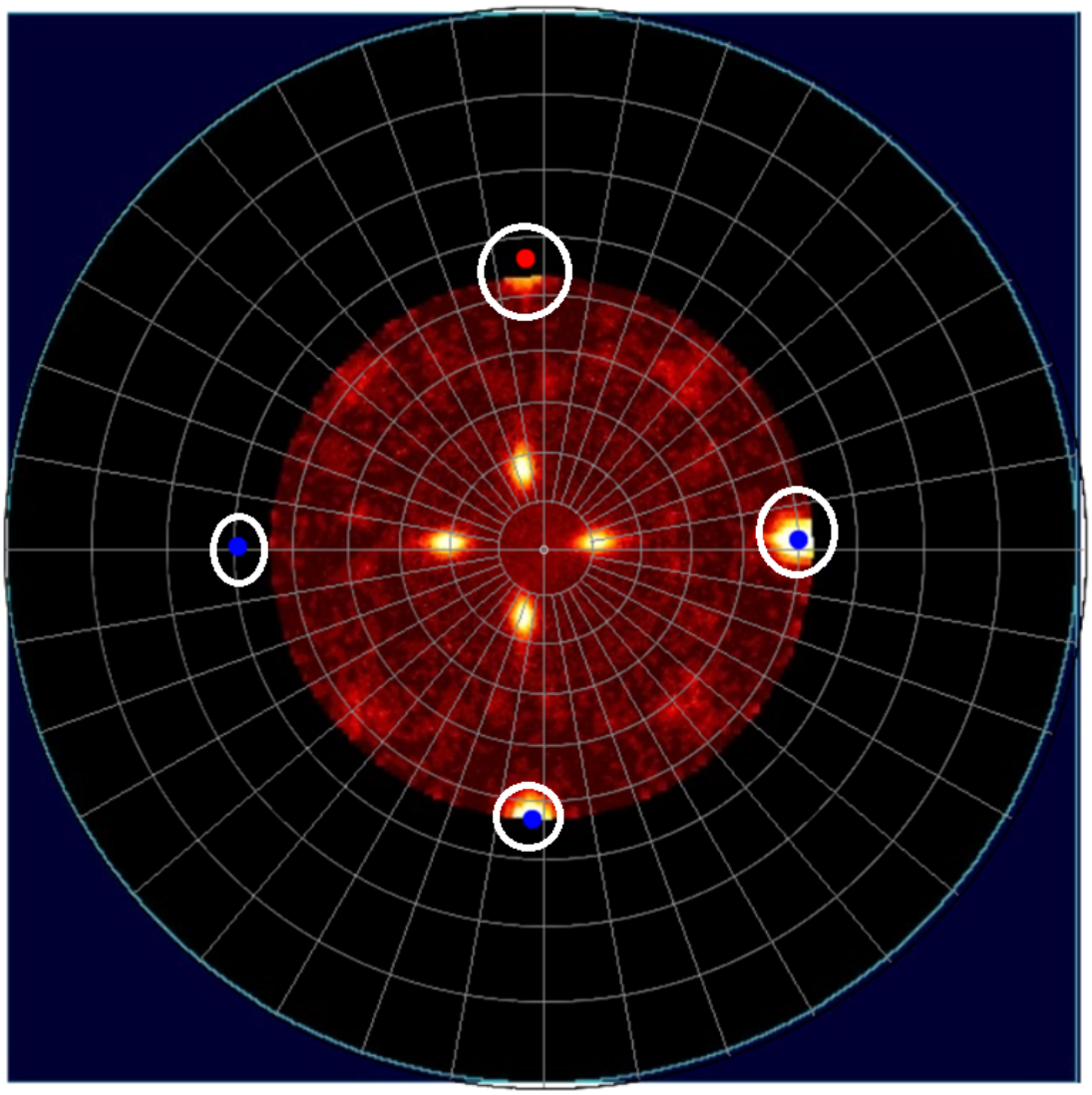

Figure A3.1: Intensity peaks for the (111) family of planes corresponding to the main (100) orientation; (100) and (100)-4° substrates.

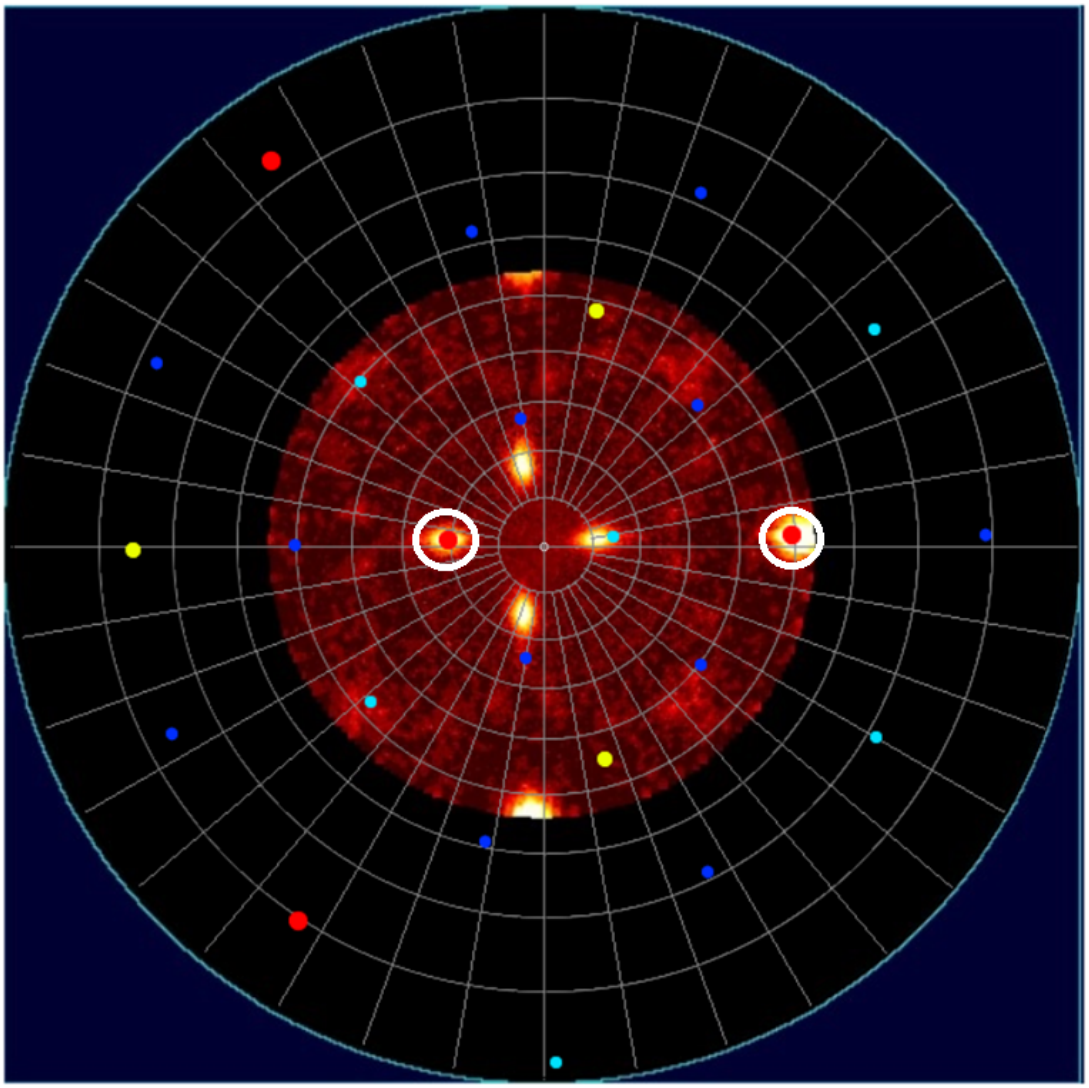

Figure A3.2: Intensity peaks for the (111) family of planes corresponding to type-A twins; (100) and (100)-4° substrates.

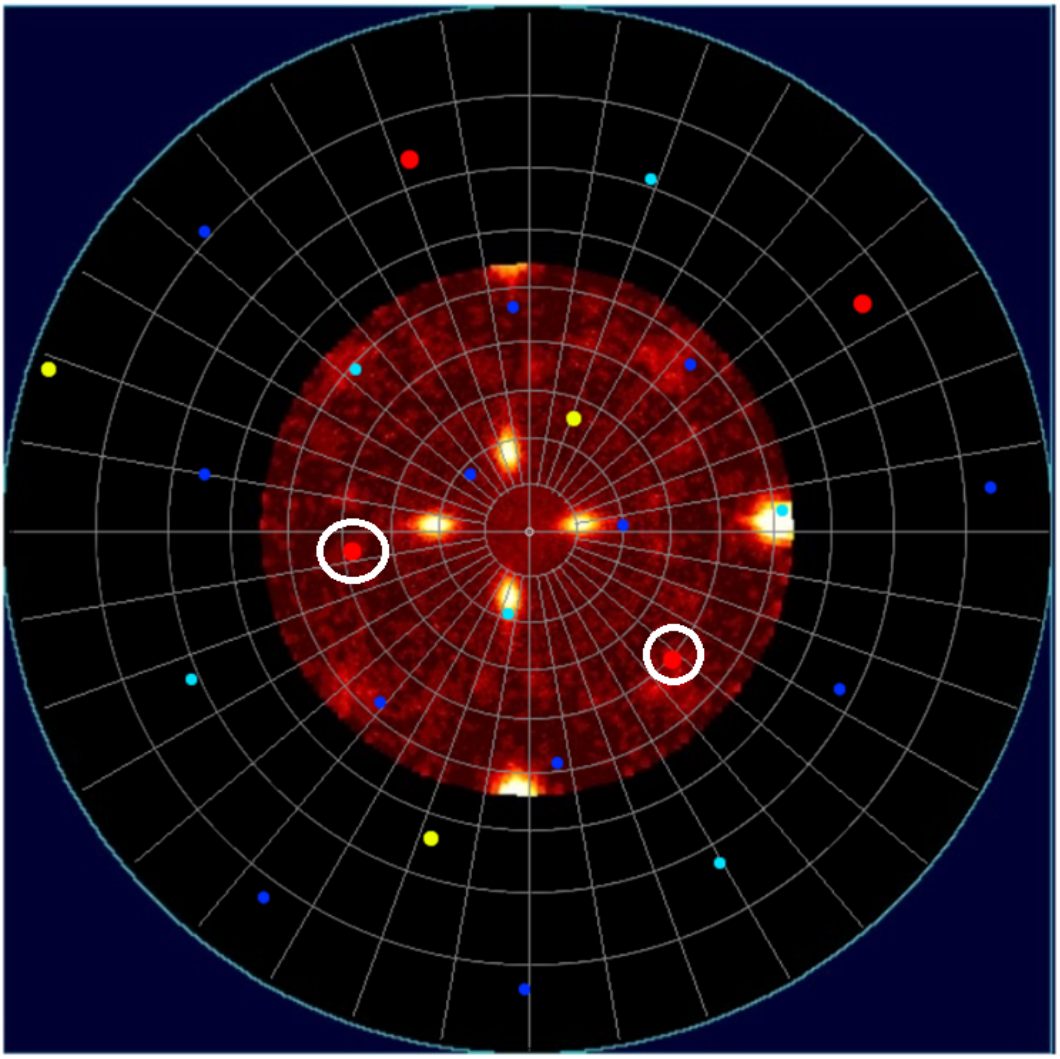

Figure A3.3: Intensity peaks for the (111) family of planes corresponding to type-B twins; (100) and (100)-4° substrates.

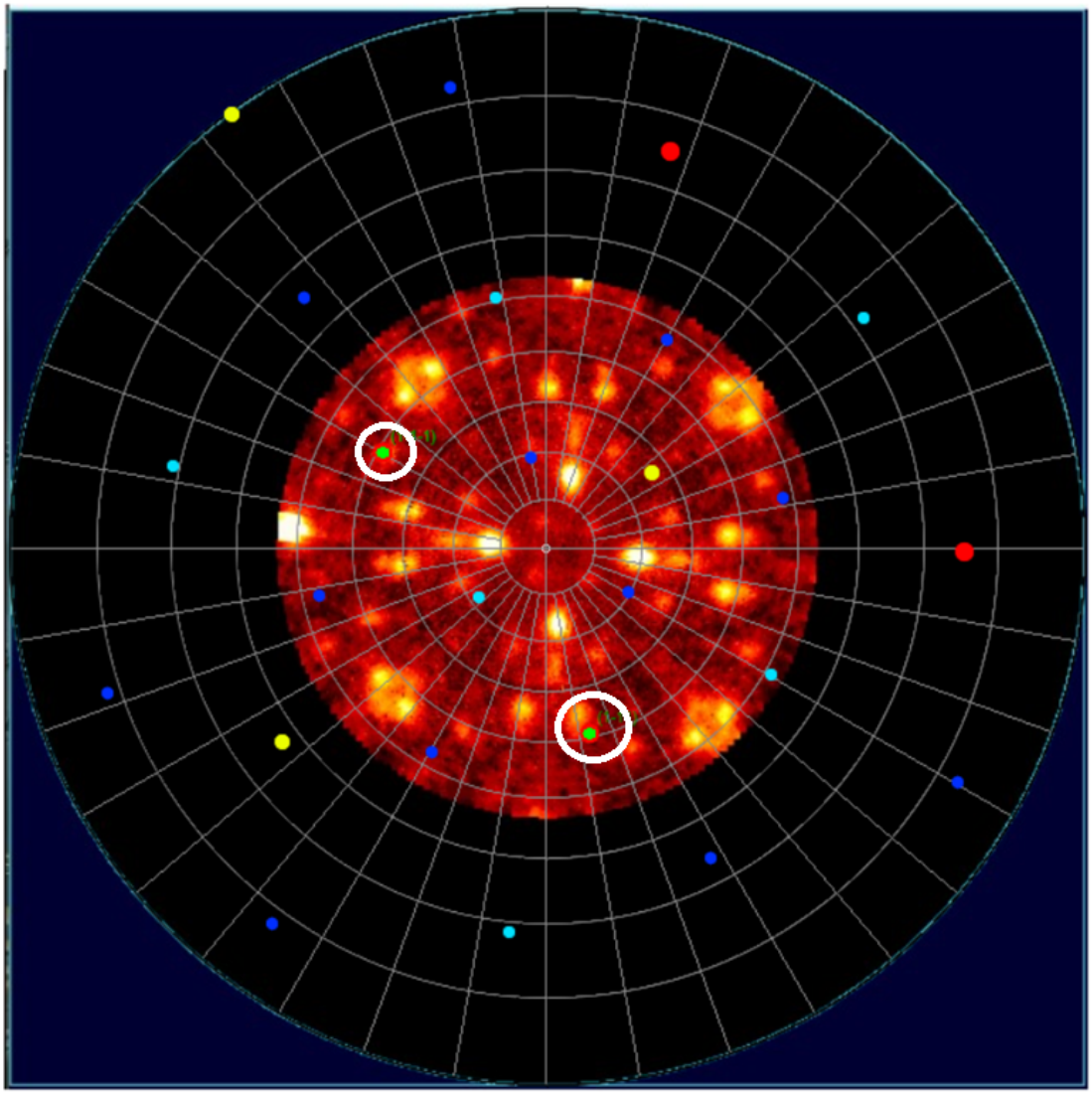

Figure A3.4: Intensity peaks for the (111) family of planes corresponding to type-C twins; (100) and (100)-4° substrates.

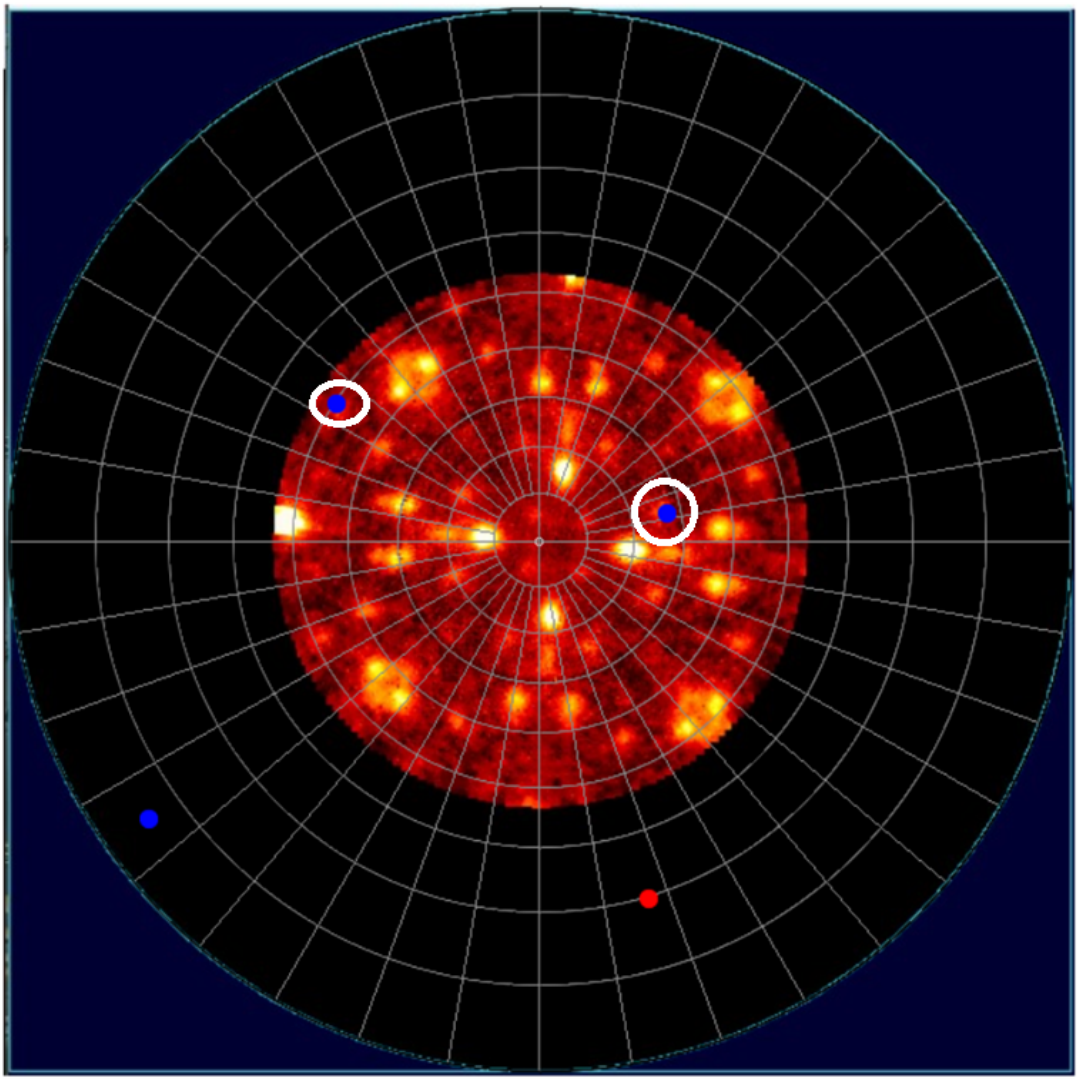

Figure A3.5: Intensity peaks for the (111) family of planes corresponding to type-D twins; (100) and (100)-4° substrates.

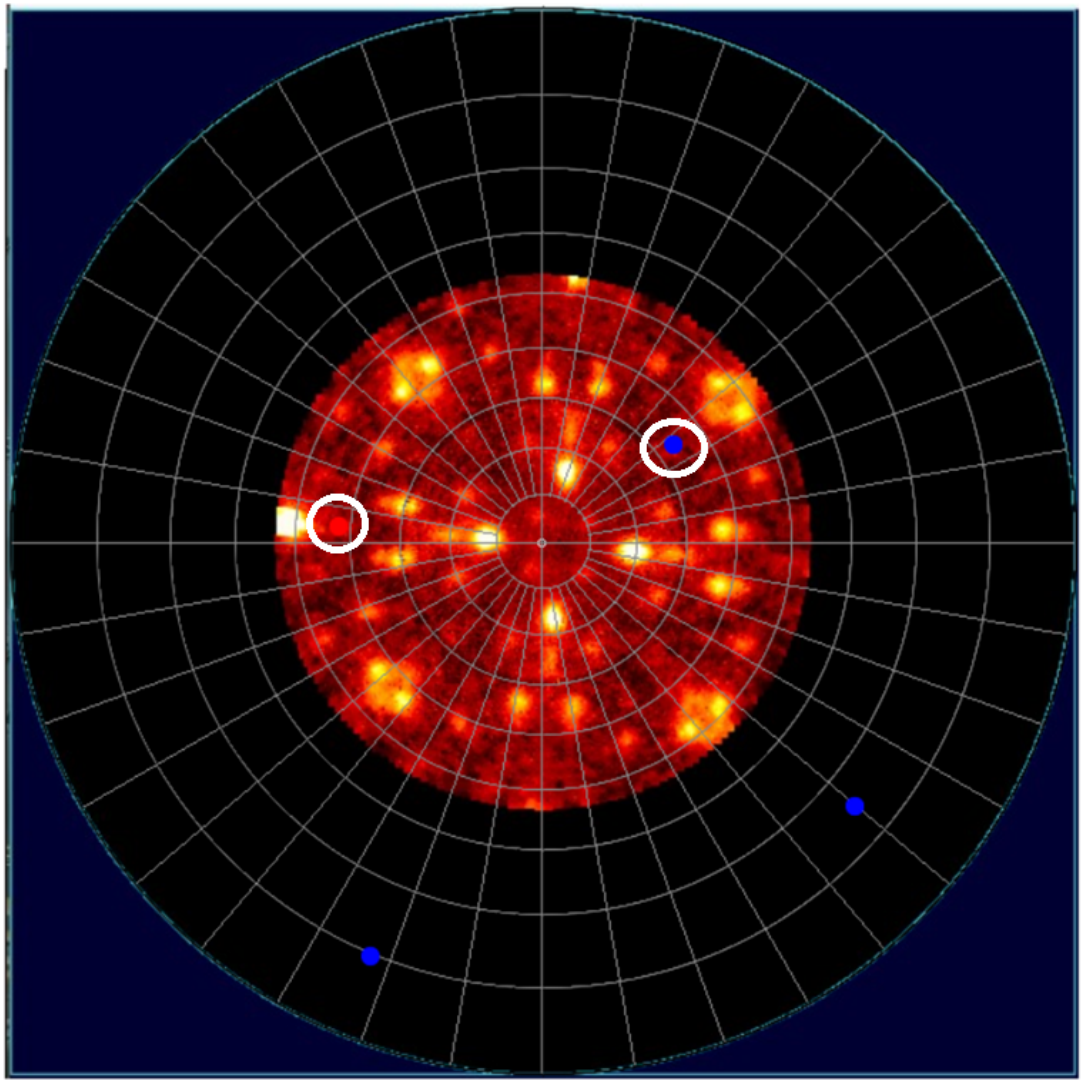

Figure A3.6: Intensity peaks for the (111) family of planes corresponding to type-E twins; (100) and (100)-4° substrates.

A1.2 (111) substrates

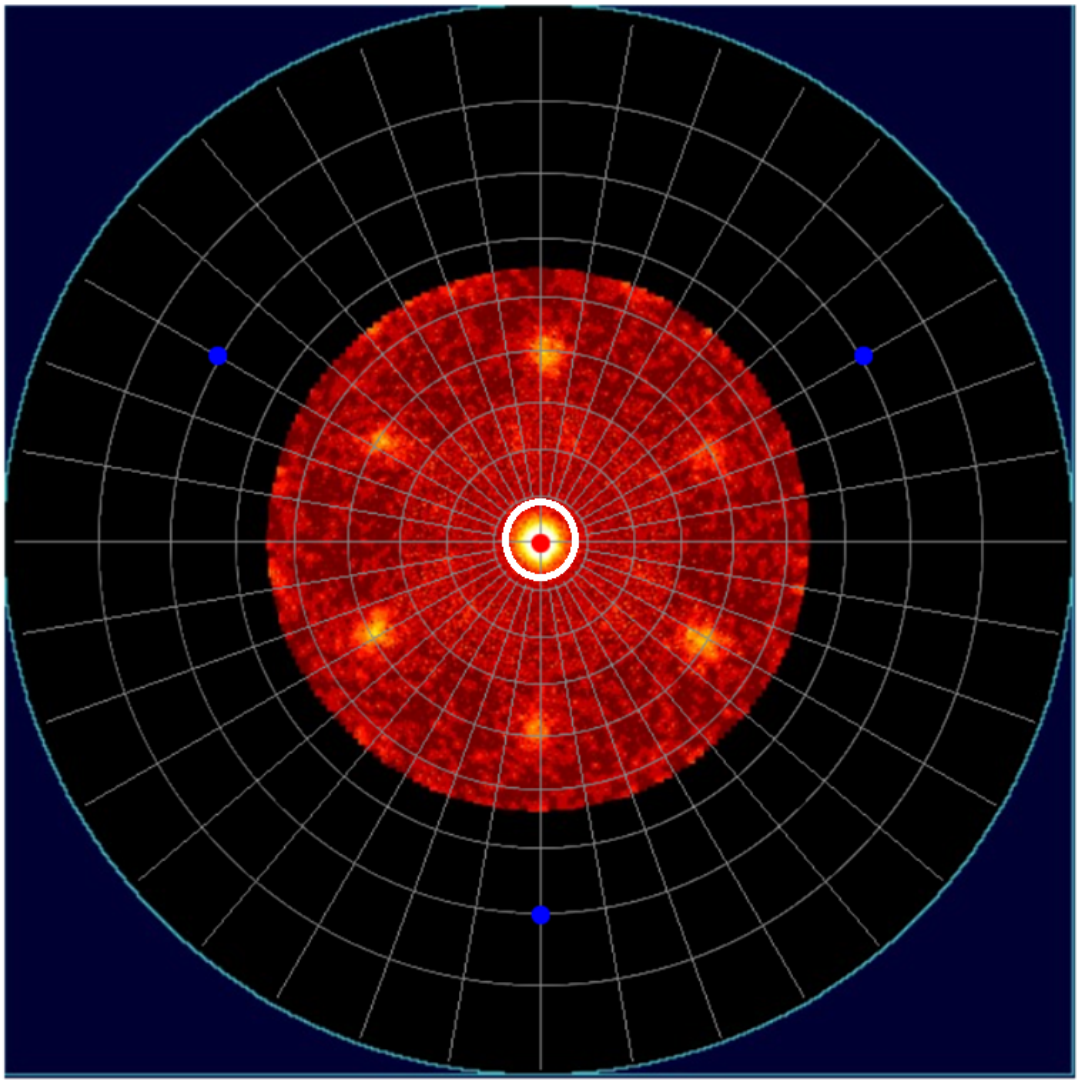

Figure A3.7: Intensity peaks for the (111) family of planes corresponding to the main (111) orientation; (111) substrates.

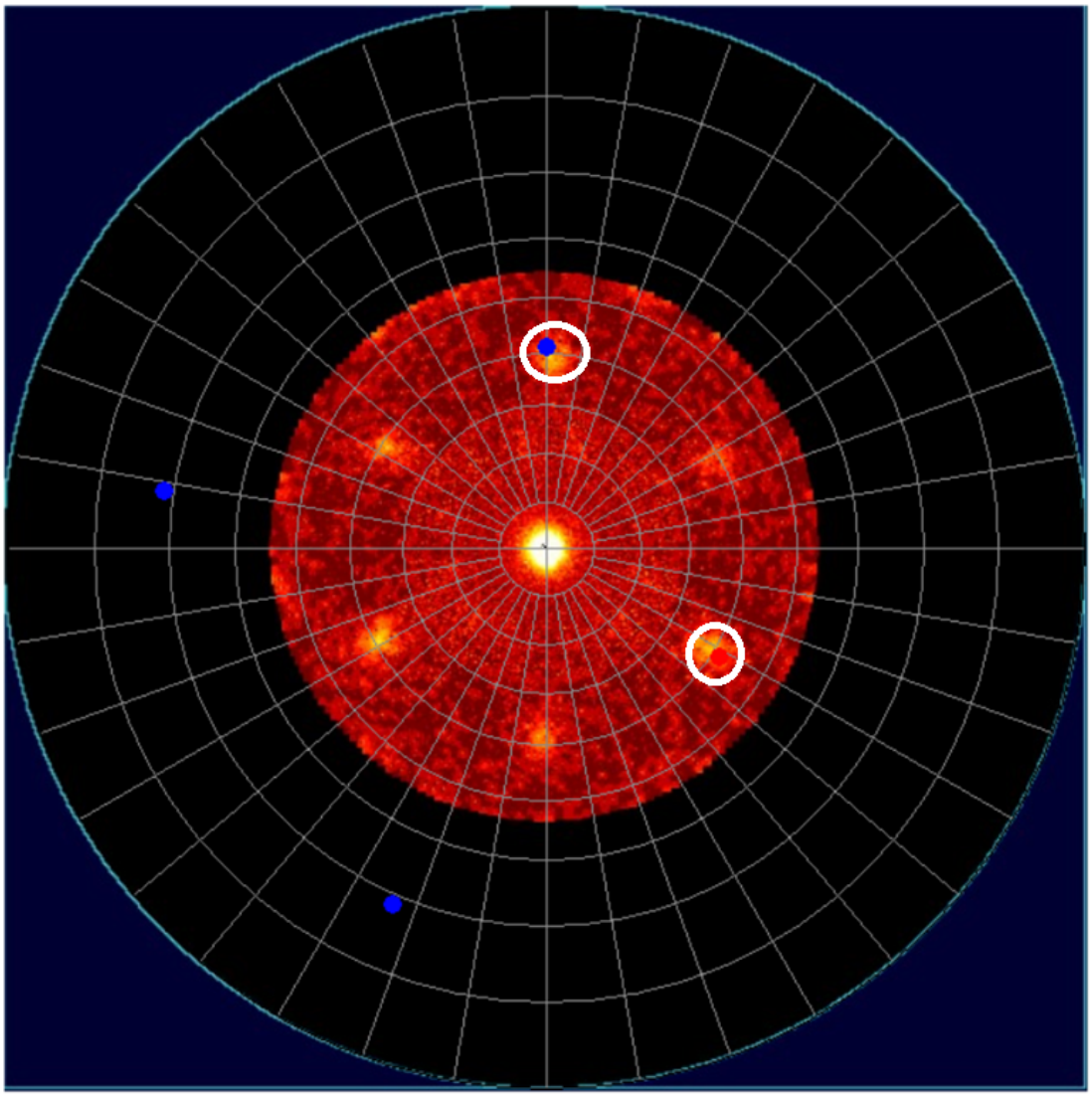

Figure A3.8: Intensity peaks for the (111) family of planes corresponding to type-A; (111) substrates.

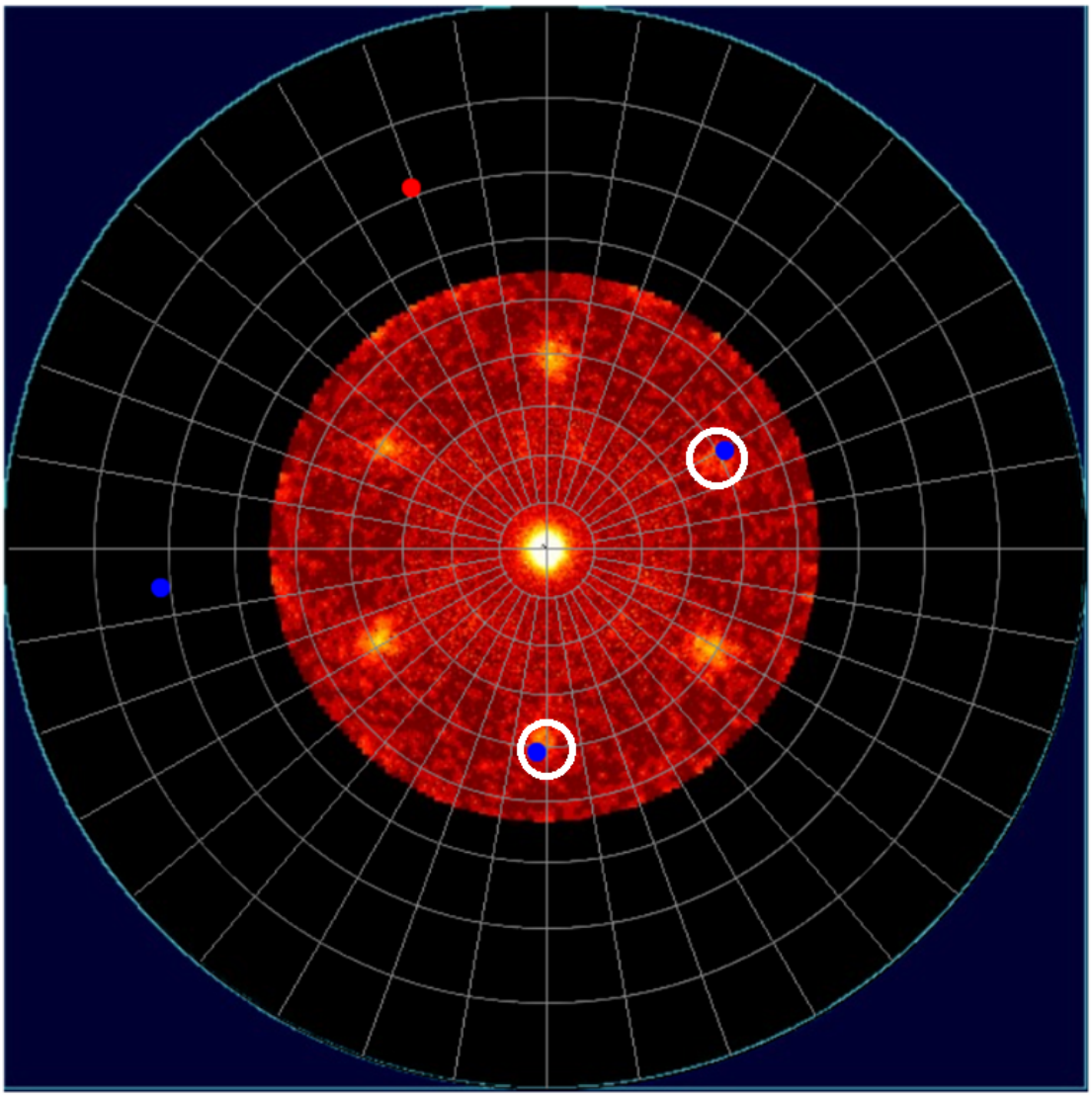

Figure A3.9: Intensity peaks for the (111) family of planes corresponding to type-B; (111) substrates.

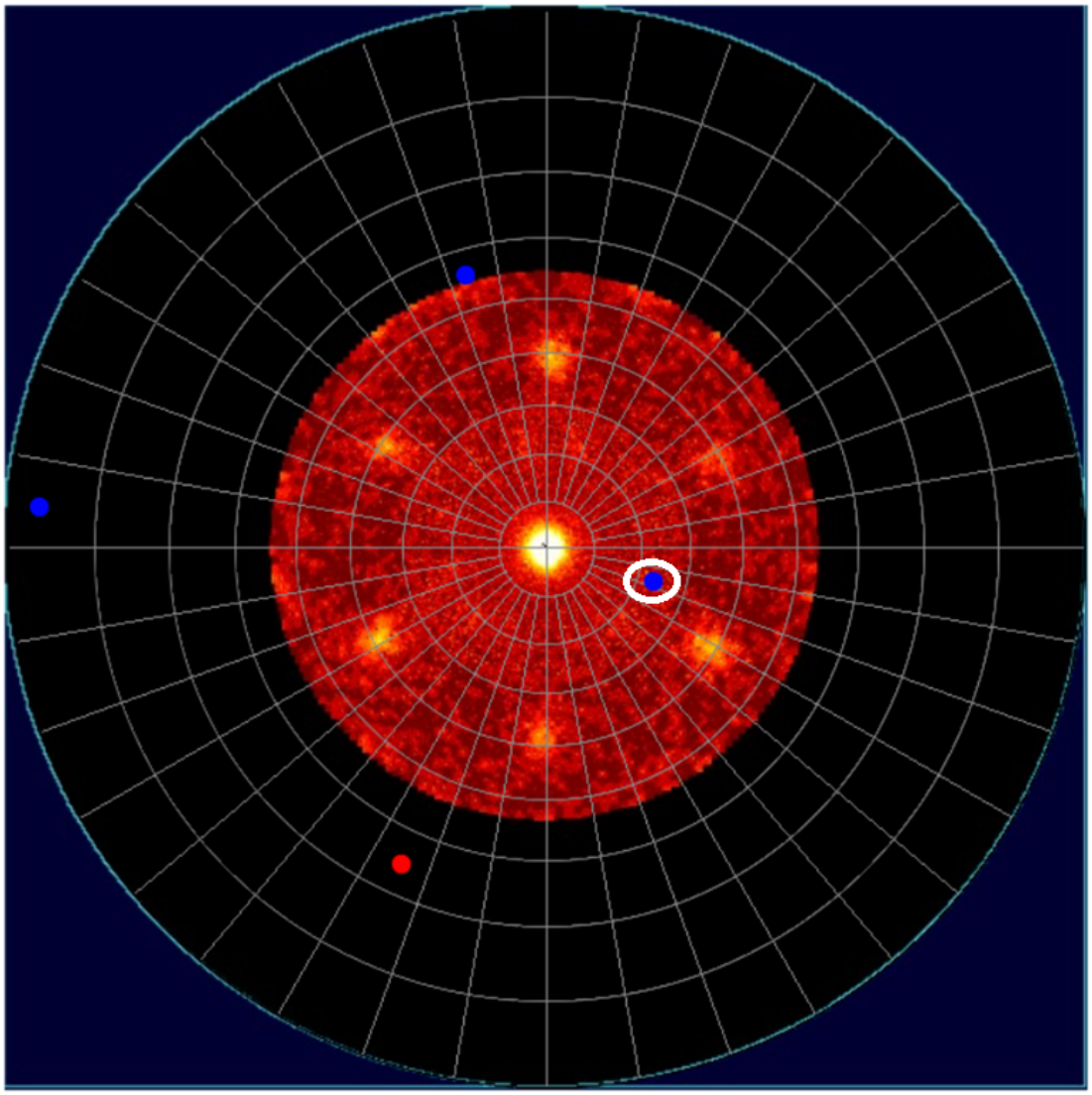

Figure A3.10: Intensity peaks for the (111) family of planes corresponding to type-C; (111) substrates.

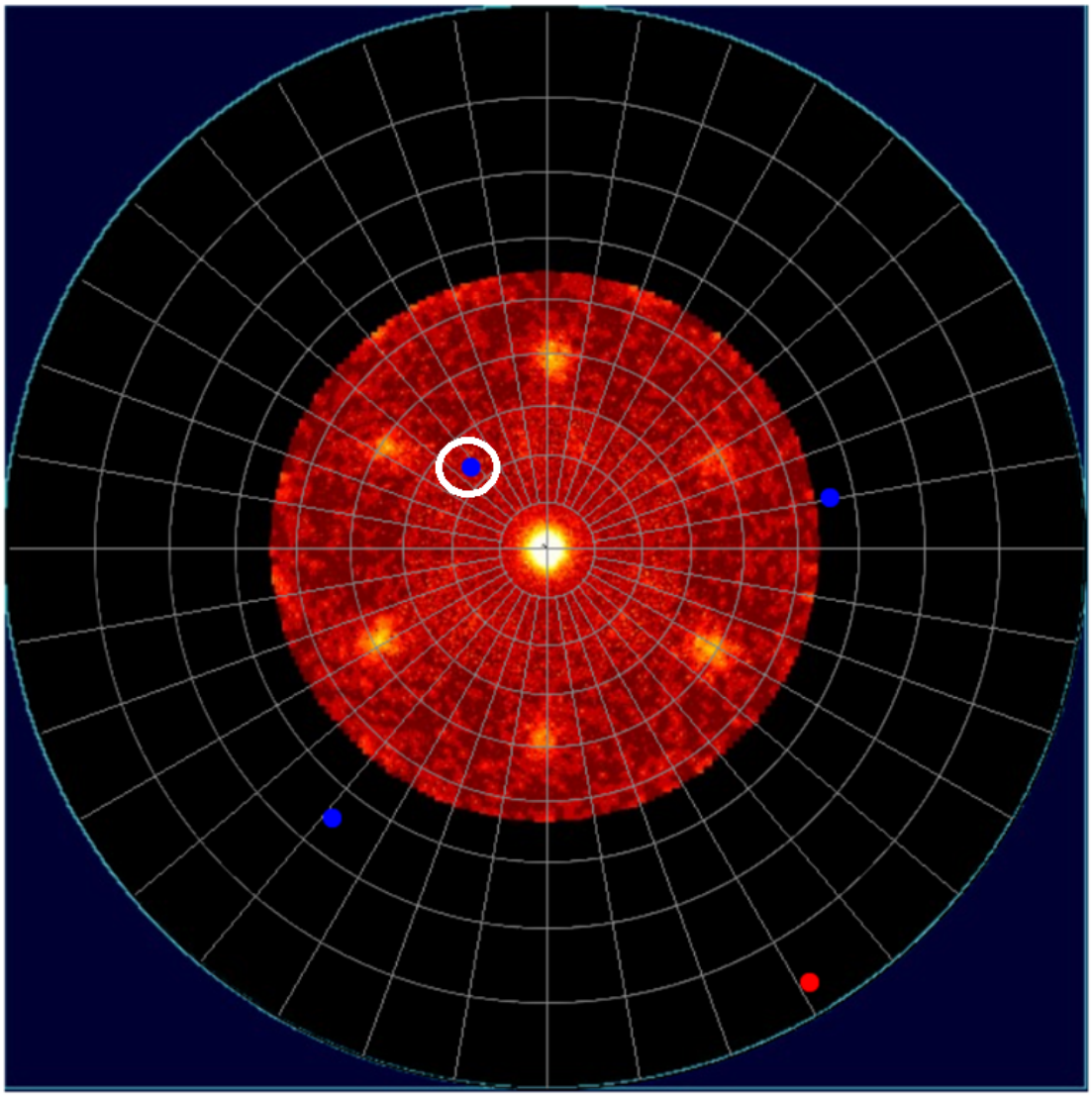

Figure A3.11: Intensity peaks for the (111) family of planes corresponding to type-D; (111) substrates.

A2 (220) pole figures

A2.1 (100) and (100)-4° substrates

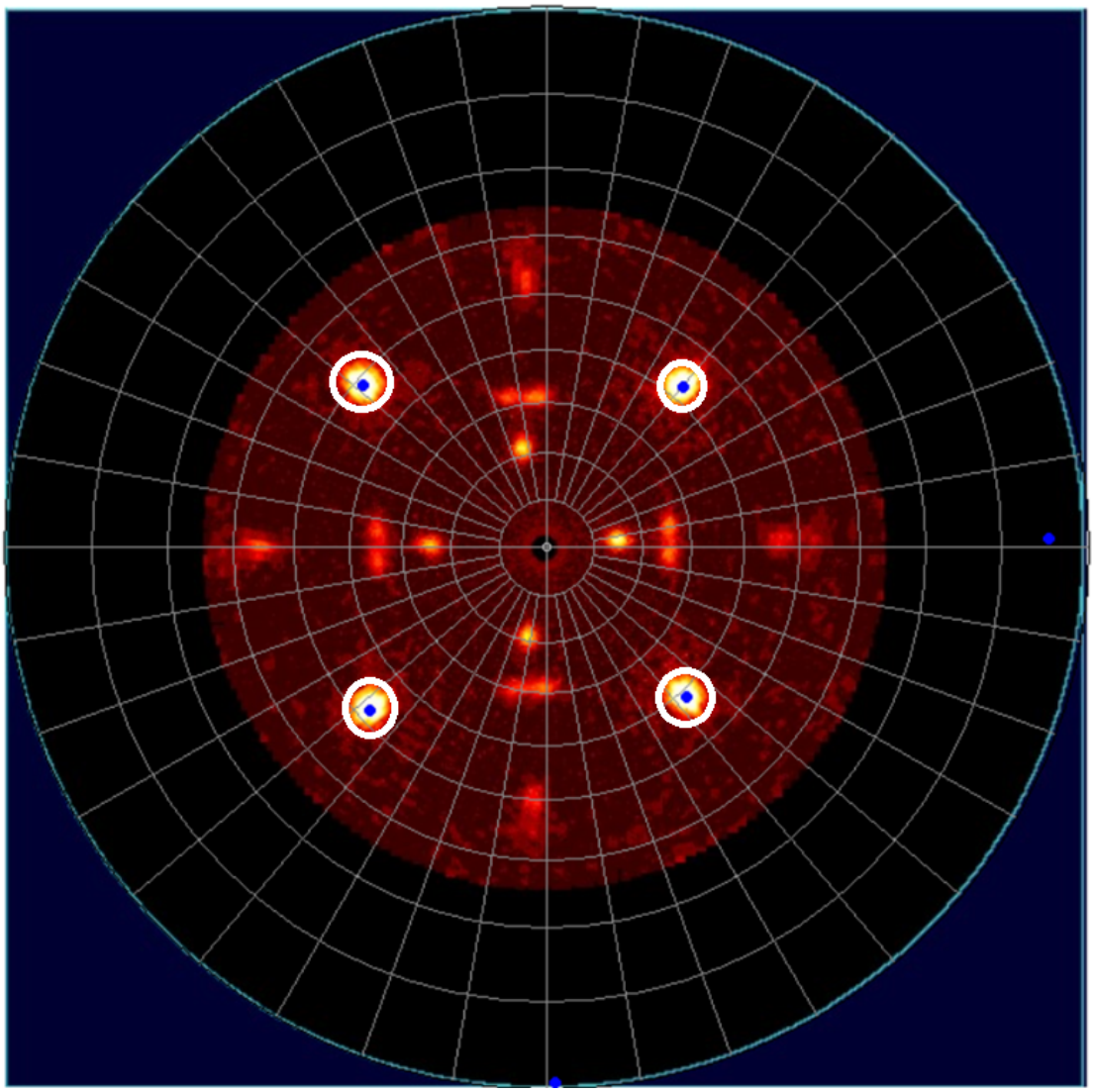

Figure A3.12: Intensity peaks for the (220) family of planes corresponding to the main (100) orientation; (100) and (100)-4° substrates.

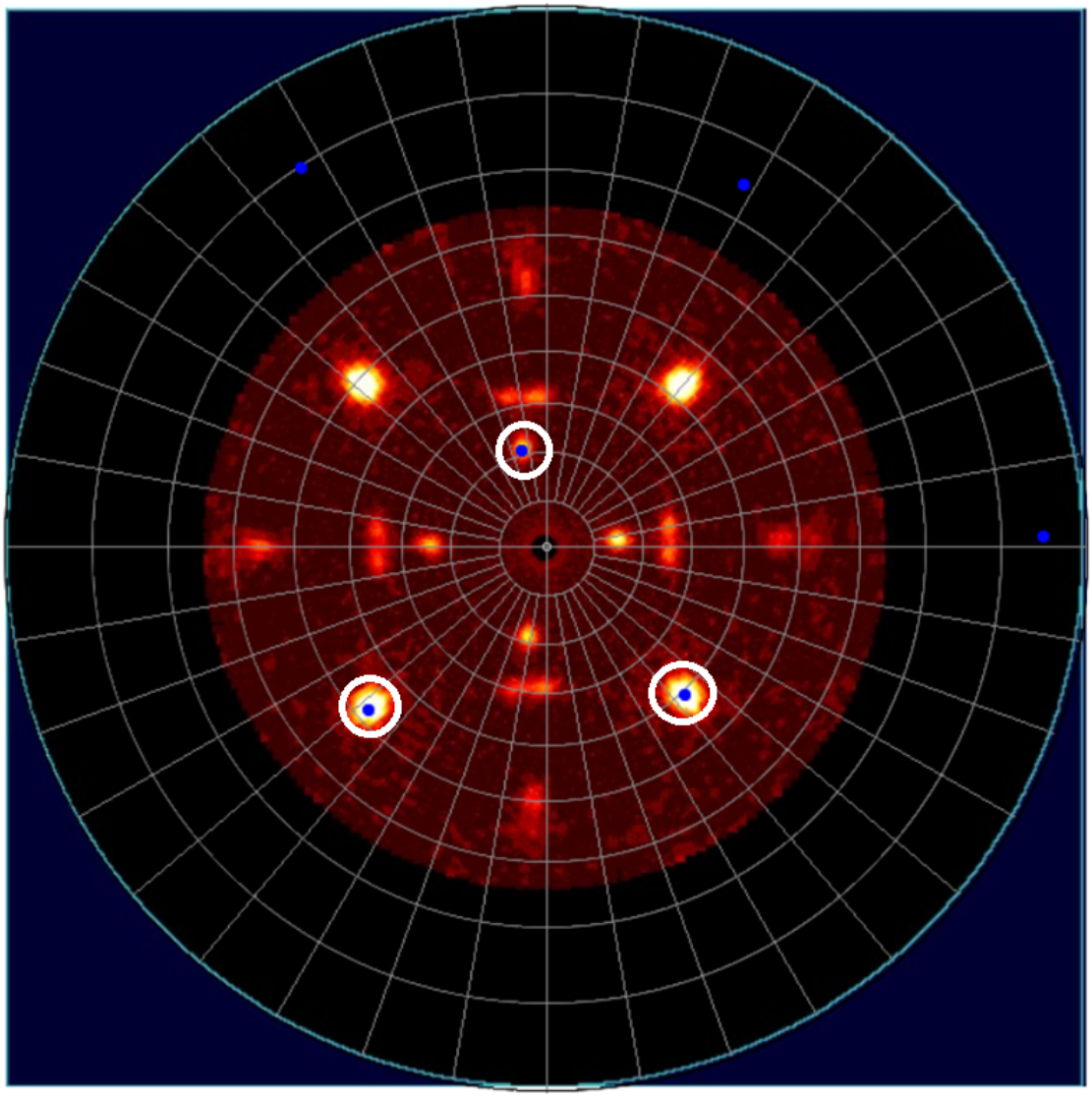

Figure A3.13: Intensity peaks for the (220) family of planes corresponding to type-A twins; (100) and (100)-4° substrates in trials 1, 2, and 4.

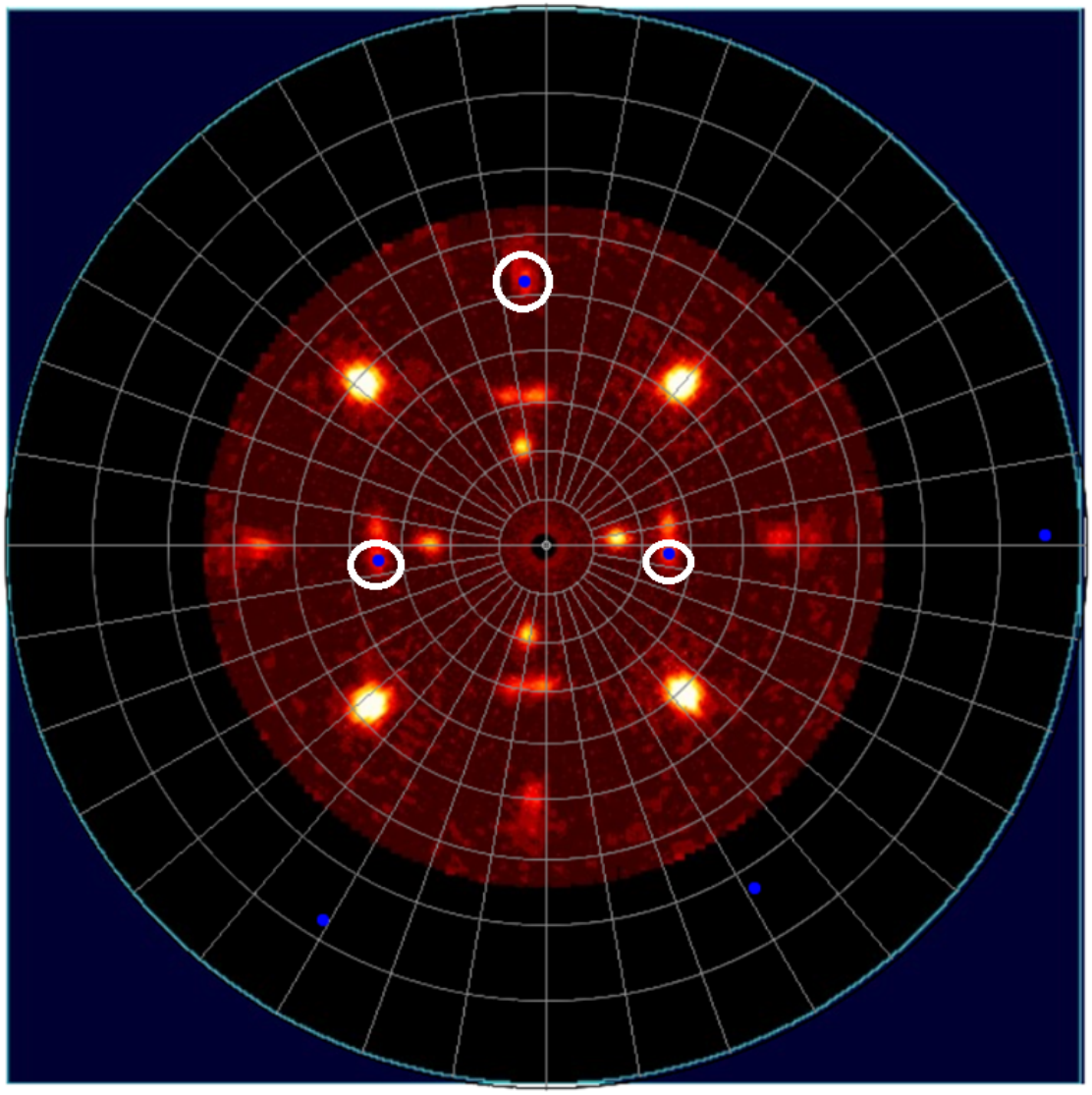

Figure A3.14: Intensity peaks for the (220) family of planes corresponding to type-B twins; (100) and (100)-4° substrates in trials 1, 2, and 4.

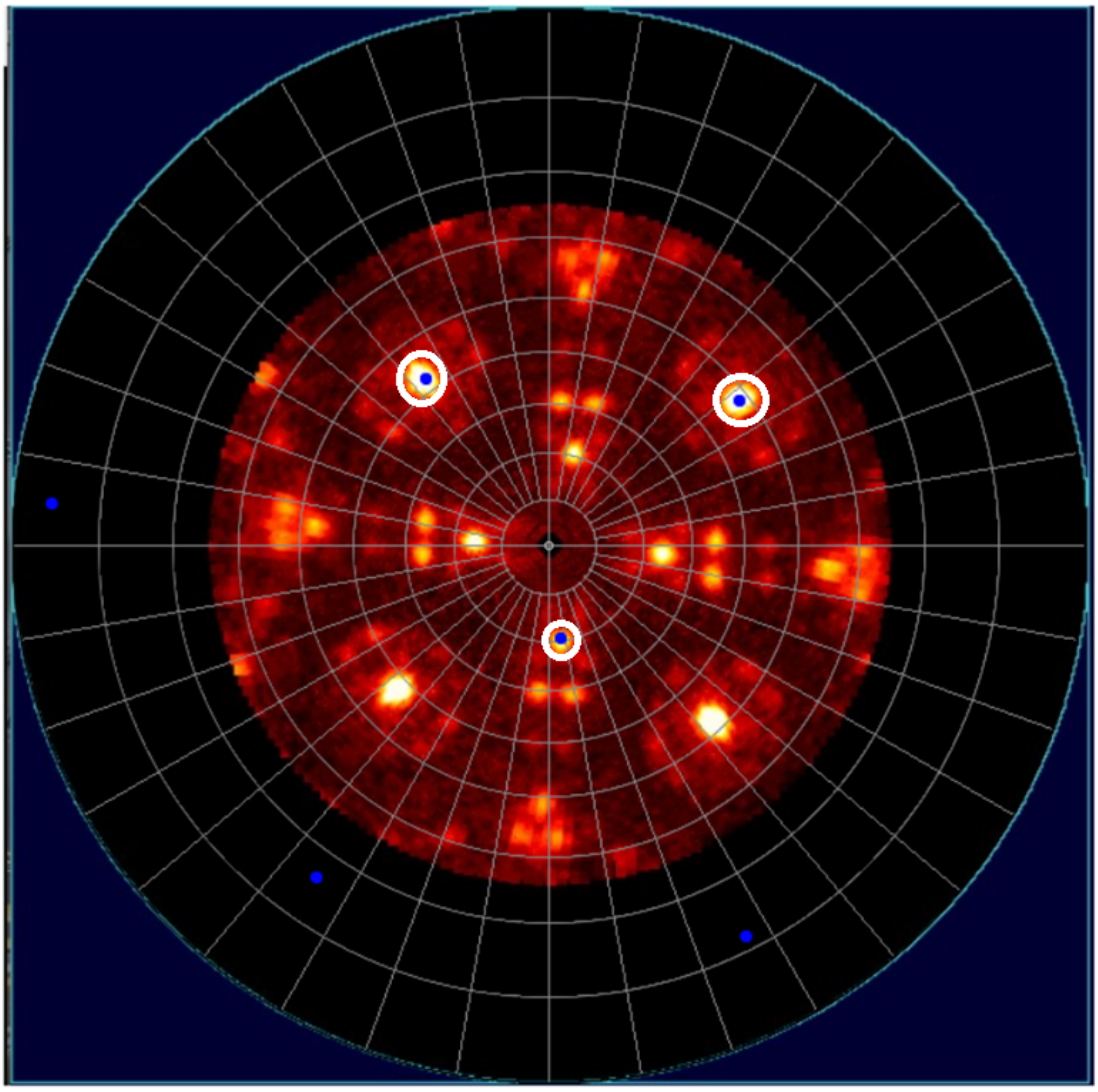

Figure A3.15: Intensity peaks for the (220) family of planes corresponding to type-A twins; (100) and (100)-4° substrates in trial 3.

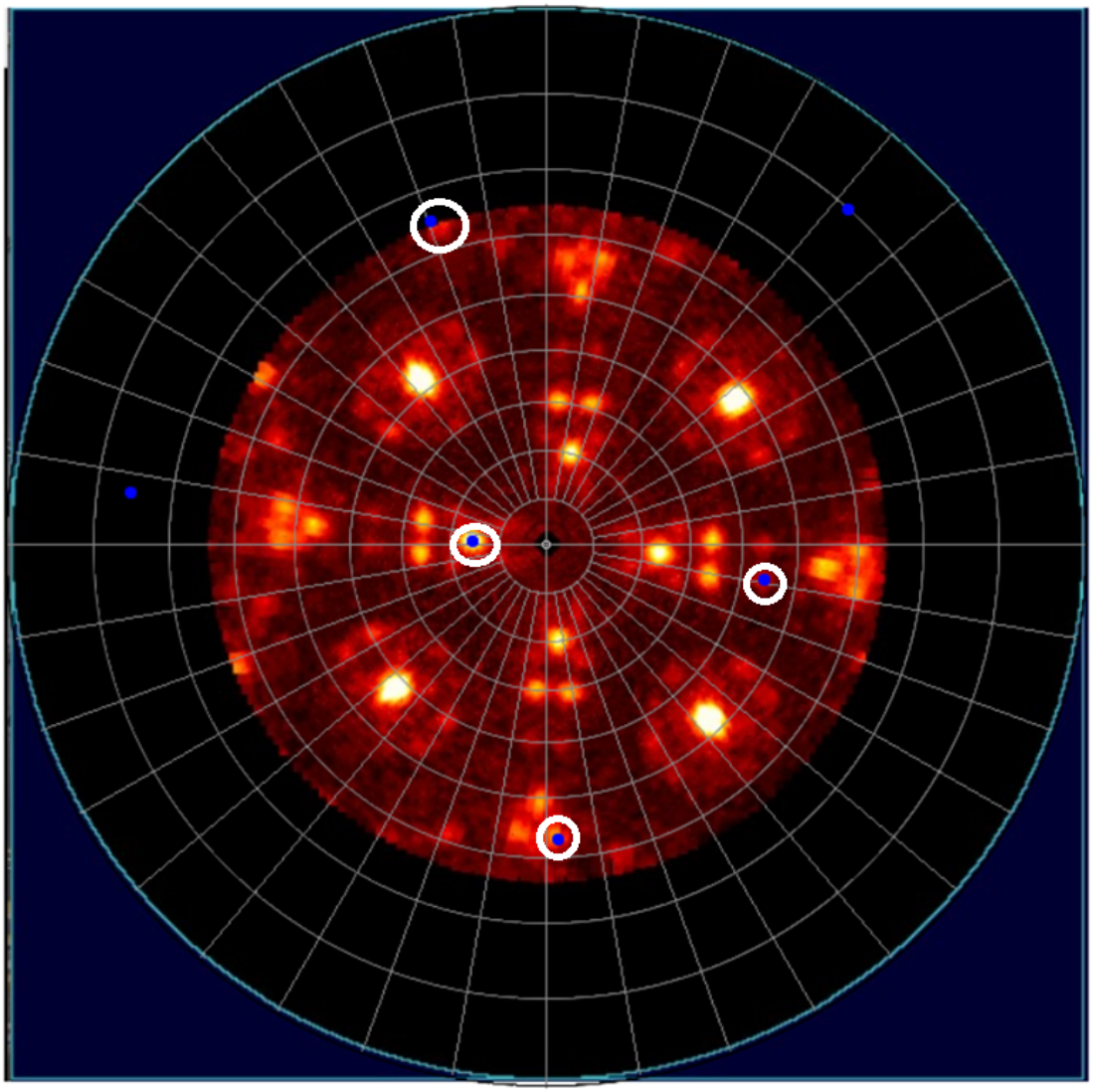

Figure A3.16: Intensity peaks for the (220) family of planes corresponding to type-B twins; (100) and (100)-4° substrates in trial 3.

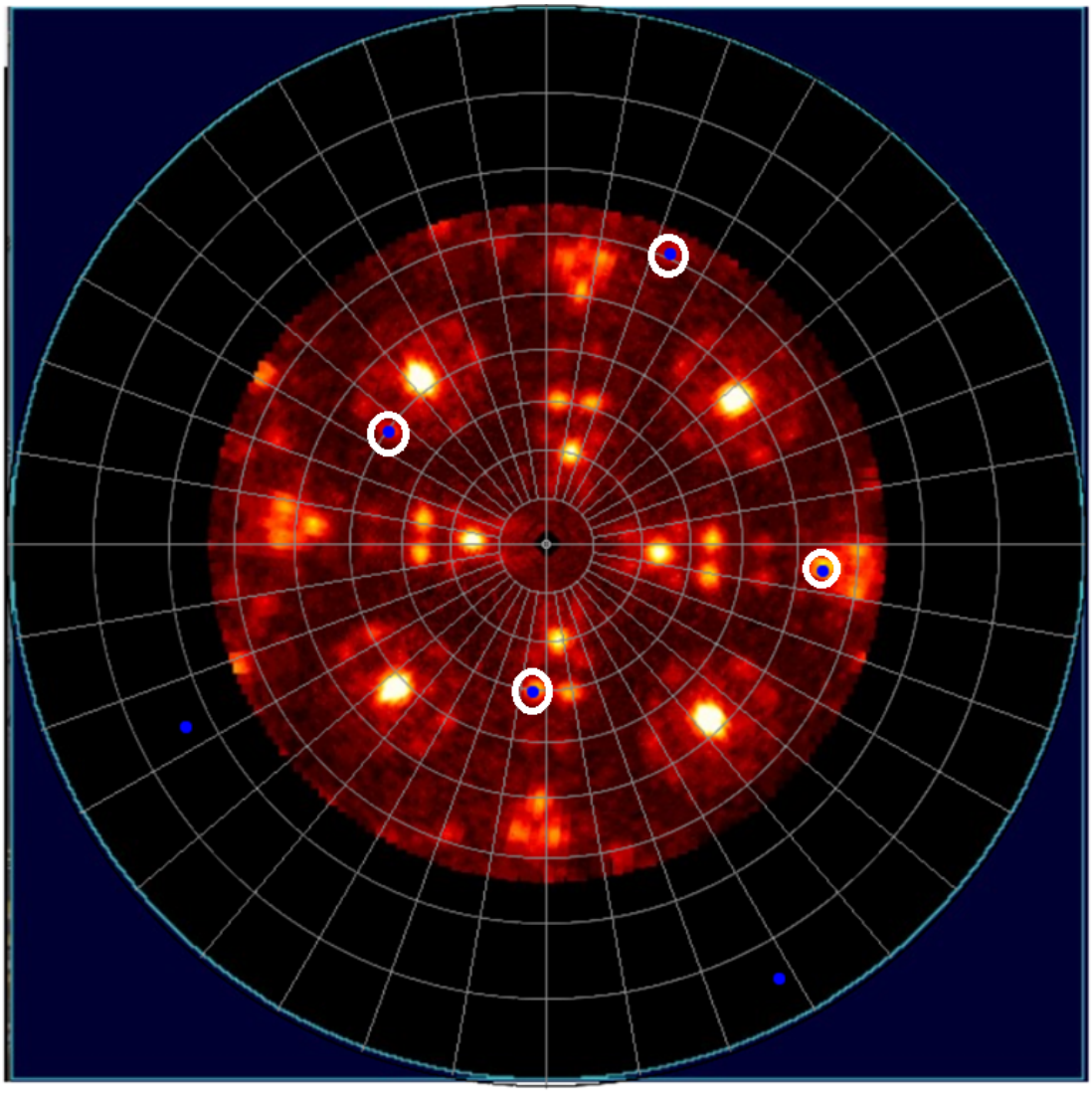

Figure A3.17: Intensity peaks for the (220) family of planes corresponding to type-C twins; (100) and (100)-4° substrates in trial 3.

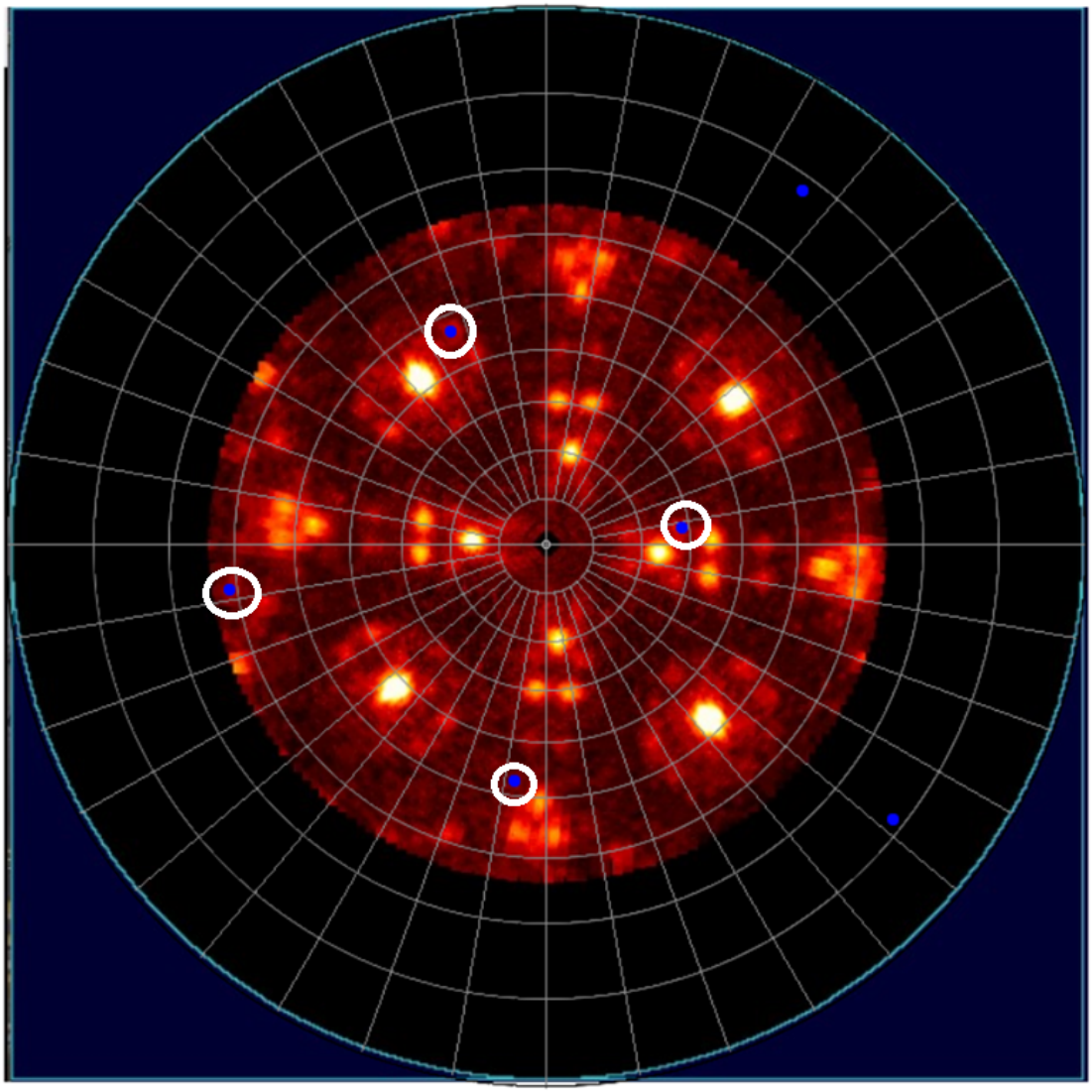

Figure A3.18: Intensity peaks for the (220) family of planes corresponding to type-D twins; (100) and (100)-4° substrates in trial 3.

A2.2 (111) substrates

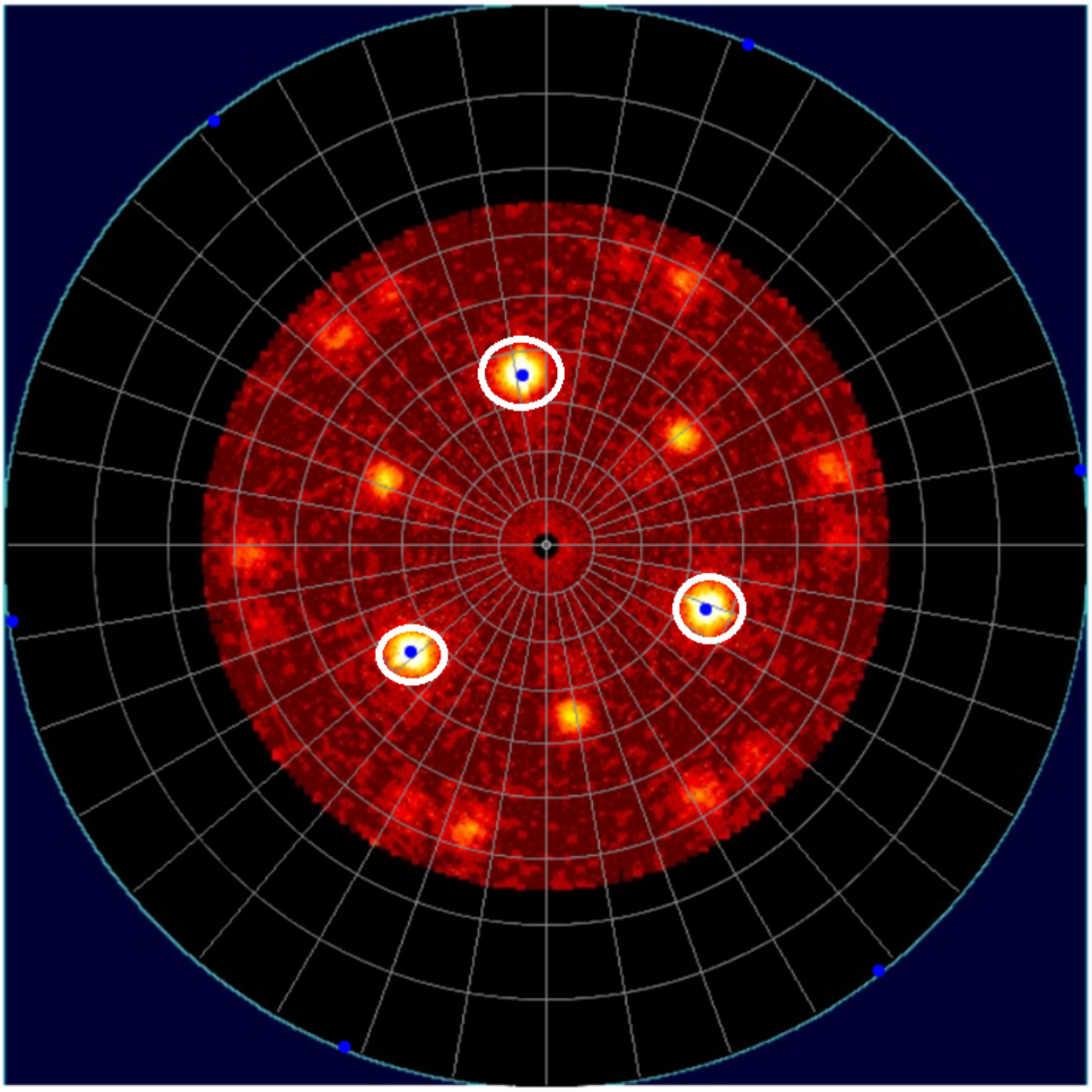

Figure A3.19: Intensity peaks for the (220) family of planes corresponding to the main (111) orientation; (111) substrates.

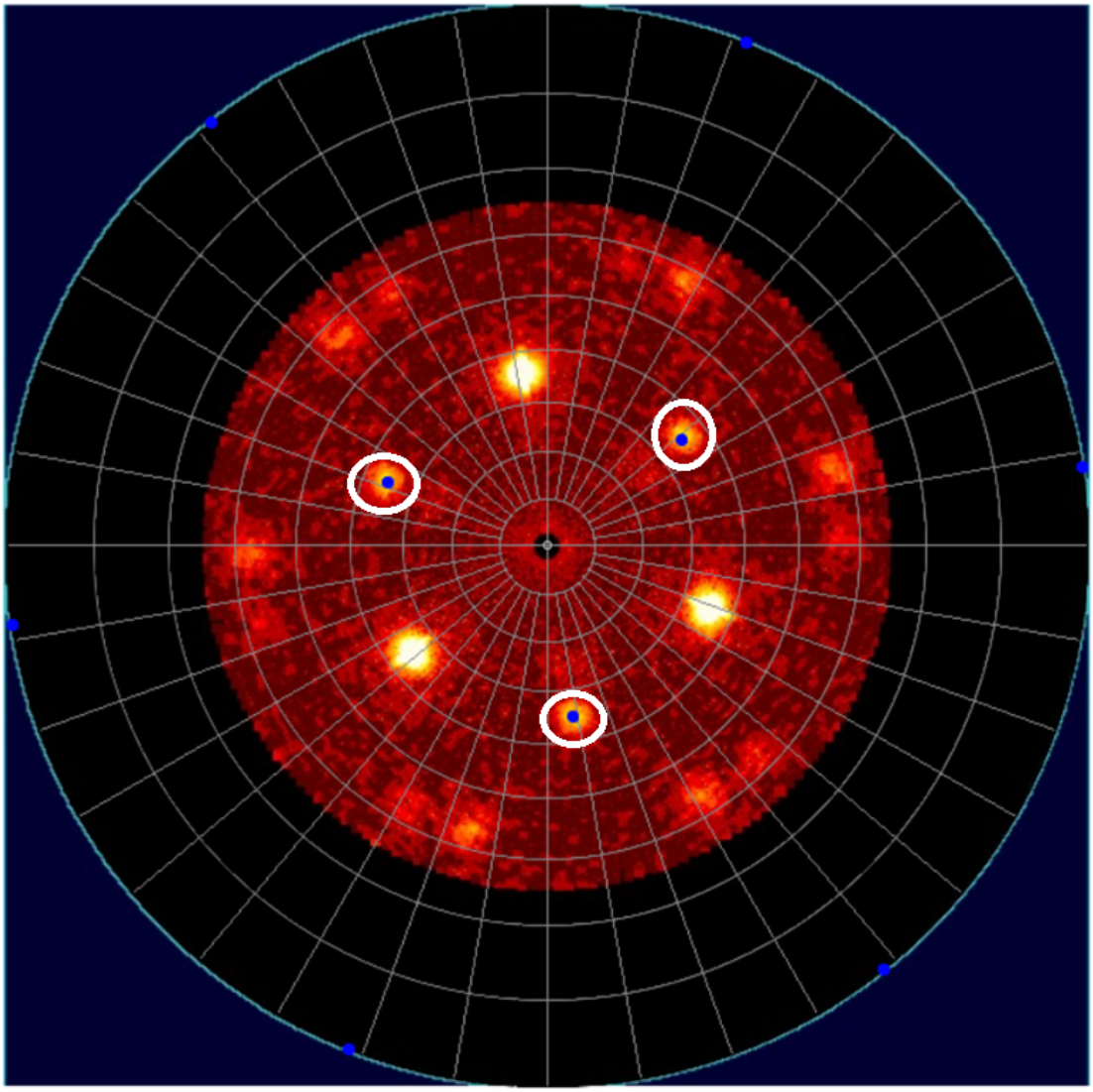

Figure A3.20: Intensity peaks for the (220) family of planes corresponding to type-A twins; (111) substrates.

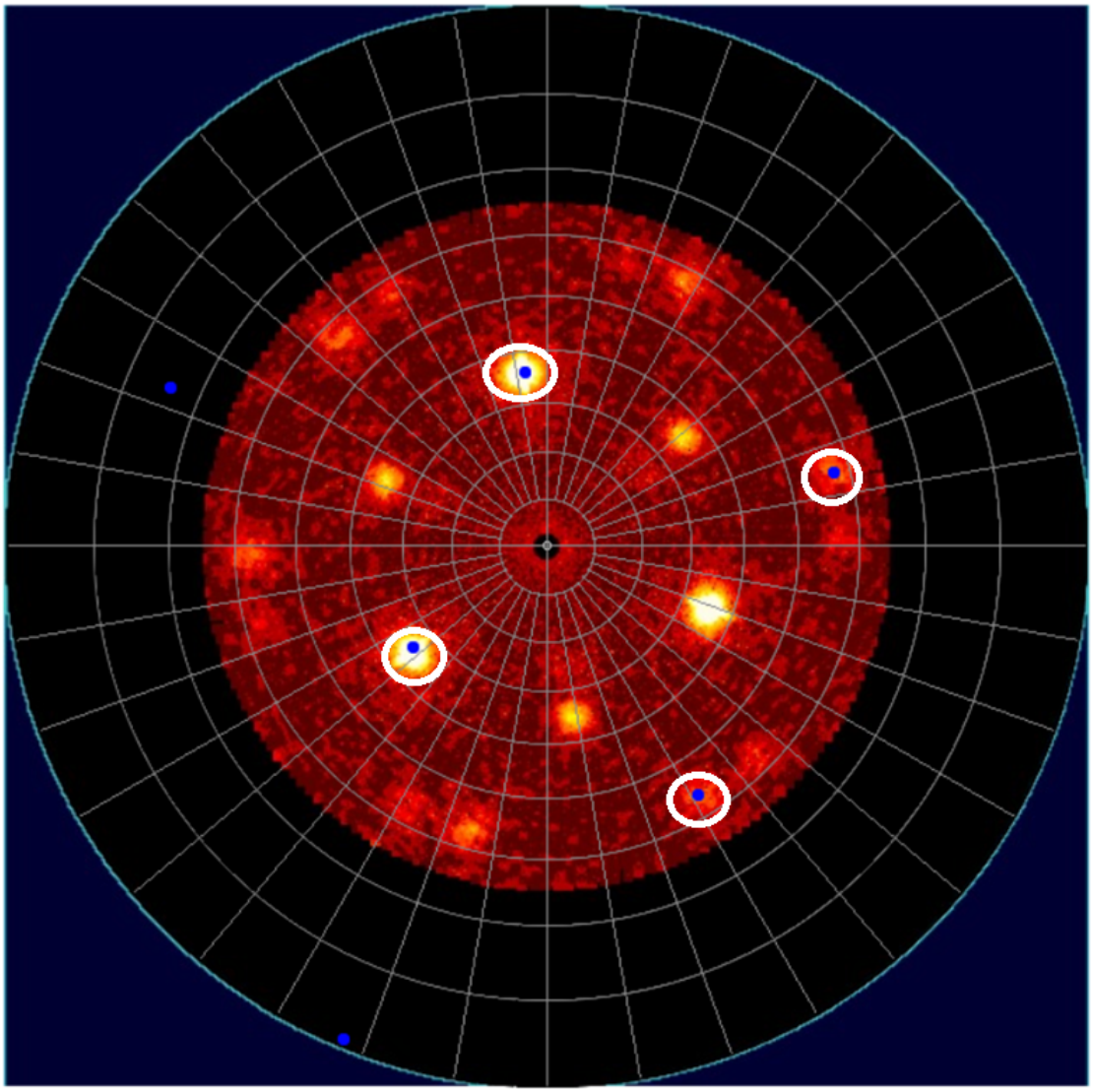

Figure A3.21: Intensity peaks for the (220) family of planes corresponding to type-B twins; (111) substrates.

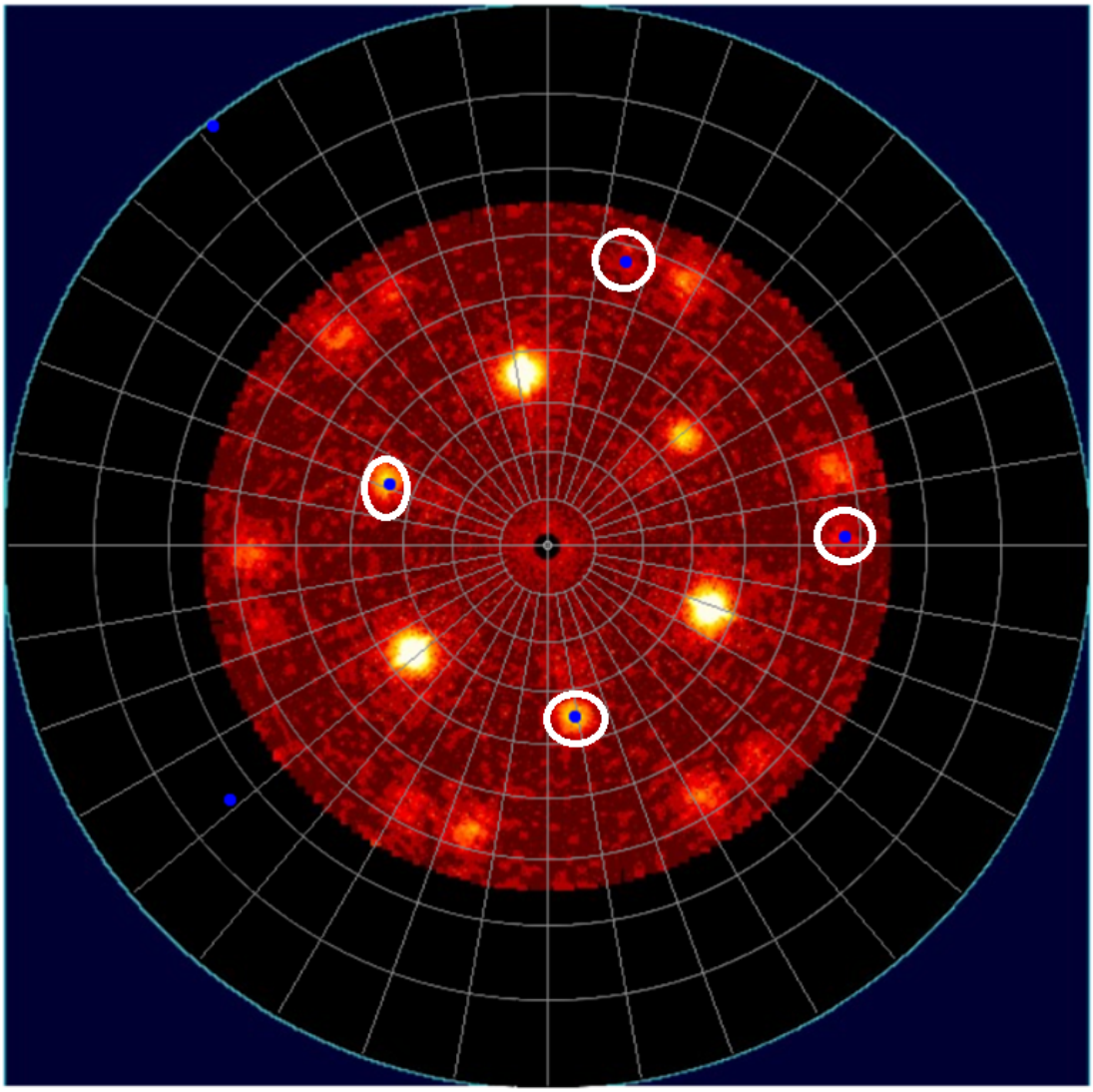

Figure A3.22: Intensity peaks for the (220) family of planes corresponding to type-C twins; (111) substrates.

A3 (311) pole figures

A3.1 (100) and (100)-4° substrates

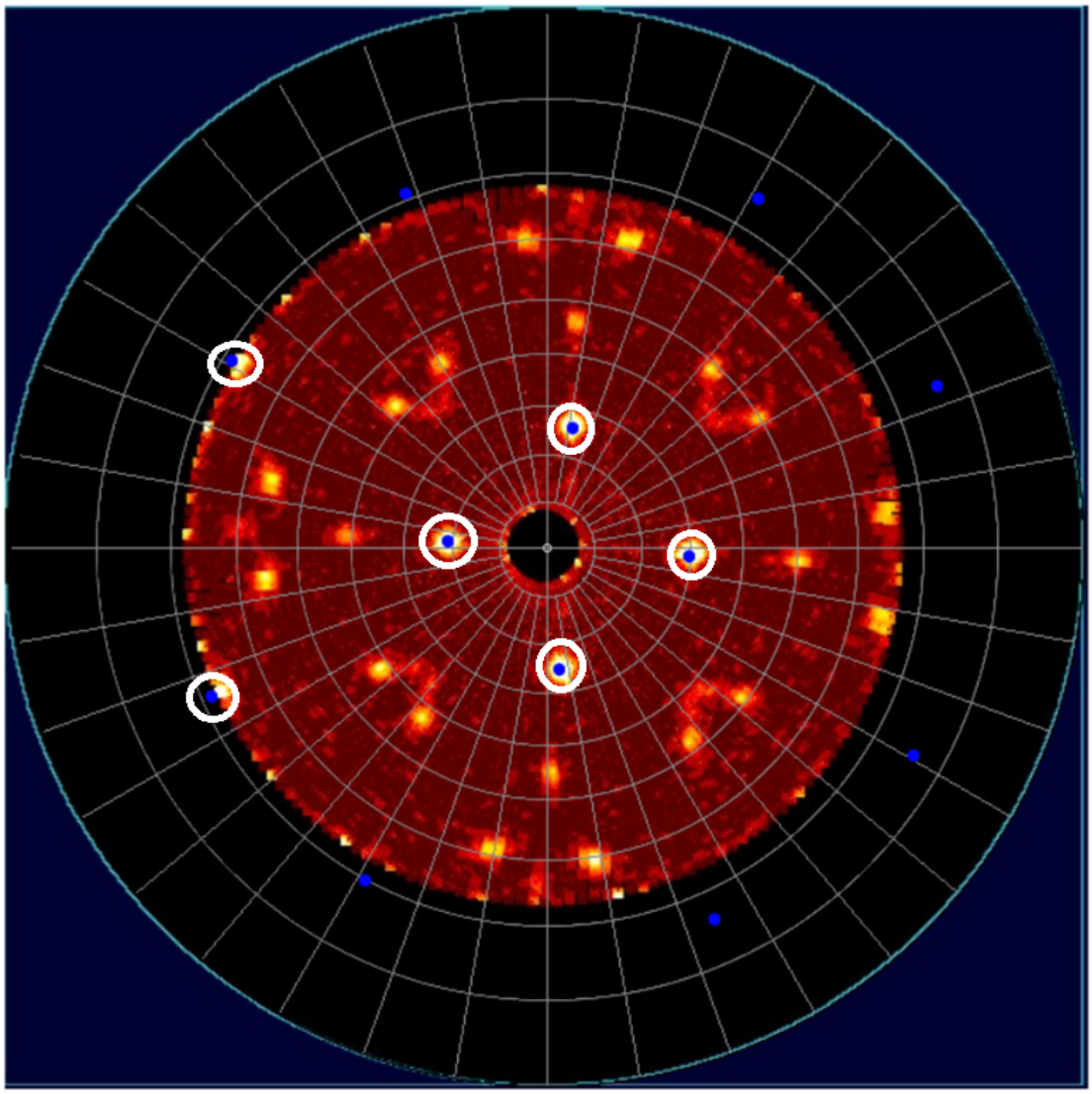

Figure A3.23: Intensity peaks for the (311) family of planes corresponding to the main (100) orientation; (100) and (100)-4° substrates in trials 1-4.

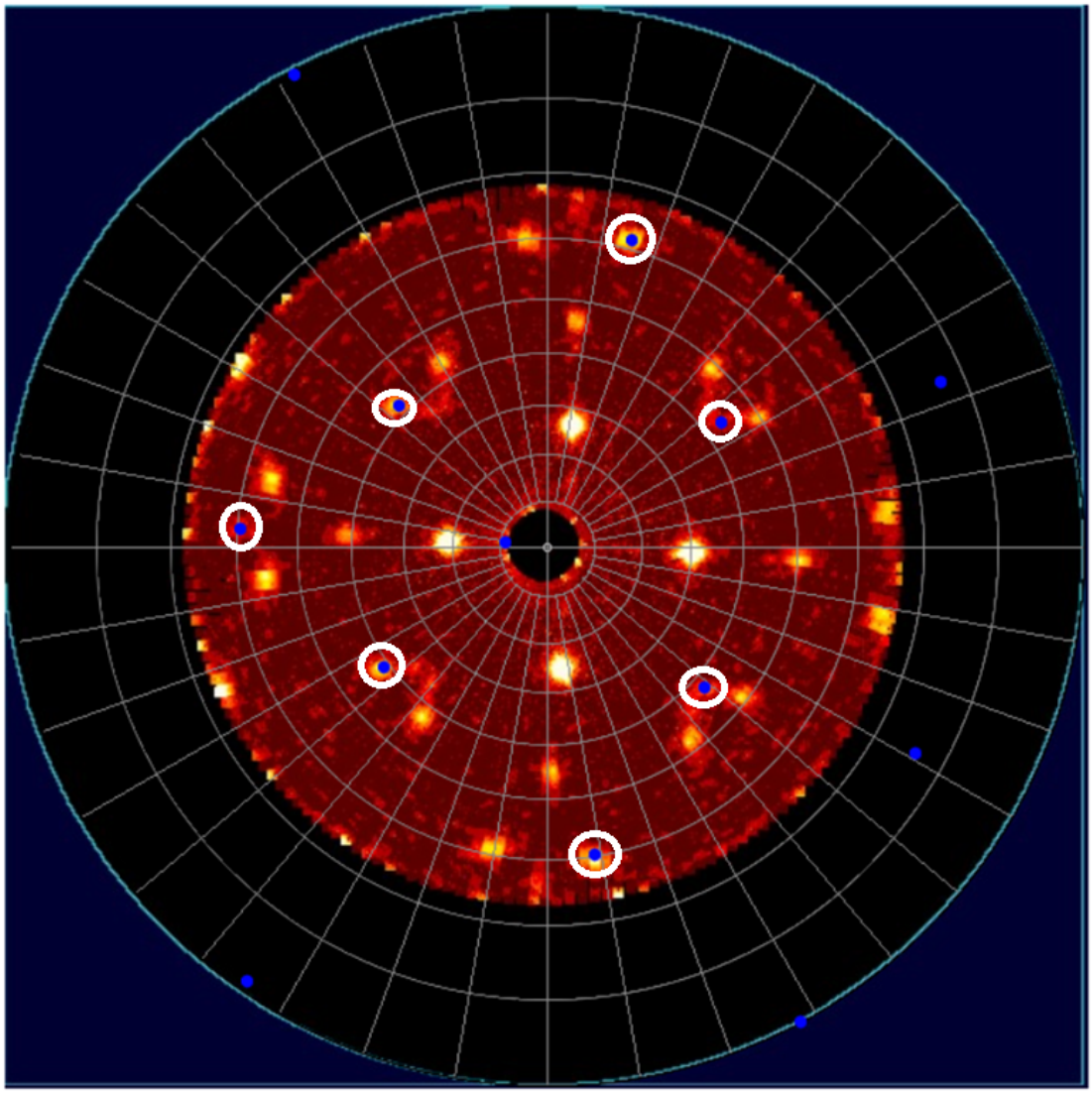

Figure A3.24: Intensity peaks for the (311) family of planes corresponding to type-A twins; (100) and (100)-4° substrates in trials 1, 2, and 4.

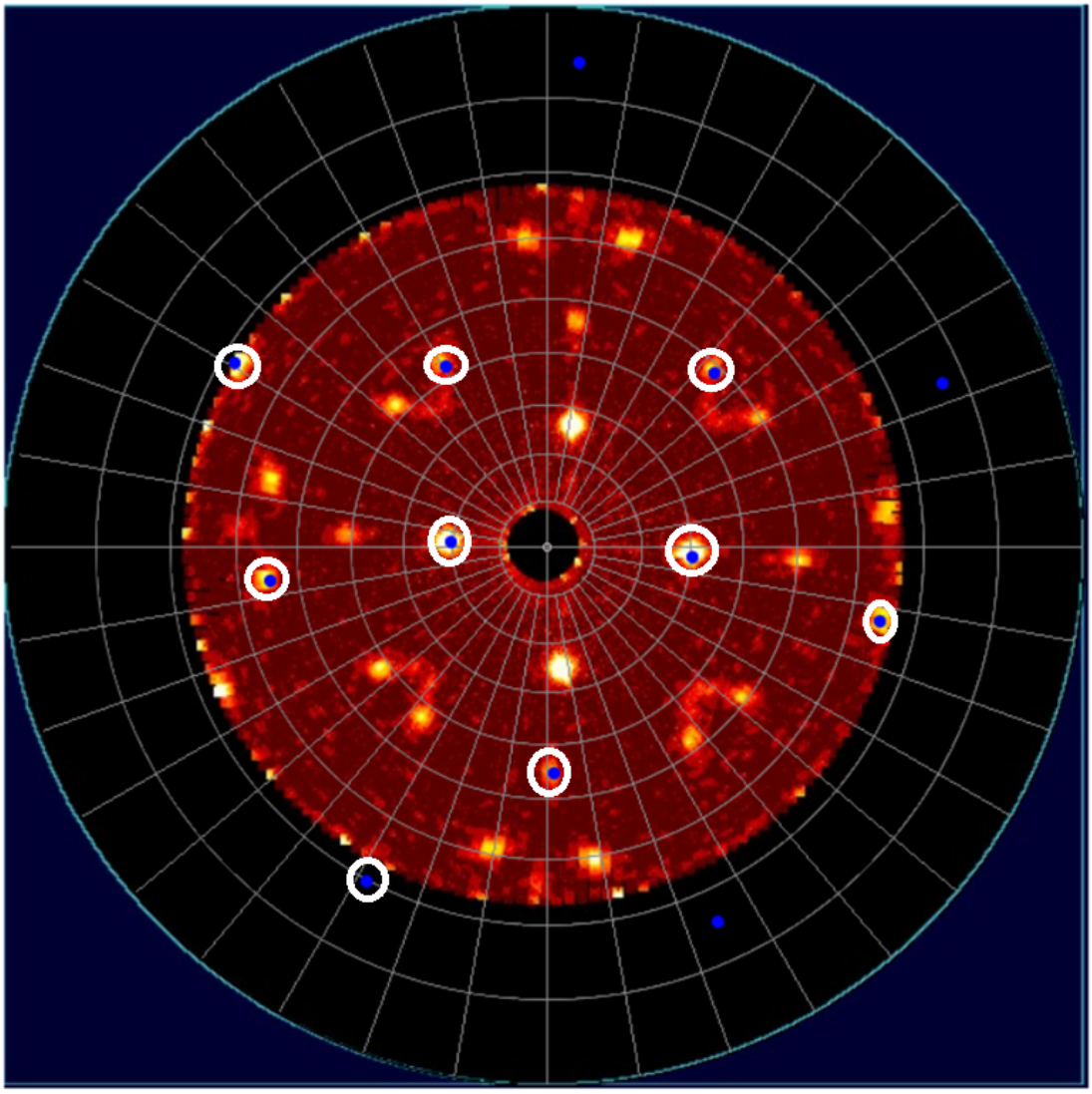

Figure A3.25: Intensity peaks for the (311) family of planes corresponding to type-B twins; (100) and (100)-4° substrates in trials 1, 2, and 4.

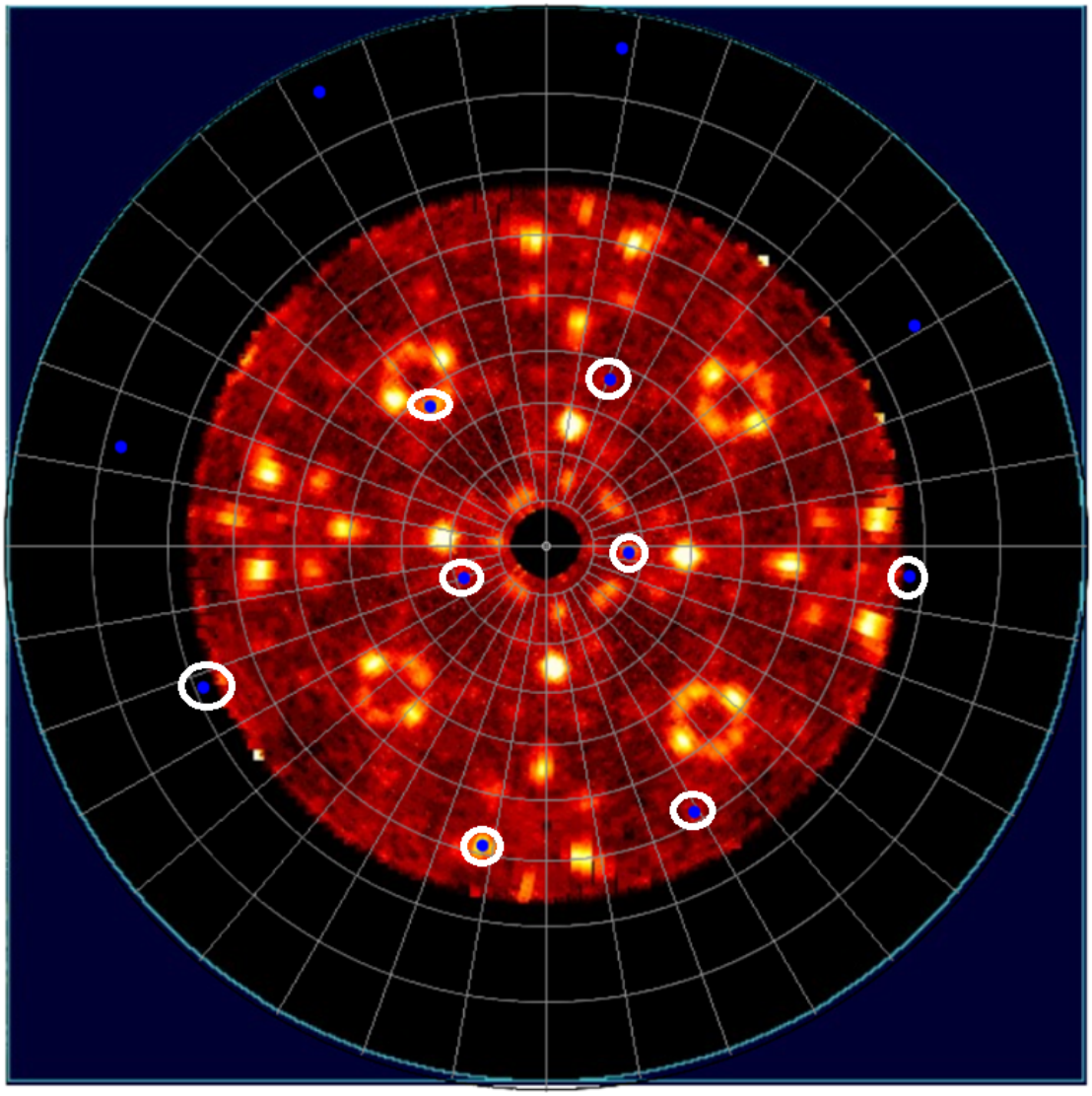

Figure A3.26: Intensity peaks for the (311) family of planes corresponding to type-A twins; (100) and (100)-4° substrates in trial 3.

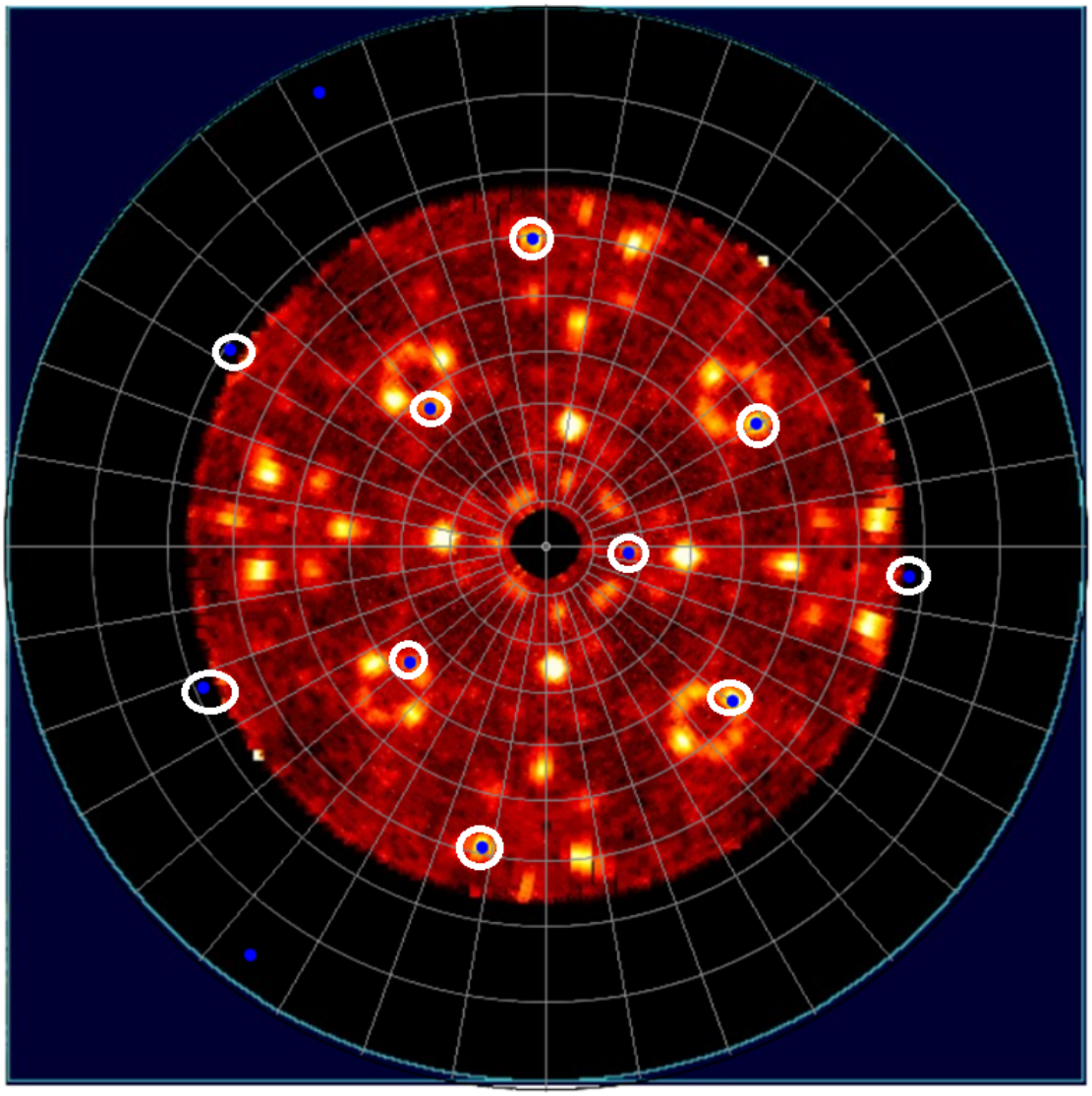

Figure A3.27: Intensity peaks for the (311) family of planes corresponding to type-C twins; (100) and (100)-4° substrates in trial 3.

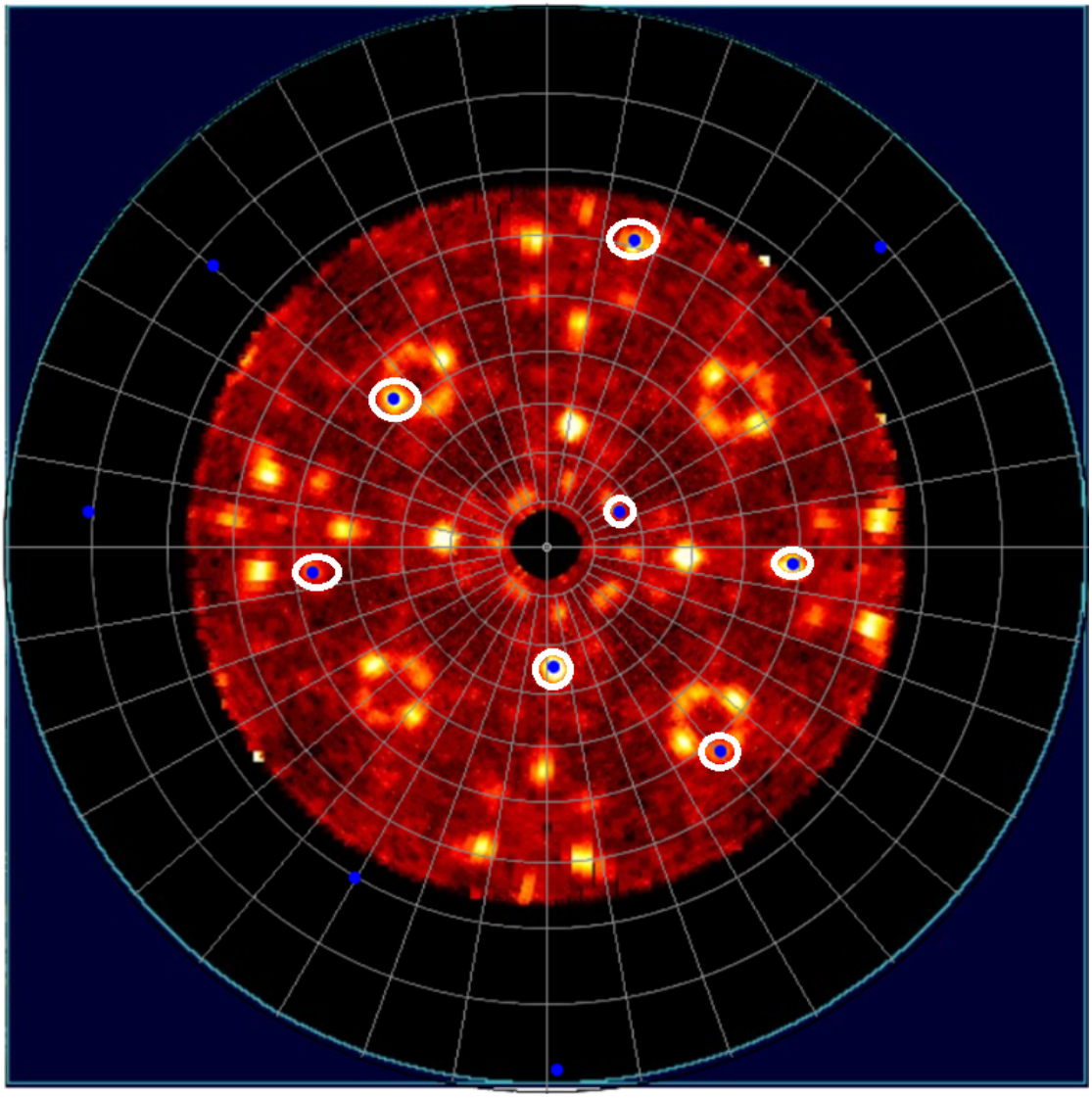

Figure A3.28: Intensity peaks for the (311) family of planes corresponding to type-D twins; (100) and (100)-4° substrates in trial 3.

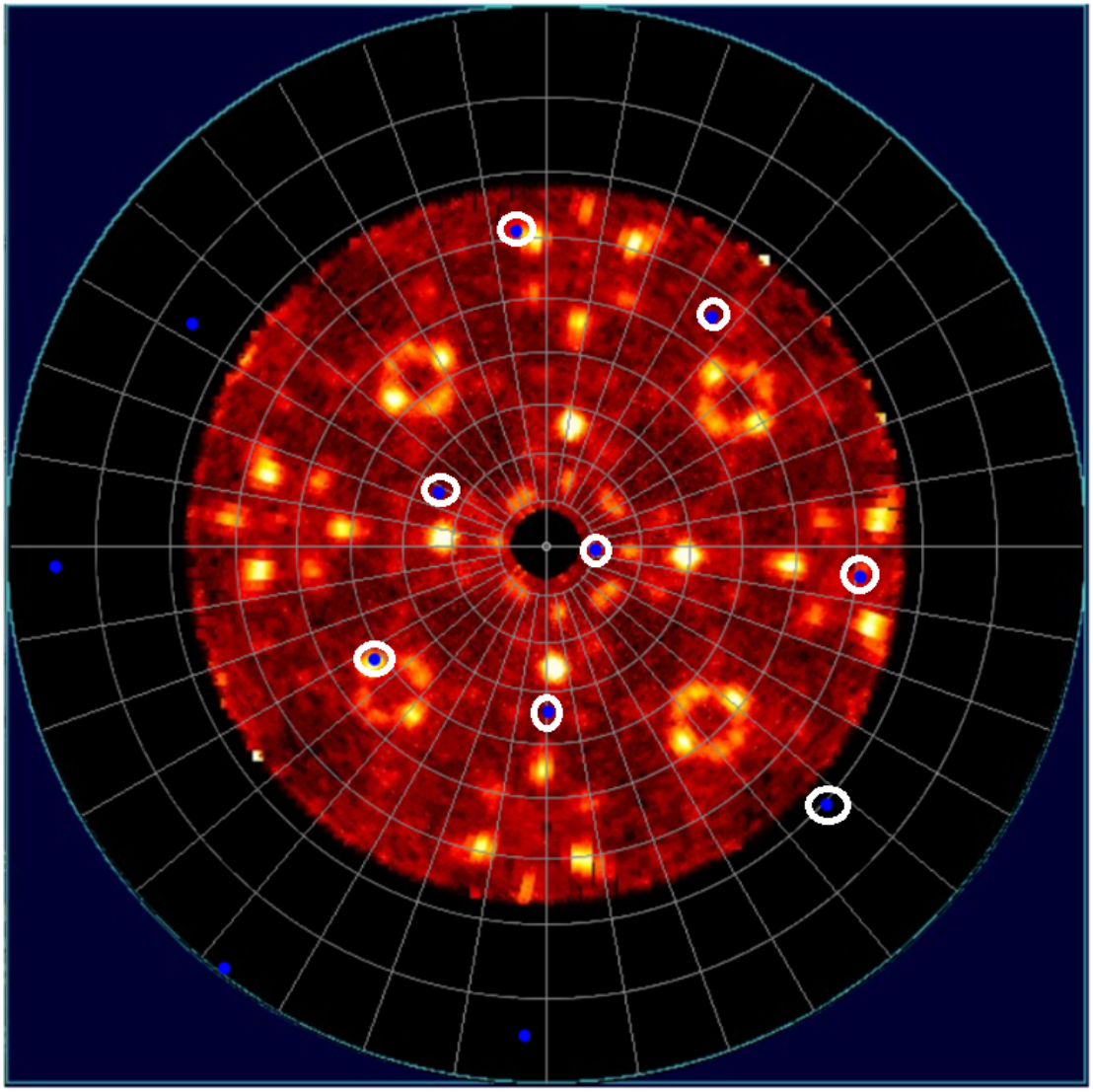

Figure A3.29: Intensity peaks for the (311) family of planes corresponding to type-E twins; (100) and (100)-4° substrates in trial 3.

A3.2 (111) substrates

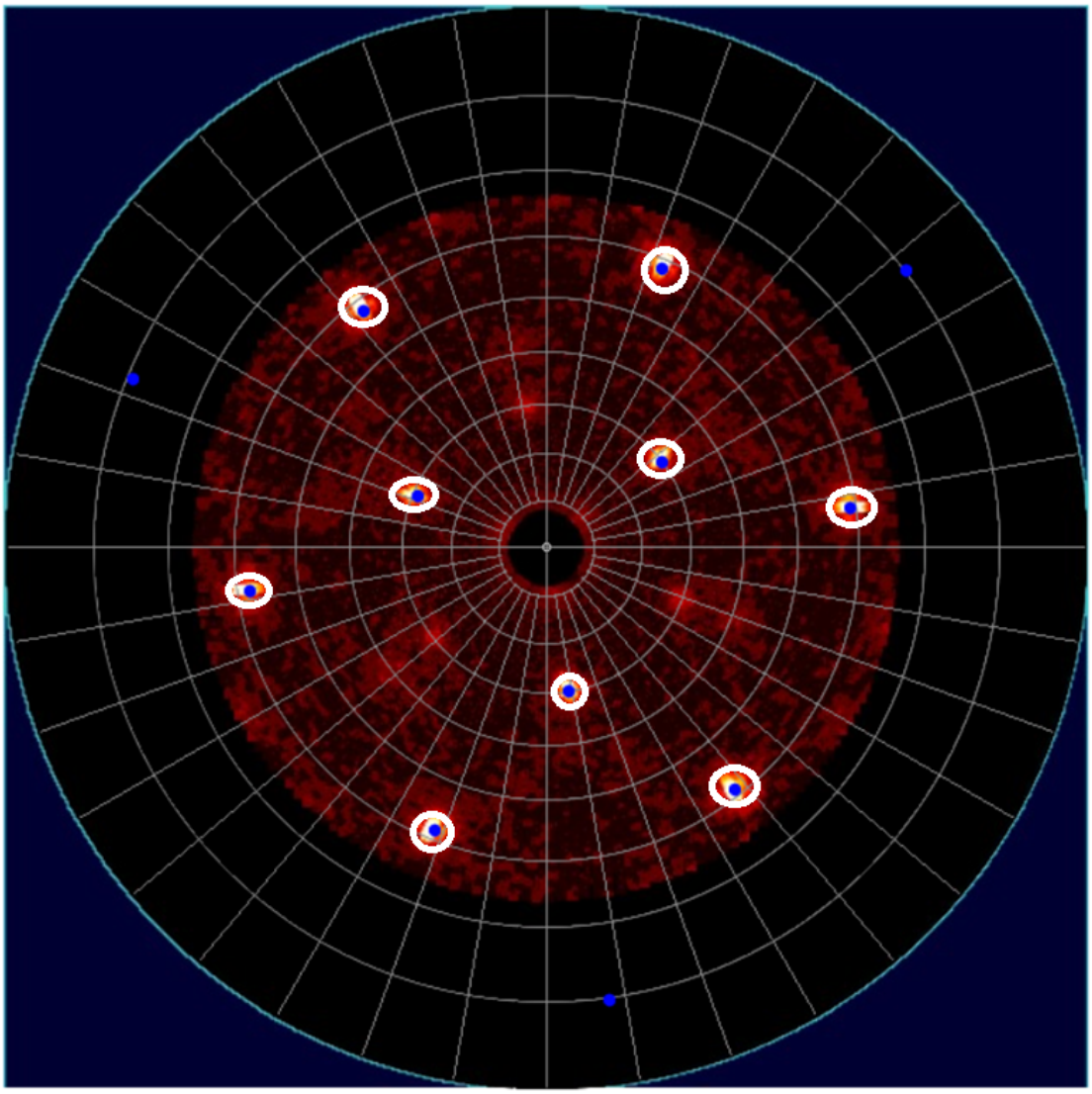

Figure A3.30: Intensity peaks for the (311) family of planes corresponding to the main (111) orientation; (111) substrates.

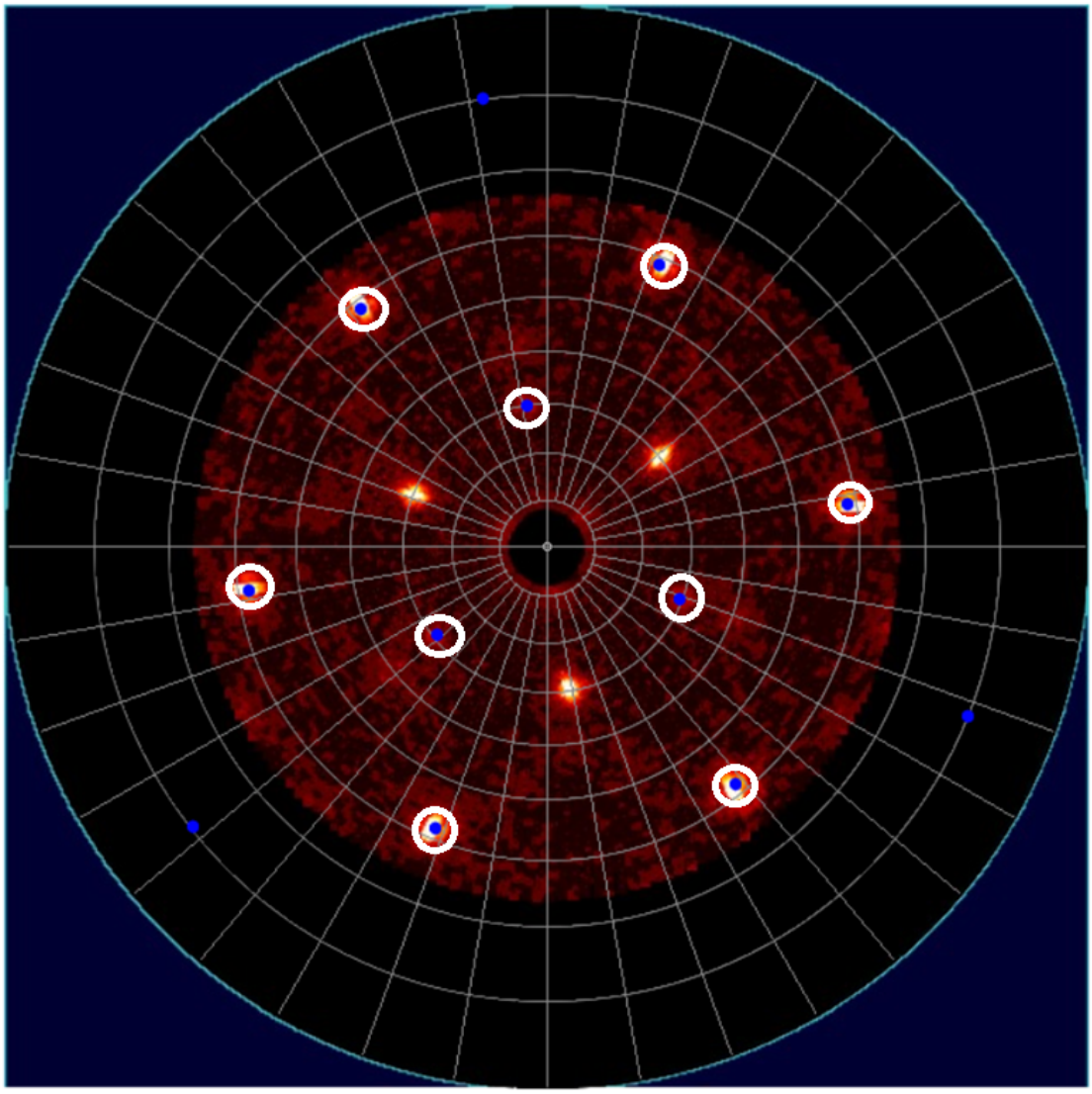

Figure A3.31: Intensity peaks for the (311) family of planes corresponding to type-A twins; (111) substrates.

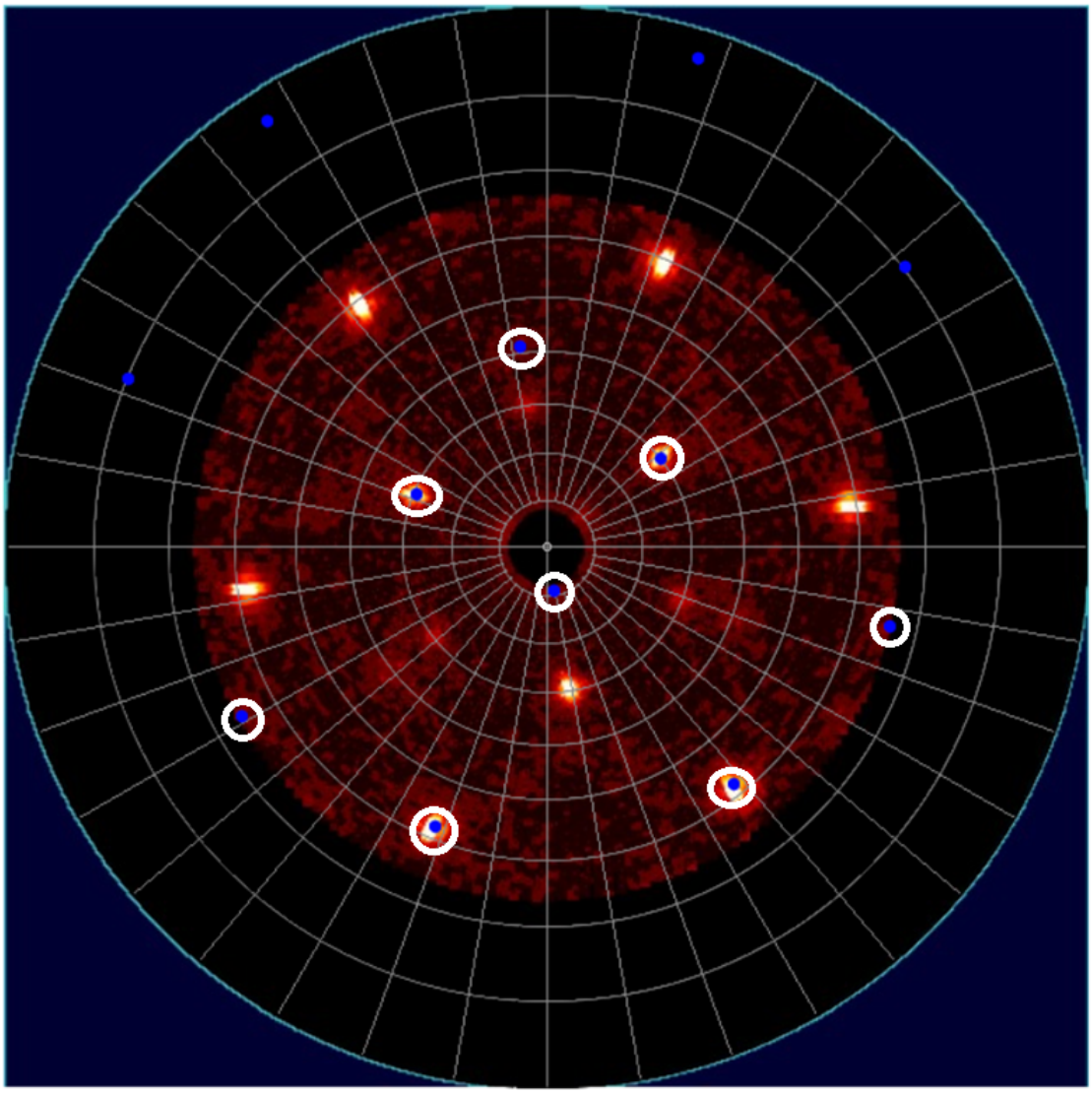

Figure A3.32: Intensity peaks for the (311) family of planes corresponding to type-B twins; (111) substrates.

Bibliography

[1] J. R. Chelikowsky and M. L. Cohen. Nonlocal pseudopotential calculations for the electronic structure of eleven diamond and zinc-blende semiconductors. *Phys. Rev. B* 14 (2 July 1976), 556–582.

[2] M. Melli, M. West, S. Hickman, S. Dhuey, D. Lin, M. Khorasaninejad, C. Chang, S. Jolly, H. Tae, E. Poliakov, P. S. Hilaire, S. Cabrini, C. Peroz, and M. Klug. Gallium phosphide optical metasurfaces for visible light applications. *Scientific Reports* 10(20694) (Nov. 2020).

[3] M. Feifel, J. Ohlmann, J. Benick, T. Rachow, S. Janz, M. Hermle, F. Dimroth, J. Belz, A. Beyer, K. Volz, and D. Lackner. MOVPE Grown Gallium Phosphide–Silicon Heterojunction Solar Cells. *IEEE Journal of Photovoltaics* 7(2) (2017), 502–507.

[4] V. Tassev, M. Snure, R. Peterson, K. L. Schepler, R. Bedford, M. Mann, S. Vangala, W. Goodhue, A. Lin, J. Harris, M. Fejer, and P. Schunemann. Progress in orientation-patterned GaP for next-generation nonlinear optical devices. In: *Nonlinear Frequency Generation and Conversion: Materials, Devices, and Applications XII*. Ed. by K. L. Vodopyanov. Vol. 8604. International Society for Optics and Photonics. SPIE, 2013, 120–128.

[5] K. Termkoa, S. Vangala, W. Goodhue, R. Peterson, R. Bedford, V. Tassev, C. Lynch, and D. Bliss. Production of orientation-patterned GaP templates using wafer fusion techniques. *Optical Materials* 34(1) (2011), 30–35. ISSN: 0925-3467.

[6] L. E. Myers, R. C. Eckardt, M. M. Fejer, R. L. Byer, W. R. Bosenberg, and J. W. Pierce. Quasi-phase-matched optical parametric oscillators in bulk periodically poled LiNbO3. *J. Opt. Soc. Am. B* 12(11) (Nov. 1995), 2102–2116.

[7] J.-P. Meyn and M. M. Fejer. Tunable ultraviolet radiation by second-harmonic generation in periodically poled lithium tantalate. *Opt. Lett.* 22(16) (Aug. 1997), 1214–1216.

[8] M. Fingas and C. Brown. Chapter 5 - Oil Spill Remote Sensing. In: *Oil Spill Science and Technology (Second Edition)*. Ed. by M. Fingas. Second Edition. Boston: Gulf Professional Publishing, 2017, 305–385. ISBN: 978-0-12-809413-6.

[9] N. Ashcroft and N. Mermin. *Solid State Physics*. Cengage Learning, 2011. ISBN: 9788131500521.

[10] D. S. Hum and M. M. Fejer. Quasi-phasematching. *Comptes Rendus Physique* 8(2) (2007). Recent advances in crystal optics, 180–198. ISSN: 1631-0705.

[11] T. Kondo, S. Koh, and R. Ito. Sublattice reversal epitaxy: a novel technique for fabricating domain-inverted compound semiconductor structures. *Science and Technology of Advanced Materials* 1(3) (2000), 173–179.

[12] R. Paschotta. *Quasi-phase Matching*. URL: https://www.rp-photonics.com/quasi_phase_matching.html (visited on 06/15/2022).

[13] M. Fejer, G. Magel, D. Jundt, and R. Byer. Quasi-phase-matched second harmonic generation: tuning and tolerances. *IEEE Journal of Quantum Electronics* 28(11) (1992), 2631–2654.

[14] S. Russell, P. Powers, M. Missey, and K. Schepler. Broadband mid-infrared generation with two-dimensional quasi-phase-matched structures. *IEEE Journal of Quantum Electronics* 37(7) (2001), 877–887.

[15] D. E. Thompson, J. D. McMullen, and D. B. Anderson. Second-harmonic generation in GaAs "stack of plates" using high-power CO2 laser radiation. *Applied Physics Letters* 29(2) (1976), 113–115.

[16] D. Zheng, L. A. Gordon, Y. S. Wu, R. S. Feigelson, M. M. Fejer, R. L. Byer, and K. L. Vodopyanov. 16-µm infrared generation by difference-frequency mixing in diffusion-bonded-stacked GaAs. *Opt. Lett.* 23(13) (July 1998), 1010–1012.

[17] K. L. Vodopyanov, O. Levi, P. S. Kuo, T. J. Pinguet, J. S. Harris, M. M. Fejer, B. Gerard, L. Becouarn, and E. Lallier. Optical parametric oscillation in quasi-phase-matched GaAs. *Opt. Lett.* 29(16) (Aug. 2004), 1912–1914.

[18] P. S. Kuo, K. L. Vodopyanov, M. M. Fejer, D. M. Simanovskii, X. Yu, J. S. Harris, D. Bliss, and D. Weyburne. Optical parametric generation of a mid-infrared continuum in orientation-patterned GaAs. *Opt. Lett.* 31(1) (Jan. 2006), 71–73.

[19] G. Insero, C. Clivati, D. D'Ambrosio, P. D. Natale, G. Santambrogio, P. G. Schunemann, J.-J. Zondy, and S. Borri. Difference frequency generation in the mid-infrared with orientation-patterned gallium phosphide crystals. *Opt. Lett.* 41(21) (Nov. 2016), 5114–5117.

[20] T. Matsushita, T. Yamamoto, and T. Kondo. Epitaxial Growth of Spatially Inverted GaP for Quasi Phase Matched Nonlinear Optical Devices. *Japanese Journal of Applied Physics* 46(No. 17) (Apr. 2007), L408–L410.

[21] V. L. Tassev, S. R. Vangala, R. D. Peterson, M. M. Kimani, M. Snure, R. W. Stites, S. Guha, J. E. Slagle, T. R. Ensley, A. A. Syed, and I. V. Markov. Heteroepitaxial growth of OPGaP on OPGaAs for frequency conversion in the IR and THz. *Opt. Mater. Express* 6(5) (May 2016), 1724–1737.

[22] P. G. Schunemann, C. Farrell, K. Johnson, D. T. Reid, and L. Maidment. Efficient frequency conversion in OP-GaP grown on OP-GaAs templates. In: *Nonlinear Frequency Generation and Conversion: Materials and Devices XX*. Ed. by P. G. Schunemann and K. L. Schepler. Vol. 11670. International Society for Optics and Photonics. SPIE, 2021.

[23] C. Ratcliff, T. J. Grassman, J. A. Carlin, and S. A. Ringel. High temperature step-flow growth of gallium phosphide by molecular beam epitaxy and metalorganic chemical vapor deposition. *Applied Physics Letters* 99(14) (2011), 141905.

[24] R. M. Biefeld. The preparation of device quality gallium phosphide by metal organic chemical vapor deposition. *Journal of Crystal Growth* 56(2) (1982), 382–388. ISSN: 0022-0248.

[25] M. Nandy, A. Paszuk, M. Feifel, C. Koppka, P. Kleinschmidt, F. Dimroth, and T. Hannappel. A Route to Obtaining Low-Defect III–V Epilayers on Si(100) Utilizing MOCVD. *Crystal Growth & Design* 21(10) (2021), 5603–5613.

[26] A. Beyer, J. Ohlmann, S. Liebich, H. Heim, G. Witte, W. Stolz, and K. Volz. GaP heteroepitaxy on Si(001): Correlation of Si-surface structure, GaP growth conditions, and Si-III/V interface structure. *Journal of Applied Physics* 111(8) (2012), 083534.

[27] H. Döscher. In: *GaP Heteroepitaxy on Si(100)*. Springer, 2013. ISBN: 978-3-319-02879-8.

[28] T. J. Grassman, J. A. Carlin, B. Galiana, L.-M. Yang, F. Yang, M. J. Mills, and S. A. Ringel. Nucleation-related defect-free GaP/Si(100) heteroepitaxy via metal-organic chemical vapor deposition. *Applied Physics Letters* 102(14) (2013), 142102.

[29] V. Dixit, T. Ganguli, T. Sharma, S. Singh, R. Kumar, S. Porwal, P. Tiwari, A. Ingale, and S. Oak. Effect of two-step growth process on structural, optical and electrical properties of MOVPE-grown GaP/Si. *Journal of Crystal Growth* 310(15) (2008), 3428–3435. ISSN: 0022-0248.

[30] S. Irvine and P. Capper. Introduction to Metalorganic Vapor Phase Epitaxy. In: *Metalorganic Vapor Phase Epitaxy (MOVPE)*. John Wiley Sons, Ltd, 2019. Chap. 1, 1–18. ISBN: 9781119313021.

[31] P. Laukkanen, M. P. J. Punkkinen, M. Kuzmin, K. Kokko, J. Lång, and R. M. Wallace. Passivation of III–V surfaces with crystalline oxidation. *Applied Physics Reviews* 8(1) (2021), 011309.

[32] R. Wixom, L. Rieth, and G. Stringfellow. Sb and Bi surfactant effects on homo-epitaxy of GaAs on (001) patterned substrates. *Journal of Crystal Growth* 265(3) (2004), 367–374. ISSN: 0022-0248.

[33] P. E. Batson, N. Dellby, and O. L. Krivanek. Sub-ångstrom resolution using aberration corrected electron optics. *Nature* 418 (2002), 617–620. ISSN: 1476-4687.

[34] F. J. Humphreys. Review Grain and subgrain characterisation by electron backscatter diffraction. *Journal of Materials Science* 36 (2001), 3833–3854.

[35] Imaging of Crystalline Specimens and Their Defects. In: *Transmission Electron Microscopy: Physics of Image Formation*. New York, NY: Springer New York, 2008, 356–415. ISBN: 978-0-387-34758-5.

[36] E. Okunishi, H. Sawada, and Y. Kondo. Experimental study of annular bright field (ABF) imaging using aberration-corrected scanning transmission electron microscopy (STEM). *Micron* 43(4) (2012). Advancing HR-TEM and HR-STEM, 538–544. ISSN: 0968-4328.

[37] N. Hernández-Pedro, E. Rangel-López, B. Pineda, and J. Sotelo. Atomic Force Microscopy in Detection of Viruses. In: *Atomic Force Microscopy Investigations into Biology*. Ed. by C. L. Frewin. Rijeka: IntechOpen, 2012. Chap. 11.

[38] U. Aridogan, Y. Shan, and K. K. Leang. Design and Analysis of Discrete-Time Repetitive Control for Scanning Probe Microscopes. *Journal of Dynamic Systems, Measurement, and Control* 131(6) (Oct. 2009). 061103. ISSN: 0022-0434.

[39] D. Nečas and P. Klapetek. Gwyddion: an open-source software for SPM data analysis. *Open Physics* 10(1) (2012), 181–188.

[40] Gwyddion. *Data Levelling and Background Subtraction*. URL: http://gwyddion.net/documentation/user-guide-en/leveling-and-background.html (visited on 05/18/2022).

[41] Gwyddion. *Scan Line Artefacts*. URL: http://gwyddion.net/documentation/user-guide-en/scan-line-defects.html (visited on 05/18/2022).

[42] B. B. He. Front Matter. In: *Two-dimensional X-ray Diffraction*. John Wiley Sons, Ltd, 2018, i–xv. ISBN: 9781119356080.

[43] W. C. Röntgen. 1896-01-23. *Nature* 53 (1896), 274–276.

[44] L. Bragg. X-RAY CRYSTALLOGRAPHY. *Scientific American* 219(1) (1968), 58–74. ISSN: 00368733, 19467087.

[45] B. B. He. Introduction. In: *Two-dimensional X-ray Diffraction*. John Wiley Sons, Ltd, 2018. Chap. 1, 1–28. ISBN: 9781119356080.

[46] B. B. He. Texture Analysis. In: *Two-dimensional X-ray Diffraction*. John Wiley Sons, Ltd, 2018. Chap. 8, 235–270. ISBN: 9781119356080.

[47] S. Weber. *WinWulff*. URL: http://www.jcrystal.com/products/winwulff/index.htm (visited on 06/16/2022).

[48] O. Supplie, S. Brückner, O. Romanyuk, H. Döscher, C. Höhn, M. M. May, P. Kleinschmidt, F. Grosse, and T. Hannappel. Atomic scale analysis of the GaP/Si(100) heterointerface by in situ reflection anisotropy spectroscopy and ab initio density functional theory. *Phys. Rev. B* 90 (23 Dec. 2014), 235301.